

AD-A033 654

VISIDYNE INC BURLINGTON MASS
ANALYSIS OF HIGH ALTITUDE EFFECTS SIMULATION (HAES).(U)
FEB 76 W P REIDY, T C DEGGES, W NEAL

F/G 4/1

F19628-74-C-0177

UNCLASSIFIED

VI-311

AFGL-TR-76-0039

NL

1 of 1
ADA033654



END

DATE
FILMED

2 - 77

ADA033654

13 (circled) (circled scribble)

AFGL-TR-76-0039
HAES REPORT NO. 40

ANALYSIS OF HIGH ALTITUDE EFFECTS SIMULATION (HAES)

W. P. Reidy
T. C. Degges
W. Neal

Visidyne, Inc.
19 Third Avenue
Northwest Industrial Park
Burlington, Massachusetts 01803

1 February 1976

Scientific Report No. 1

Approved for public release; distribution unlimited.

This research was sponsored by the Defense Nuclear Agency under Subtask L25AAXYX966, Work Unit 16, entitled :Analysis and Feasibility Assessment:, and Work unit 19, entitled "ICE CAP Data Analysis".

AIR FORCE GEOPHYSICS LABORATORY
AIR FORCE SYSTEMS COMMAND
UNITED STATES AIR FORCE
HANSCOM AFB, MASSACHUSETTS 01731

DDC
RECEIVED
DEC 22 1976
D

Qualified requestors may obtain additional copies from the Defense Documentation Center. All others should apply to the National Technical Information Service.

Unclassified

SECURITY CLASSIFICATION OF THIS PAGE (When Data Entered)

REPORT DOCUMENTATION PAGE		READ INSTRUCTIONS BEFORE COMPLETING FORM
1. REPORT NUMBER AFGL-TR-76-0039 ✓	2. GOVT ACCESSION NO.	3. RECIPIENT'S CATALOG NUMBER
4. TITLE (and Subtitle) ANALYSIS OF HIGH ALTITUDE EFFECTS SIMULATION (HAES)		5. TYPE OF REPORT & PERIOD COVERED Scientific Report No. 1 <i>9 Sept for 75</i>
7. AUTHOR(s) W. P. Reidy, W. Neal T. C. Degges		6. PERFORMING ORG. REPORT NUMBER VI-311 Scientific-1 7. CONTRACT OR GRANT NUMBER(s) F19628-74-C-0177 HAES Report No. 40
9. PERFORMING ORGANIZATION NAME AND ADDRESS Visidyne, Inc. 19 Third Avenue Burlington, Massachusetts 01803		10. PROGRAM ELEMENT, PROJECT, TASK AREA & WORK UNIT NUMBERS 62710H CDNA0020 CDNA0018
11. CONTROLLING OFFICE NAME AND ADDRESS Air Force Geophysics Laboratory Hanscom AFB, Massachusetts 01731 Contract Monitor: Dr. A. T. Stair, Jr/OPR		12. REPORT DATE February 1, 1976 <i>11 Feb 76</i>
14. MONITORING AGENCY NAME & ADDRESS (if different from Controlling Office)		13. NUMBER OF PAGES 81 <i>70p</i>
		15. SECURITY CLASS. (of this report) Unclassified
		15a. DECLASSIFICATION/DOWNGRADING SCHEDULE
16. DISTRIBUTION STATEMENT (of this Report) Approved for public release, distribution unlimited.		
17. DISTRIBUTION STATEMENT (of the abstract entered in Block 20, if different from Report) <i>18 AFGL DNA 19 TR-76-0039, HAES-40</i>		
18. SUPPLEMENTARY NOTES This research was sponsored by the Defense Nuclear Agency under Subtask L25AAXYX966, Work Unit 16, entitled "Analysis and Feasibility Assessment", and Work unit 19, entitled "ICECAP Data Analysis".		
19. KEY WORDS (Continue on reverse side if necessary and identify by block number) Electron deposition; Aurora; CO ₂ vibrational population; Atmospheric infrared emission; CO ₂ spectral radiance; Ozone spectral radiance		
20. ABSTRACT (Continue on reverse side if necessary and identify by block number) Initial formulation of the analysis of the energy deposition and the electron density profiles in our EXCEDE-type experiment are presented. Altitude profiles are given for the night time zenith spectral radiance for CO ₂ bands at 4.3 μm and 15 μm and for the ozone band at 9.6 μm . Model calculations of the vibrational population of the first excited level of the CO ₂ ν_3 vibrational mode are also presented. <i>micrometers</i>		

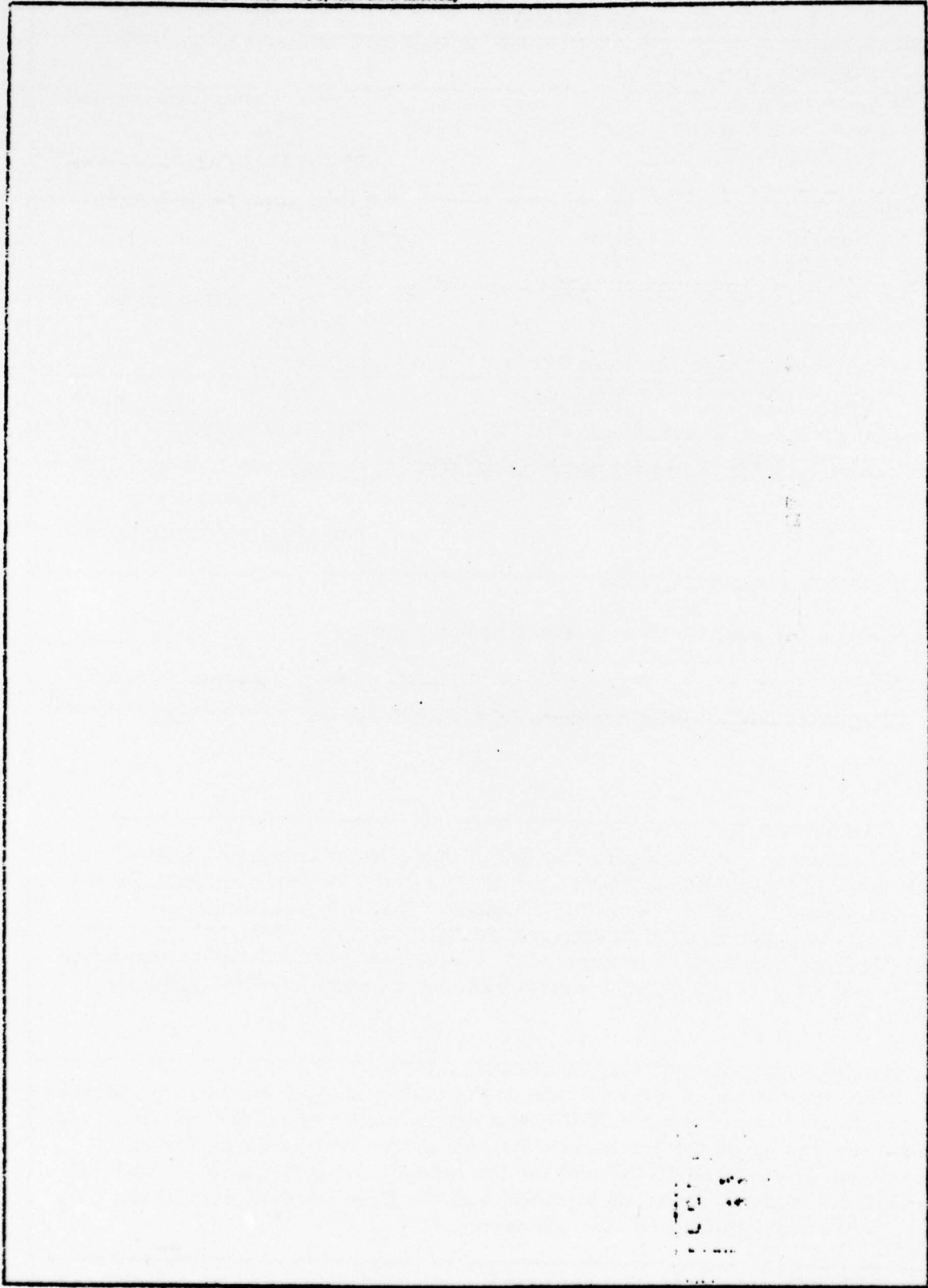
DD FORM 1 JAN 73 1473 EDITION OF 1 NOV 65 IS OBSOLETE

Unclassified

SECURITY CLASSIFICATION OF THIS PAGE (When Data Entered)

nu sub 3

SECURITY CLASSIFICATION OF THIS PAGE(When Data Entered)



The calculations in this report provided a portion of the theoretical data base on which the EXCEDE series of rocketborne electron experiments were designed. The support of Dr. Harold C. Fitz, Jr and LCDR Chris Thomas of DNA and Mr. Herb Mitchell of R&D Associates and the technical direction of Dr. A.T. Stair, Jr., Mr. James Ulwick and Mr. Robert R. O'Neil of AFGL is gratefully acknowledged.

TABLE OF CONTENTS

	PAGE
1.0 INTRODUCTION	7
2.0 ENERGY DEPOSITION	9
3.0 SPECTRAL RADIANCE CALCULATIONS AT 4.3 μm , 9.6 μm , 15 μm	20
4.0 MODEL CALCULATIONS OF THE VIBRATIONAL POPULATION OF THE FIRST EXCITED LEVEL ν_3 VIBRATIONAL MODEL	22
REFERENCES	
APPENDIX 1 - Auroral Electron Energy Spectra Rocket A18.219-1 Launched 25 February 1974	38
APPENDIX 2 - Spectral Radiance Calculations at 4.3 μm , 9.6 μm , and 15 μm	65

1.0 INTRODUCTION

Contract F19628-74-C-0177 is a contract to analyze High Altitude Effects Simulation (HAES) Experiments performed as part of the ICECAP and EXCEDE Programs and the application of these measurements to physics and chemistry code modelling of atmospheric emissions, such as OPTIR. The work performed under the initial phase of this program includes modelling of energy deposition, particularly for EXCEDE type experiments where radial distributions are probably more important than in auroral events (Section 2.0); calculations of the zenith spectral radiance at 4.3 μm (Section 3.0); and calculations of vibrational population of the first excited level of the CO_2 ν_3 vibrational mode (Section 4.0).

2.0 ENERGY DEPOSITION

The energy deposition calculations are based on the Berger, et al^[1] Monte Carlo results which are briefly summarized in the functional relations

$$F(h, r) = \rho(h) R(h, r) A(z_m)$$

$$R(h, r) = F(h, r) / \int_0^{\infty} F(h, r') 2r' dr'$$

$$A(z_m) = (E/r_p) f(z_m/r_p)$$

$$z_m = \int_h^{h_0} \rho(h') dh'$$

where $F(h, r)$ is the energy per unit volume deposited at a distance $h-h_0$ down along the field line and r radially outward from a magnetic field line passing through the injection point of a single electron. Needed to calculate this are $\rho(h)$, the atmospheric density at the point of observation; $R(h, r)$ the radial distribution function; z_m , the mass thickness between the points of injection and observation; and r_p , the practical range of the incident electron (Figures 1, 2, 3).

The Monte Carlo calculations have been fitted by Berger, et al, to the following functional approximations:

$$R(h, r) \approx \frac{1}{2\pi r_H^2} \frac{b^a}{\Gamma(a)} \left(\frac{r}{r_H}\right)^{a-2} e^{-b(r/r_H)}$$

where

r_H - the initial Larmor radius of the incident electron

a, b - dimensionless parameters related to moments of $R(h, r)$

where $\langle \rho \rangle$ is the mean radius and the variance is σ^2 ; $\sigma^2 = \langle \rho^2 \rangle - \langle \rho \rangle^2$

$$a = \frac{\langle \rho^2 \rangle}{\sigma^2}; b = \frac{a r_H}{\langle \rho \rangle}$$

Figure 4 is a plot of $1/\sqrt{a}$ as a function of z_m/r_p . Figure 5 is a plot of a/b as a function of energy for different values of z_m/r_p . Figure 6 is a plot of a/b as a function of z_m/r_p for 3 keV electrons.

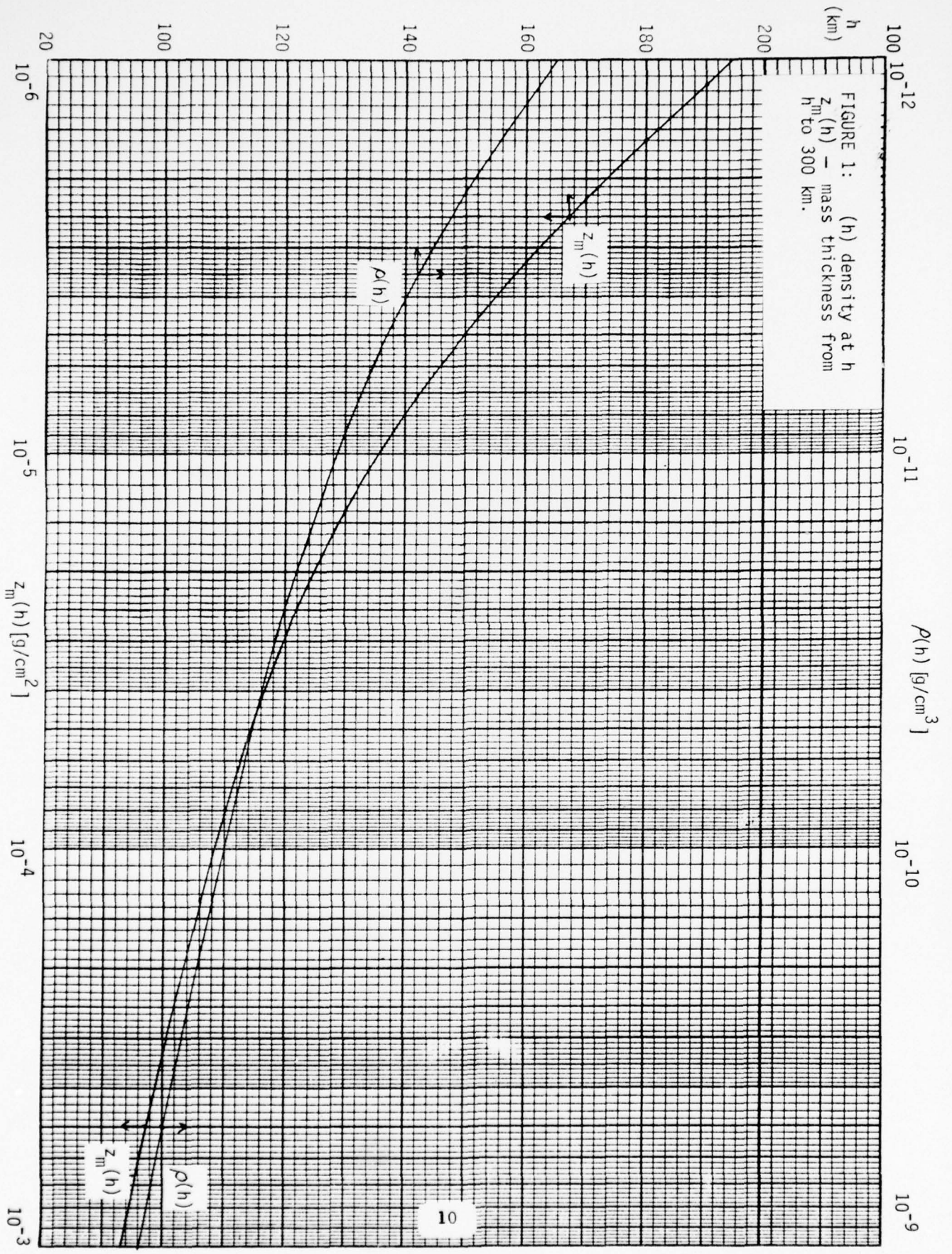
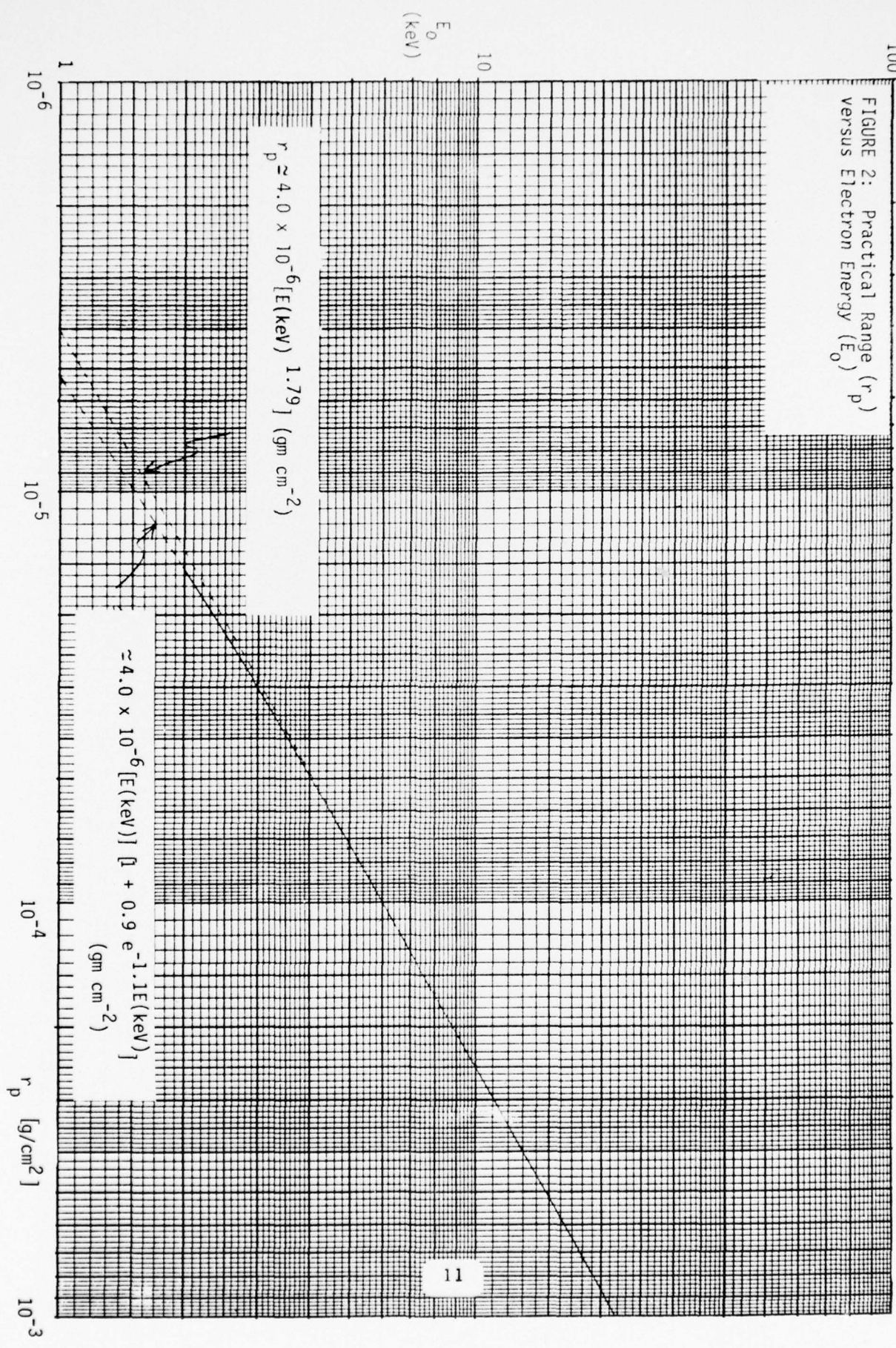
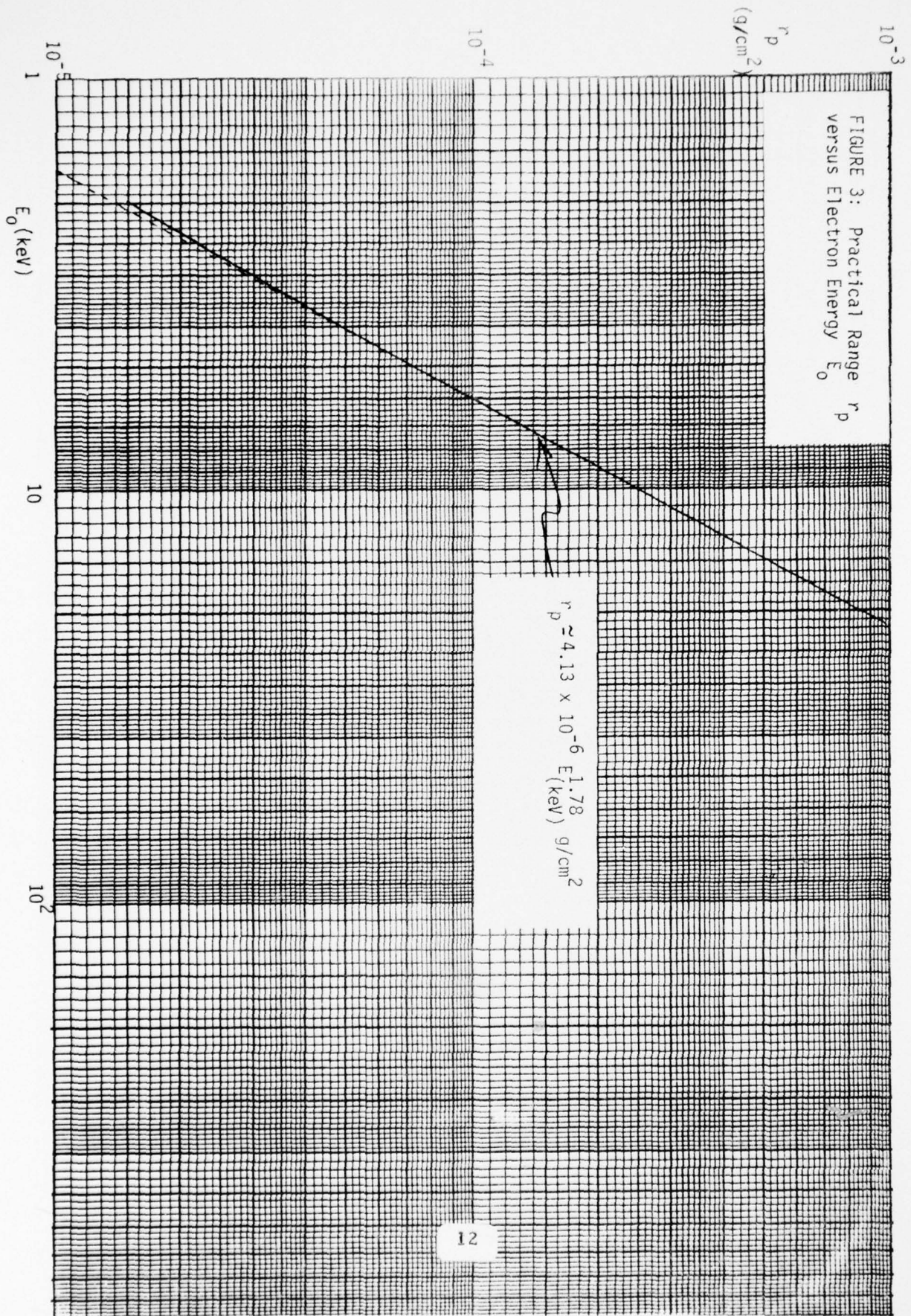


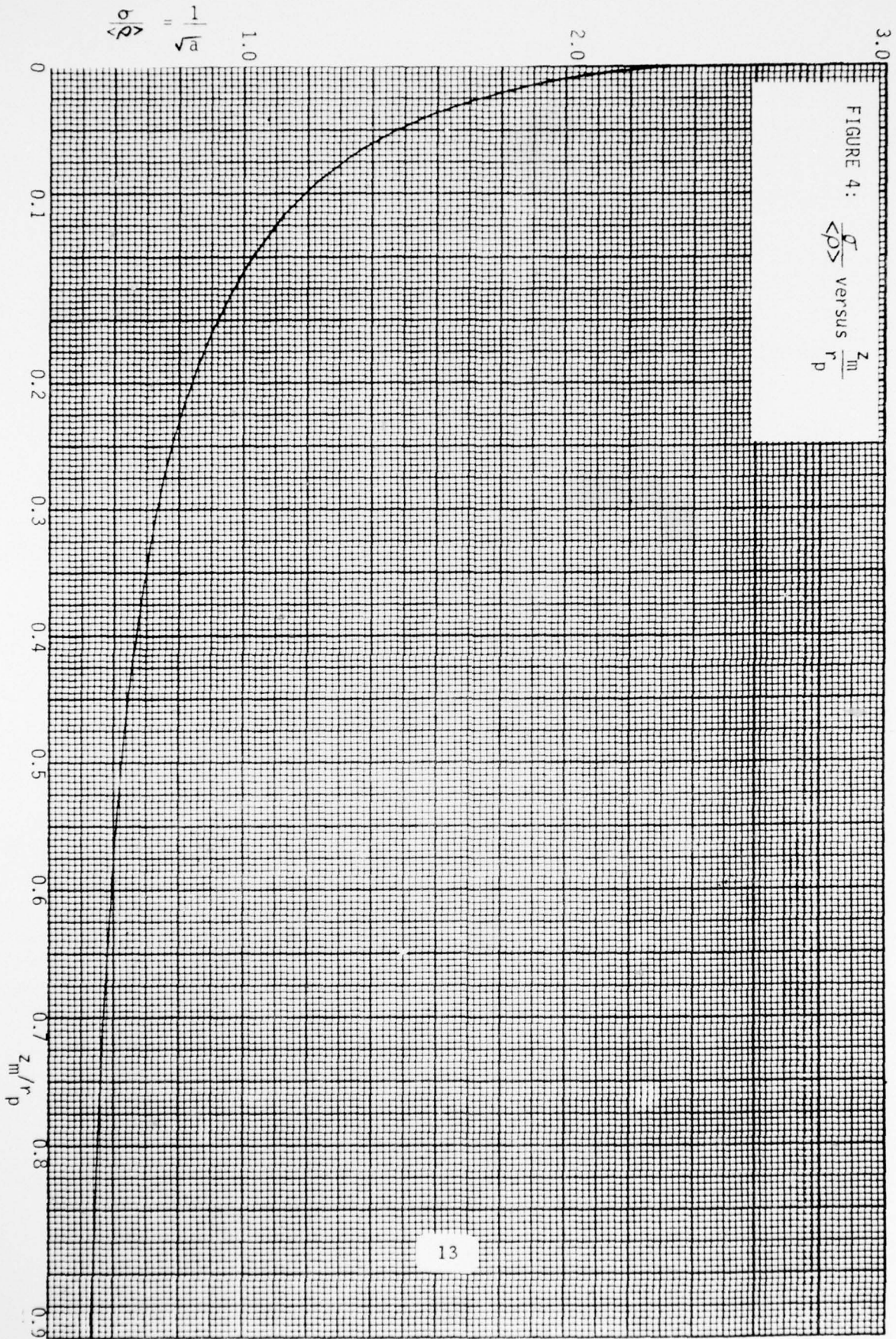
FIGURE 2: Practical Range (r_p) versus Electron Energy (E_0)





$2 \leq E_0 \leq 20 \text{ keV}$

$\theta_0 = 0^\circ$



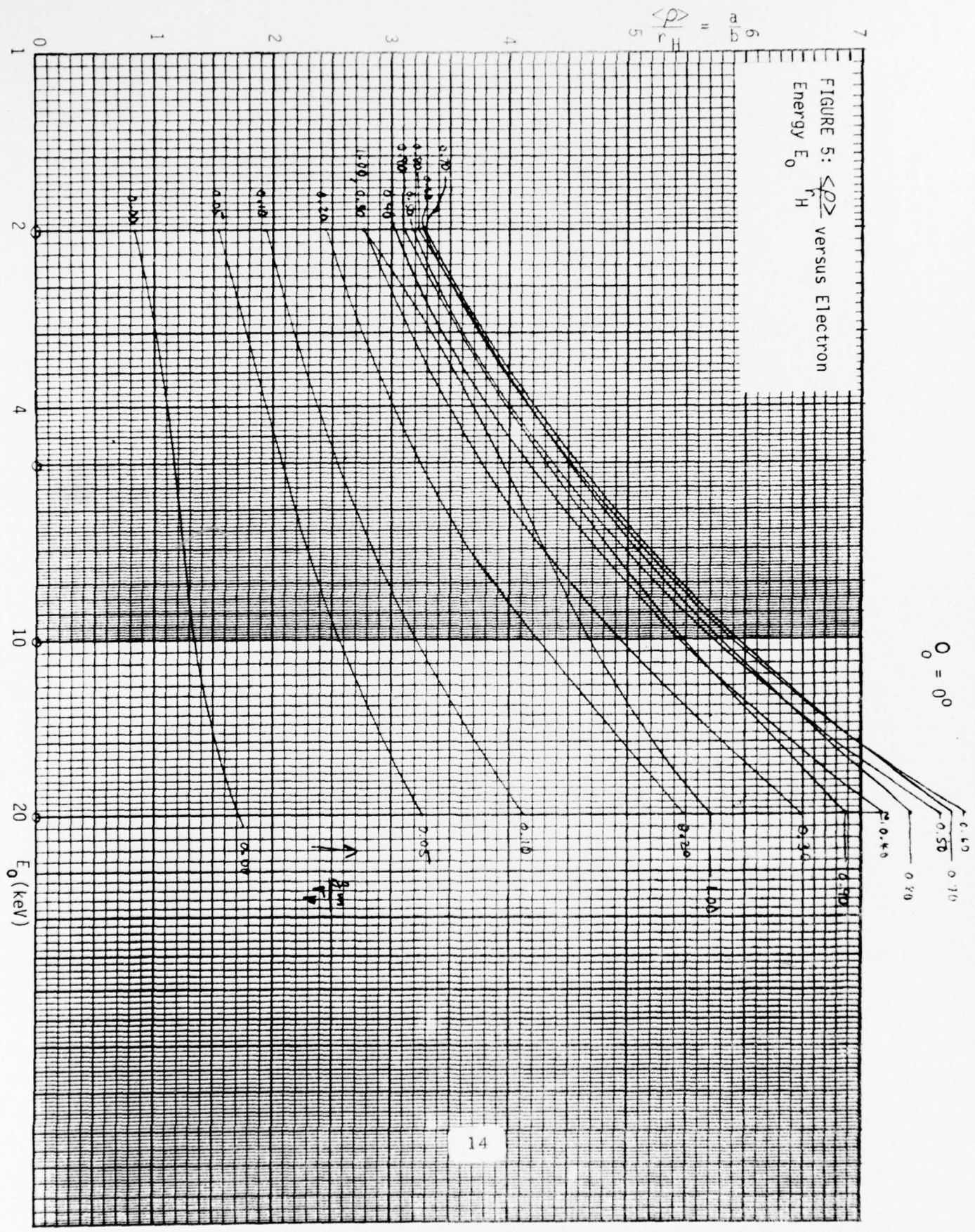
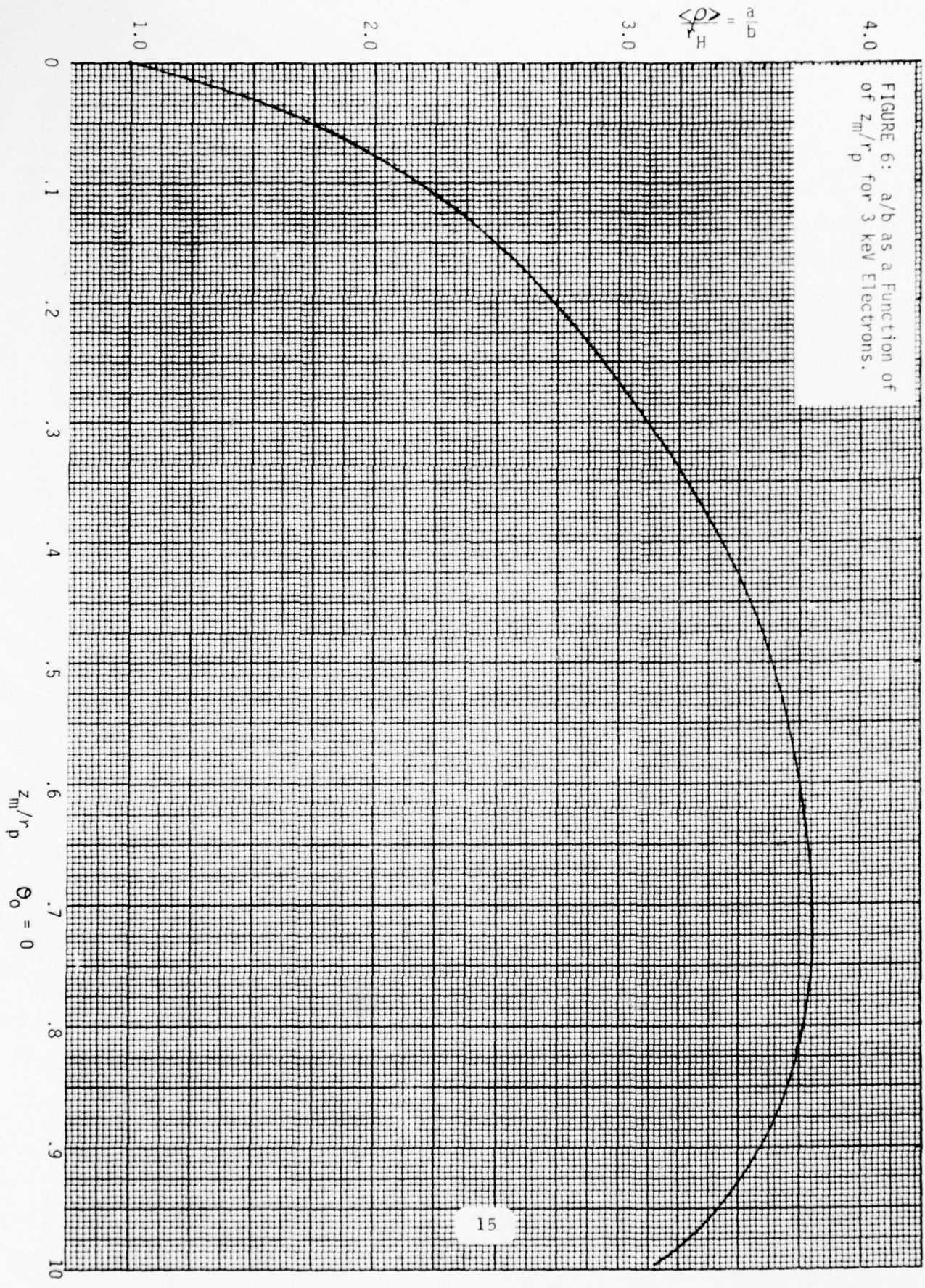


FIGURE 5: $\langle \rho \rangle$ versus Electron Energy E_0

$\theta_0 = 0^\circ$

FIGURE 6: a/b as a Function of z_m/r_p for 3 keV Electrons.



Tables in the Berger, et al paper provide: radial distribution a and b parameters for a range of energies and distances from the point of injection; atmospheric density as a function of altitude; and values of the "universal" f-function of the axial factor, $A(z_m)$, for various distances from the source. These tabular entries will be least-squares fitted to appropriate functions and incorporated into a subroutine that returns the energy deposition rate and ionization production rate, $Q = \dot{n}_e = F(h, r) \cdot I_0 / ew$ (I_0 - beam current, e - electron charge, w - eV/ion pair), for a given energy and geometry.

Recombination

For sufficiently high ionization densities, recombination may modify results significantly and thus must be taken into account.

The basic equation relating the ionization density to source strength is:

$$\dot{n}_e(t) = Q(t) - \alpha n_e^2(t)$$

a nonlinear, first-order differential equation of the Riccati type. The analytical solution for arbitrary $Q(t)$ is not known, but through the nonlinear transformation

$$\hat{n}(t) = \exp\left(\alpha \int^t dt' n_e(t')\right)$$

The linear, but second-order, homogeneous differential equation

$$\ddot{\hat{n}}_e(t) - \alpha Q(t) \hat{n}_e(t) = 0$$

is obtained, which for certain source term functional dependences, can be solved in terms of known functions.

Line Integrals

The electron density, $n_e(\vec{r}, t)$, being defined by a nonlinear differential equation involving a time-varying source function, will virtually

never be obtained in an analytical form so that a numerical evaluation of the line integral $\int n_e(\vec{r}, t) dl$, is unavoidable. For each sub-interval of the integral, the value of $n_e(\vec{r}, t)$ will have to be obtained by an integration of the equation $\dot{n}_e(t) = Q(t) - \alpha n_e^2(t)$, where the time variation, $Q(t)$, of the source is due to source trajectory motion and possibly to source intensity changes.

Approximate Calculations

For order of magnitude and qualitative investigations, certain simplified cases have been studied. If recombination during the relatively brief duration of the source pulse, $Q(t)$, can be neglected, then

$$\dot{n}_e(t) = Q(t) - \alpha n_e^2(t) \simeq Q(t)$$

and the electron density during the source pulse is given by

$$n_e(t) \simeq \int_{-\infty}^t dt' Q(t')$$

After the source pulse is over, $\dot{n}_e = -\alpha n_e^2$, which has the solution

$$n_e(t) = \frac{n_o}{1 + \alpha n_o t}$$

where $n_o = \int_{-\infty}^{\infty} dt' Q(t')$ is the total electron density produced by the source pulse (in the absence of recombination). Since, for the general point in space,

$$Q(t) = Q(h(t), r(t)) = I_o F(h, r)/ew$$

where h and r are determined by the (moving) source and observation point geometry, then

$$n_e(\vec{r}, t) = \frac{n_o(\vec{r})}{1 + \alpha n_o(r)t}$$

where

$$n_o(\vec{r}) = \frac{I_o}{ew} \int_{-\infty}^{\infty} dt' F(h(t), r(t))$$

To perform an analytical line integration of this $n_e(\vec{r}, t)$, the "initial" distribution, $n_o(\vec{r})$, must be of relatively simple algebraic form. Unfortunately, the $n_o(\vec{r})$ from the Berger theory is generally a non-elementary integral, effectively making a closed solution impossible. However, in the special case of line integrals along directions normal to the plane of the magnetic field and source velocity, and at altitudes for which the radial distribution, $R(h, r)$, has an integer a -parameter, $n_o(\vec{r})$ can be evaluated in terms of the zero and first-order modified Hankel functions. These special $n_o(\vec{r})$ cases can be evaluated from tables and least-squares fit to functions that permit analytical evaluation of the line integral to yield the approximate time dependence of $\int n_e dl$ at the special altitudes.

The model distributions which were fit to the special (evaluable) integrals were rectangular (uniform), triangular, exponential and Lorentzian. The resulting time profiles differed by 40% at one characteristic time, τ_o ; by 3:1 at $10 \tau_o$ and by 10:1 at $100 \tau_o$.

More Exact Calculations

With some idea of the source function pulses, $Q(t)$, to be encountered, the electron density $n_e(\vec{r}, t)$ can be estimated, now taking recombination into account, either by numerically integrating the basic equation

$$\dot{n}_e(t) = Q(t) - \alpha n_e^2(t)$$

defining $Q(t)$ directly in terms of the Berger function, $F(h, r)$, or by segmental representation of $Q(t)$ with polynomial fits to selected values of the Berger function.

There exist a number of straightforward, first-order differential equation numerical integration techniques, but good numerical accuracy

requires evaluation of a relatively complicated $Q(t)$ function many times over. Since the many such time-integrations required in the various desired line integrals might prove too costly in computer time, a linear segment representation approach was also looked into. If the $Q(t)$ function can be adequately represented by five or ten linear segments, then the solution throughout any segment can be expressed in terms of the solutions of the transformed, second-order differential equation:

$$\hat{n}_e(t) + \alpha Q(t) \hat{n}_e(t) = 0$$

where

$$Q(t) = Q_0 (1 + t/\tau)$$

the solutions of which are directly related to the Airy integrals $Ai(x)$ and $Bi(x)$ and their derivatives. Subroutines to evaluate these functions for $-\infty < x < \infty$ have been written and await testing.

The energy deposition calculations discussed above are applicable to both the ICECAP and EXCEDE Programs and will be used to evaluate electron spectra such as that presented in Appendix 1. The accuracy of the radial description is more relevant to the EXCEDE geometry than to a typical auroral geometry.

3.0 SPECTRAL RADIANCE CALCULATIONS AT 4.3 μM , 9.6 μM , 15 μM .

The night time zenith spectral radiance has been calculated for the CO_2 bands at 4.3 μm and 15 μm and for the ozone band at 9.6 μm at altitudes for 60 to 120 μm . The spectral radiance was calculated assuming the U. S. Standard Atmosphere (180° K Mesospheric temperature) and an atmosphere with a 230° K Mesospheric temperature. The results are presented in Appendix 2. Degges 1974 Infrared Radiance Model² was used for these calculations.

Degges' work is an extension of the study of Corbin, et al. (1969)³ and Degges (1972)⁴. The former investigated the natural infrared background of the earth in the 5 to 25 micrometer spectral region. For convenience, their study divided the atmosphere into two regions with a division at 70 km. Below 70 km the atmosphere was assumed to be in thermal equilibrium. Above 70 km explicit calculations were made of processes which excite and de-excite molecular vibrational and rotational levels which are the source of infrared radiation. Their study concentrated on radiation from water vapor, carbon dioxide, ozone, nitric oxide and nitrous oxide, which are the principal radiating species in the spectral region considered. In addition, nitric acid was included in the lower atmosphere work and estimates were made of radiation to be expected from particulate matter suspended in the atmosphere.

Corbin, et al. (1969) presented models for the lower atmosphere for a wide range of seasonal and latitudinal conditions. This was not possible for the abundances of most minor neutral species. More data has since become available, particularly for nitric oxide and the hydroxyl radical, but at present it appears that the best means of estimating abundances of important infrared emitting species is chemical rate equation integrations including molecular diffusion and eddy mixing. Even calculations involving transport properties cannot always be accepted because the values of eddy mixing coefficients are to a large extent only informed

guesses and published calculations often use outdated rate coefficients. Degges (1972) reported a computer program with which to determine diurnal variations in abundances of minor species, to investigate the effects of changes in assumed eddy mixing coefficients, and to estimate the effects of new determinations of chemical rate coefficients.

A second area of study involved in improving the radiance model includes the physical processes that control the population of infrared emitting states of atmospheric molecules. Except for the pure rotational radiation from molecules such as water, the degree of excitation of vibrational levels determines the radiation from infrared emitting molecules. The most important mechanisms are collisional excitation and de-excitation and absorption and re-emission of electromagnetic radiation.

In the troposphere and lower stratosphere, collisional processes are rapid enough to control the population of vibrational levels. Above 30 to 50 km, however, collisional excitation becomes less efficient and radiative processes become important. The combined effects of collisional and radiative processes must therefore be considered. Below an altitude of about 90 km molecular nitrogen and oxygen are the most important collision partners. Above that altitude, atomic oxygen becomes important, both in exciting nitric oxide and in determining molecular oxygen and nitrogen vibrational temperatures.

In determining the effects of radiation on the populations of vibrational levels of infrared active molecules, it is necessary to separate the radiation of a single change in vibrational quantum numbers from the rest of the radiation field. The previously reported studies did this by assuming a Doppler line shape for the individual rotational lines of a band and were able to obtain adequate numerical approximations for radiative transfer functions appropriate to single bands of linear molecules, and less accurately, for water vapor and ozone bands lying in the spectral region of interest.

4.0 MODEL CALCULATIONS OF THE VIBRATIONAL POPULATION OF THE FIRST EXCITED LEVEL ν_3 VIBRATIONAL MODEL.

In order to gain insight as to possible effects of the time and space variations in auroral excitation of the carbon dioxide (CO_2) infrared band systems, we have continued model calculations of the vibrational population of the first excited level of the CO_2 ν_3 vibrational mode. The model atmosphere used contains only CO_2 , molecular nitrogen, and atomic and molecular oxygen. The CO_2 mixing ratio is assumed constant at 320 parts per million, by volume. Calculations are restricted to levels two kilometers apart lying between 50 and 150 kilometers altitude. The temperature falls from 270 K at 50 km to a mesopause temperature of 191 between 80 and 90 km. Above 90 km, the temperature rises to 661 K at 150 km.

The radiative transfer model of Degges (1974) is used with the collision processes of Table 1, the rates shown being those given by Garvin and Hampson (1974).⁵ The QCHEM integration algorithm described by Manley, et al (1973)⁶ is used to integrate rate equations for the vibrational populations of the CO_2 ν_3 mode and the first vibrational levels of N_2 and O_2 . The results presented in the following figures should be regarded as only semi-quantitative. The system of rate equations is stiff with coupling between stiff components through the radiation field. Manley, et al (1973) point out that in cases of this nature, the solution given by the QCHEM algorithm relaxes in the correct direction, but the numerical results are not properly correlated with the prescribed time steps.

Results are presented here for two (2) sample cases. In the first, vibrational temperatures at all altitudes were set to 250 K initially. Assuming night time conditions, the system was integrated for 10^6 seconds. Then, an auroral "drizzle" was introduced with a peak ionization rate of 2.5×10^3 ion pairs $\text{cm}^{-3} \text{sec}^{-1}$ at 110 km and the integration continued for 10^6 seconds. Then, a strong arc was turned on, with a peak ionization

TABLE I

Collisional De-excitation Rates

1. $N_2 (v = 1) + M \rightarrow N_2 (v = 0) + M$
 $k_1 = 8.53 \times 10^{-7} \exp (-273.10/T^{1/3})$
2. $O_2 (v = 1) + M \rightarrow O_2 (v = 0) + M$
 $k_2 = 4.81 \times 10^{-8} \exp (-169.60/T^{1/3})$
3. $CO_2 (001) + N_2 (v = 0) \rightarrow CO_2 (000) + N_2 (v = 1)$
 $k_3 = 1.71 \times 10^6 \exp (-175.30/T^{1/3}) + 6.07 \times 10^{-14} \exp (15.27/T^{1/3})$
4. $N_2 (v = 1) + O_2 (v = 0) \rightarrow N_2 (v = 0) + O_2 (v = 1)$
 $k_4 = 1.74 \times 10^{-10} \exp (-124.00/T^{1/3})$
5. $N_2 (v = 1) + O \rightarrow N_2 (v = 0) + O$
 $k_5 = 1.07 \times 10^{-10} \exp (-69.90/T^{1/3})$
6. $O_2 (v = 1) + O \rightarrow O_2 (v = 0) + O$
 $k_6 = 6.88 \times 10^{-9} \exp (-76.65/T^{1/3})$

rate of 10^6 ion pairs $\text{cm}^{-3} \text{sec}^{-1}$ at 100 km and the integration continued for 10^6 seconds. Following this, the auroral excitation was turned off and relaxation followed for 10^4 seconds. The procedure was repeated for an initial vibrational temperature of 300 K. In both cases, the assumption was made that for each ion pair produced, three nitrogen molecules are excited to the first vibrational level.

Figures 1 through 4 display results for the case where initial vibrational temperatures are 250 K. Figures 5 through 8 display results for the case where initial vibrational temperatures are 300 K.

In Figure 1, vibrational populations increase with time below 60 km as collisions and radiative transport are effective in bringing vibrational temperatures closer to kinetic temperatures. Above 75 km, populations fall with time. At late times, populations rise above 125 km as collisions are effective in increasing nitrogen vibrational temperatures toward kinetic temperatures, with subsequent transfer of vibrational excitation to CO_2 .

There is little change in Figure 2, the "drizzle" excitation not being large compared to the normal collisional and radiative mechanisms.

The auroral effects are clearly evident in Figure 3. Above 100 km, a balance is reached between enhanced auroral excitation and radiative decay by 10^4 seconds. This aurora produces no ionization at 90 km and below. At late times, vibrational populations continue to increase at altitudes as low as 85 km as energy is transported down by radiation. This downward transport of radiation continues after the aurora is turned off, as shown in Figure 4.

The behavior for the higher initial vibrational temperature of 300 K is similar, as shown in Figures 5 through 8, except that vibrational temperatures fall at all times for altitudes below 65 km. The auroral effects are not as visibly pronounced, because of the higher initial vibrational temperature.

Figures 9 through 12 present vibrational temperatures corresponding to the vibrational populations of Figures 1 through 4.

Figure Captions

- Figure 1 CO₂ ν_3 vibrational populations at 10^{-4} , 10^{-3} , 10^5 , 10^6 seconds following relaxation from a uniform vibrational temperature of 250 K.
- Figure 2 CO₂ ν_3 vibrational populations at 10^{-4} , 10^{-3} , 10^5 , 10^6 seconds with auroral "drizzle", following conditions of Figure 1.
- Figure 3 CO₂ ν_3 vibrational populations at 10^{-4} , 10^{-3} , 10^5 , 10^6 seconds with strong auroral arc, following conditions of Figure 2.
- Figure 4 CO₂ ν_3 vibrational populations at 10^{-6} , 10^{-5} , 10^3 , 10^4 seconds during relaxation from conditions of Figure 3.
- Figure 5 CO₂ ν_3 vibrational populations at 10^{-4} , 10^{-3} , 10^5 , 10^6 seconds following relaxation from a uniform vibrational temperature of 300 K.
- Figure 6 CO₂ ν_3 vibrational populations at 10^{-4} , 10^{-3} , 10^5 , 10^6 seconds with auroral "drizzle", following conditions of Figure 5.
- Figure 7 CO₂ ν_3 vibrational populations at 10^{-4} , 10^{-3} , 10^5 , 10^6 seconds with strong auroral arc, following conditions of Figure 6.
- Figure 8 CO₂ ν_3 vibrational populations at 10^{-6} , 10^{-5} , 10^3 , 10^4 seconds during relaxation from conditions of Figure 7.
- Figure 9 CO₂ ν_3 vibrational temperatures corresponding to vibrational populations of Figure 1.
- Figure 10 CO₂ ν_3 vibrational temperatures corresponding to Figure 2.
- Figure 11 CO₂ ν_3 vibrational temperatures corresponding to Figure 3.
- Figure 12 CO₂ ν_3 vibrational temperatures corresponding to Figure 4.

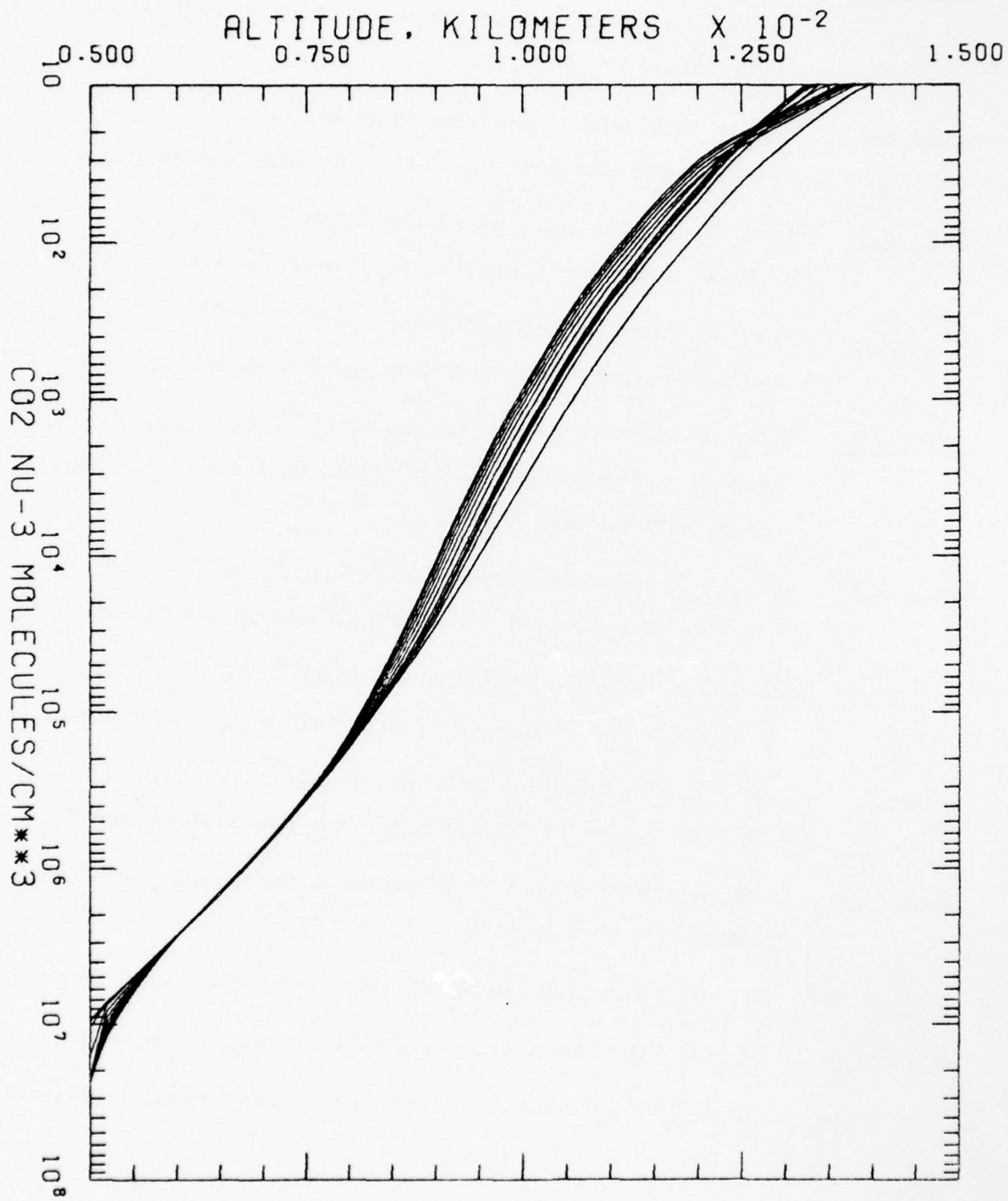


Figure 1

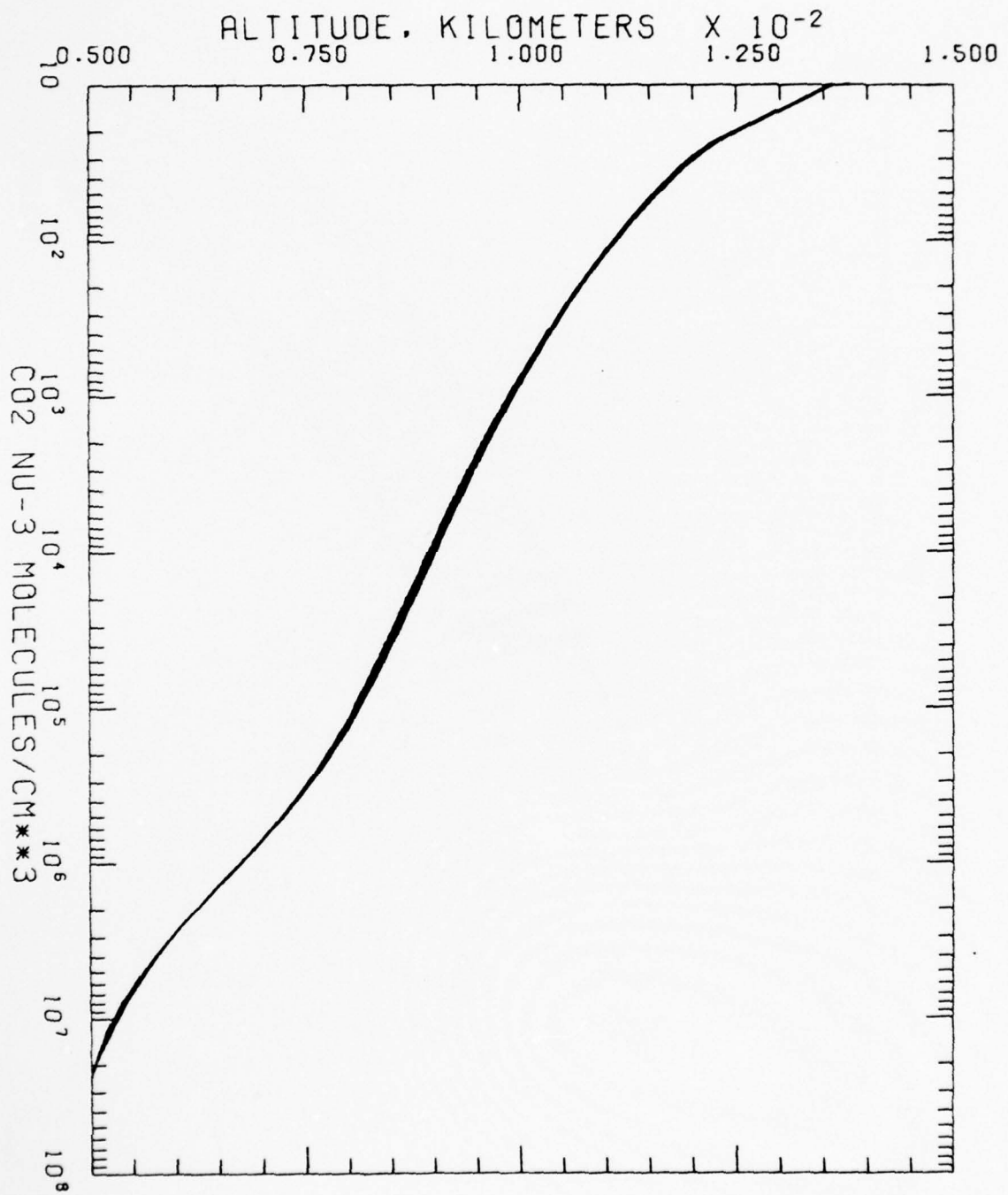


Figure 2

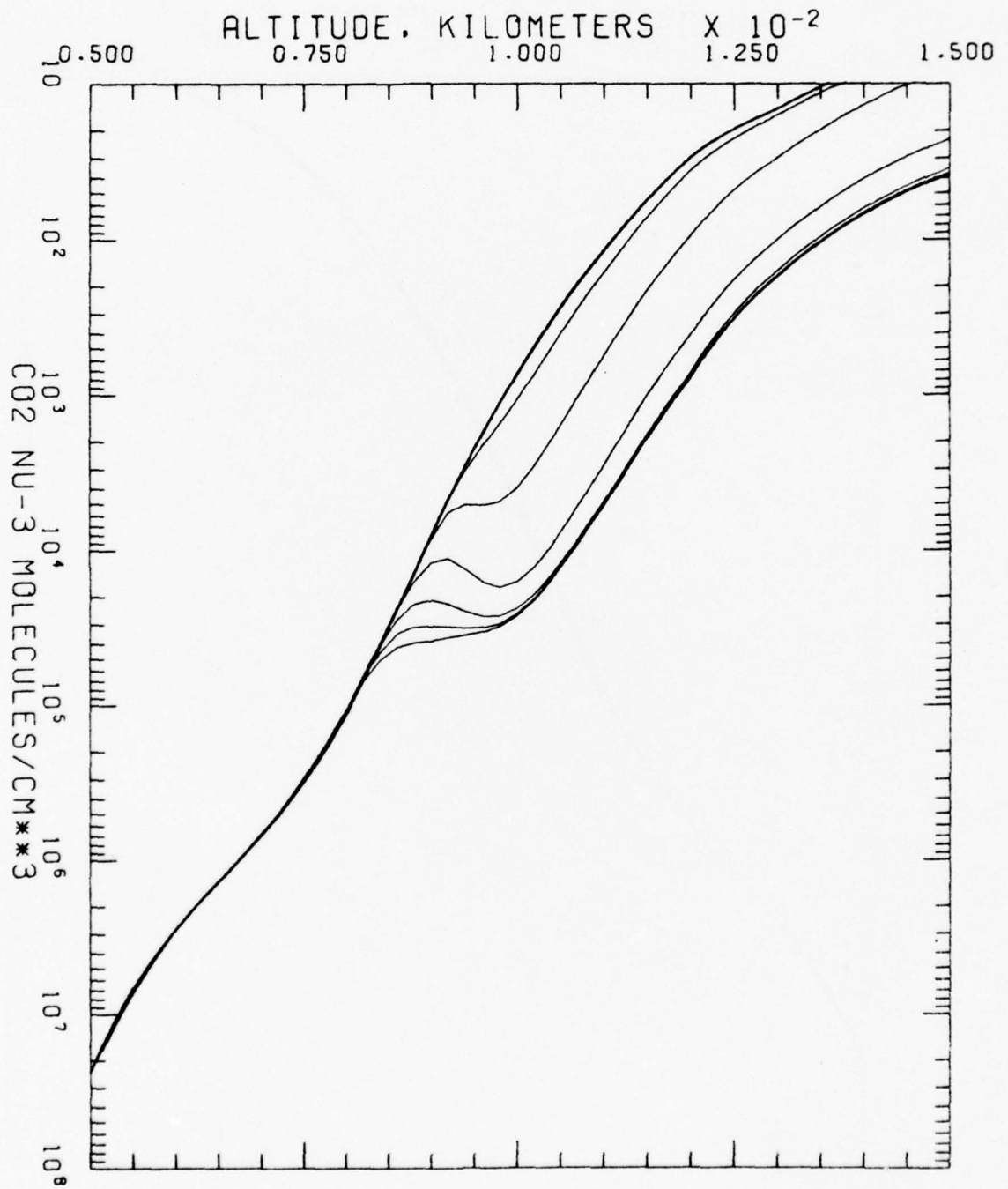


Figure 3

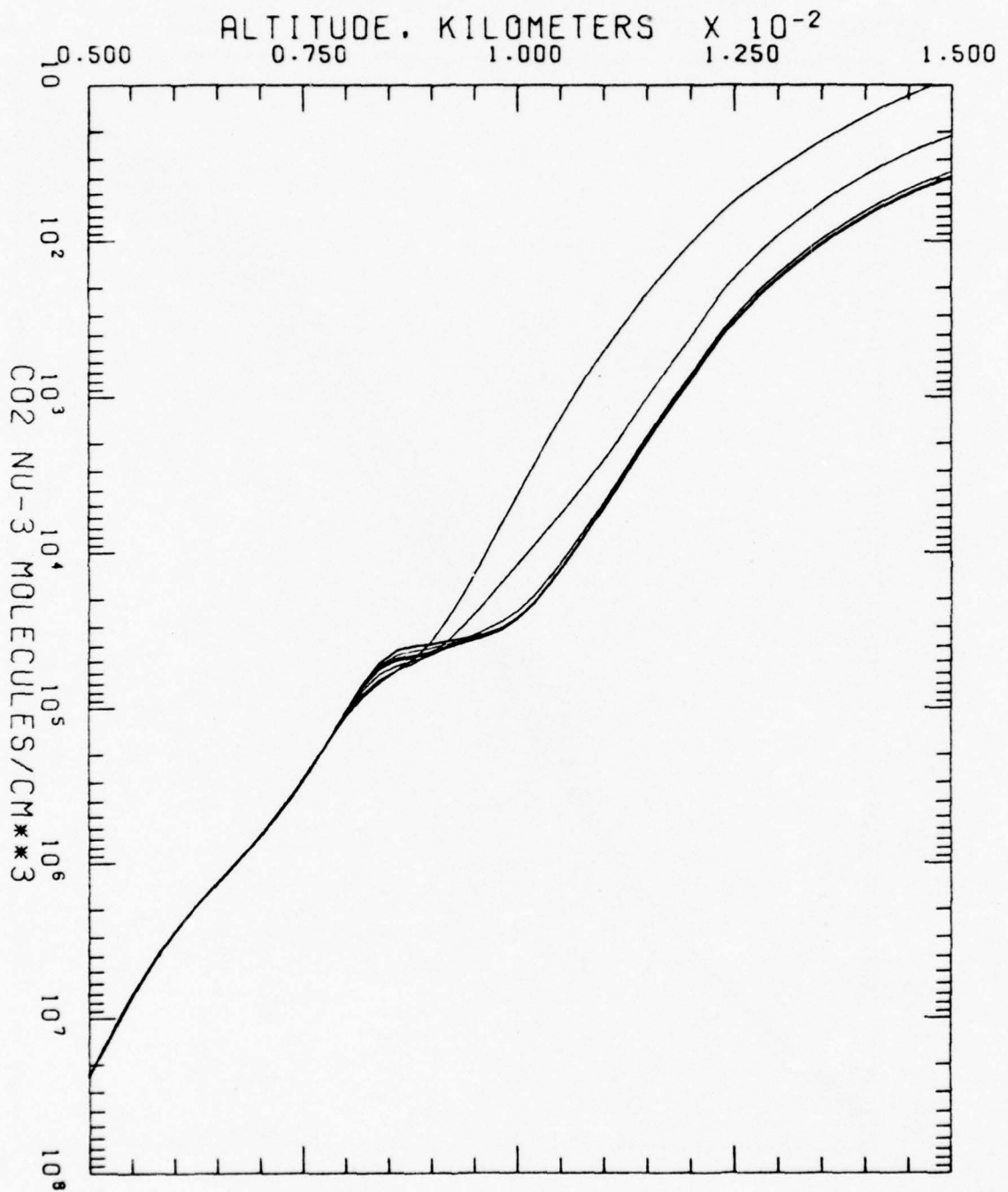


Figure 4

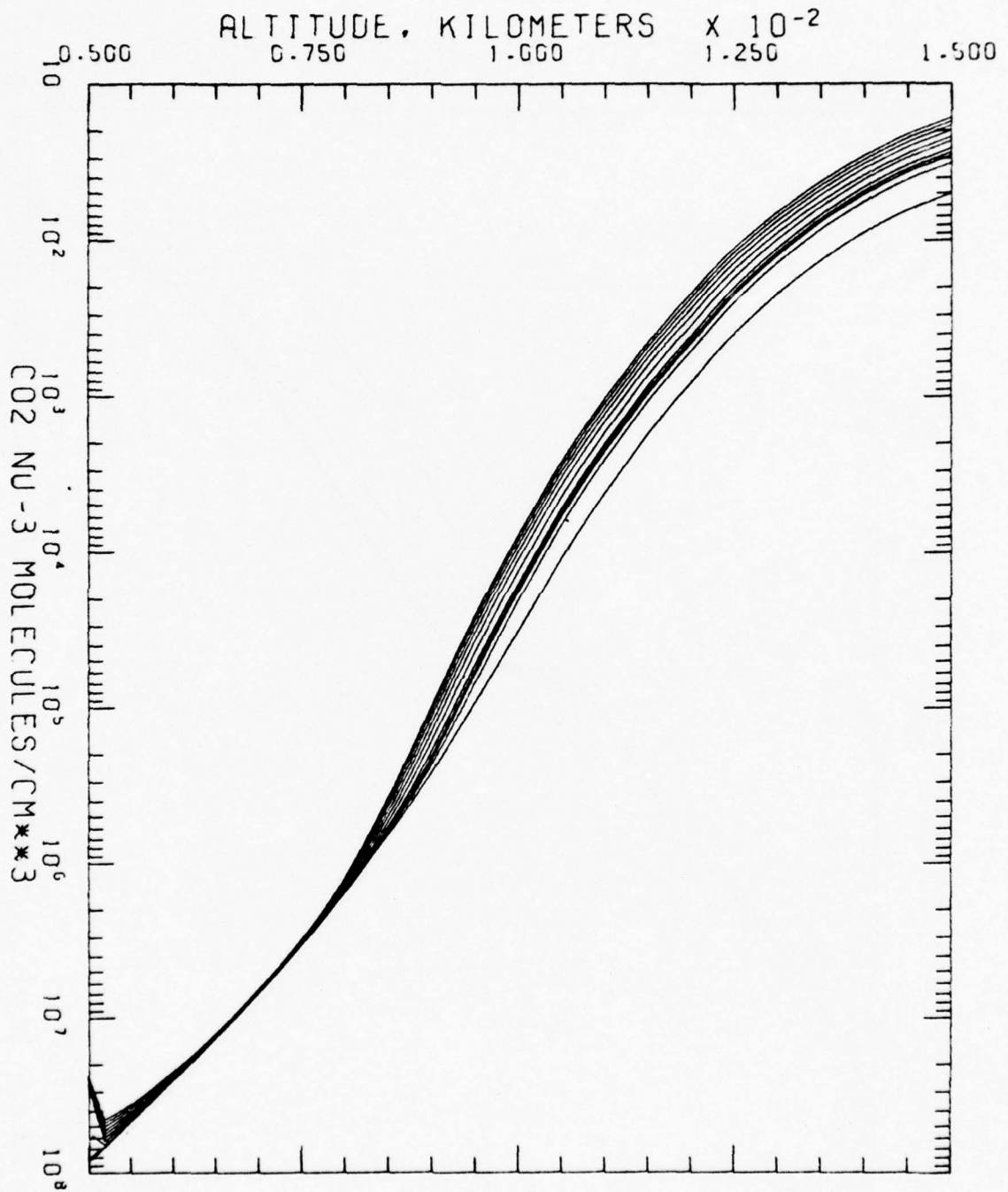


Figure 5

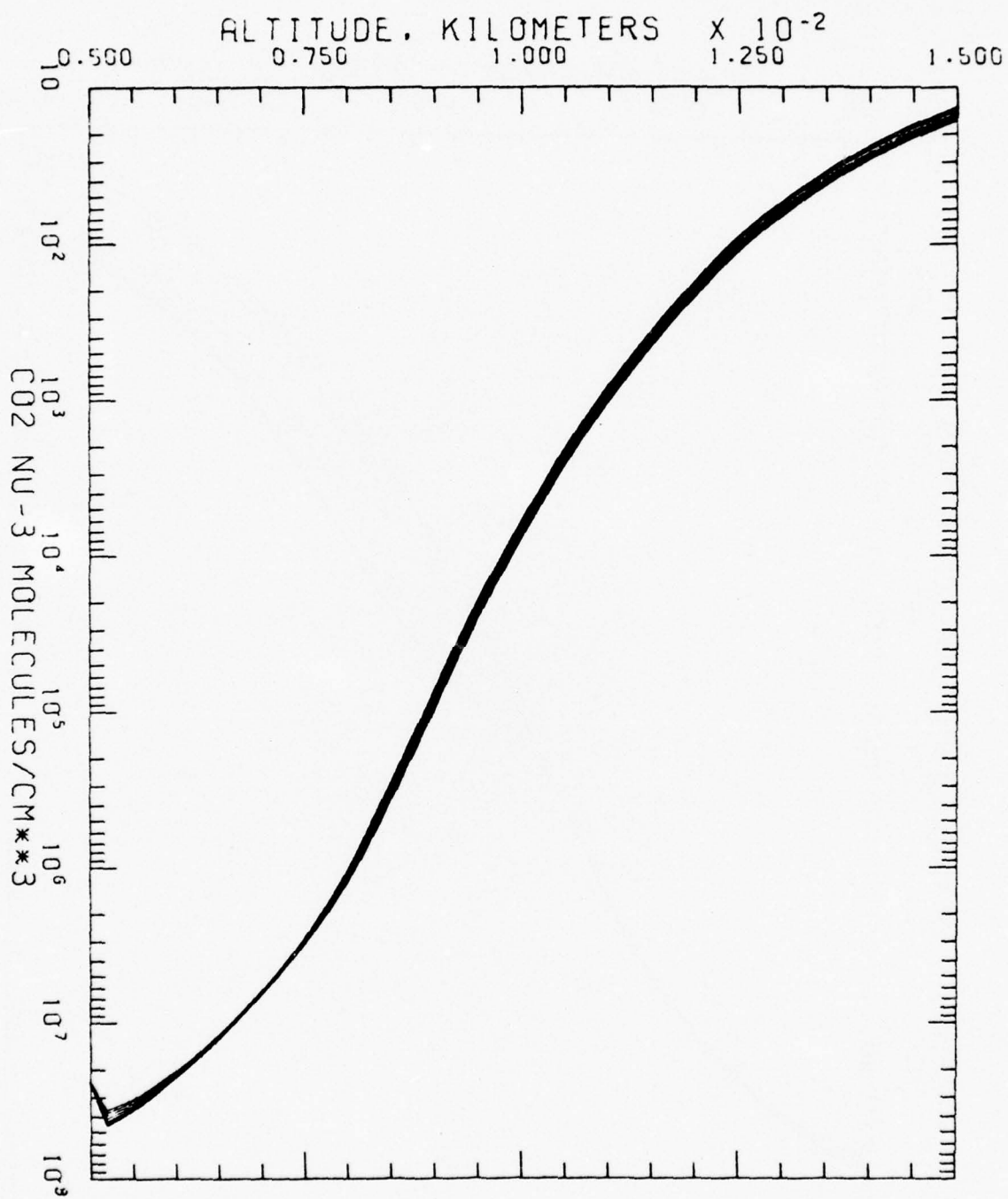


Figure 6

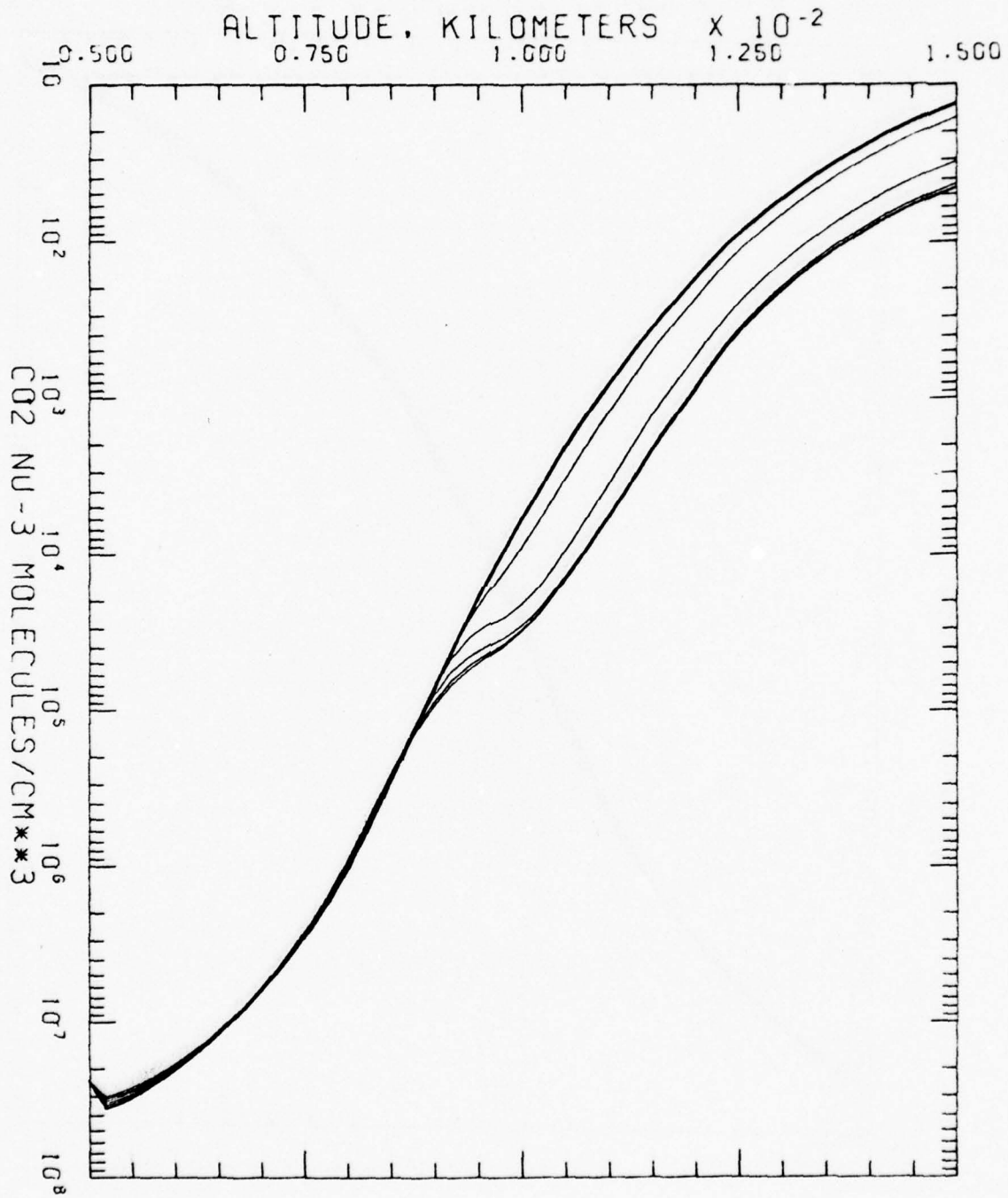


Figure 7

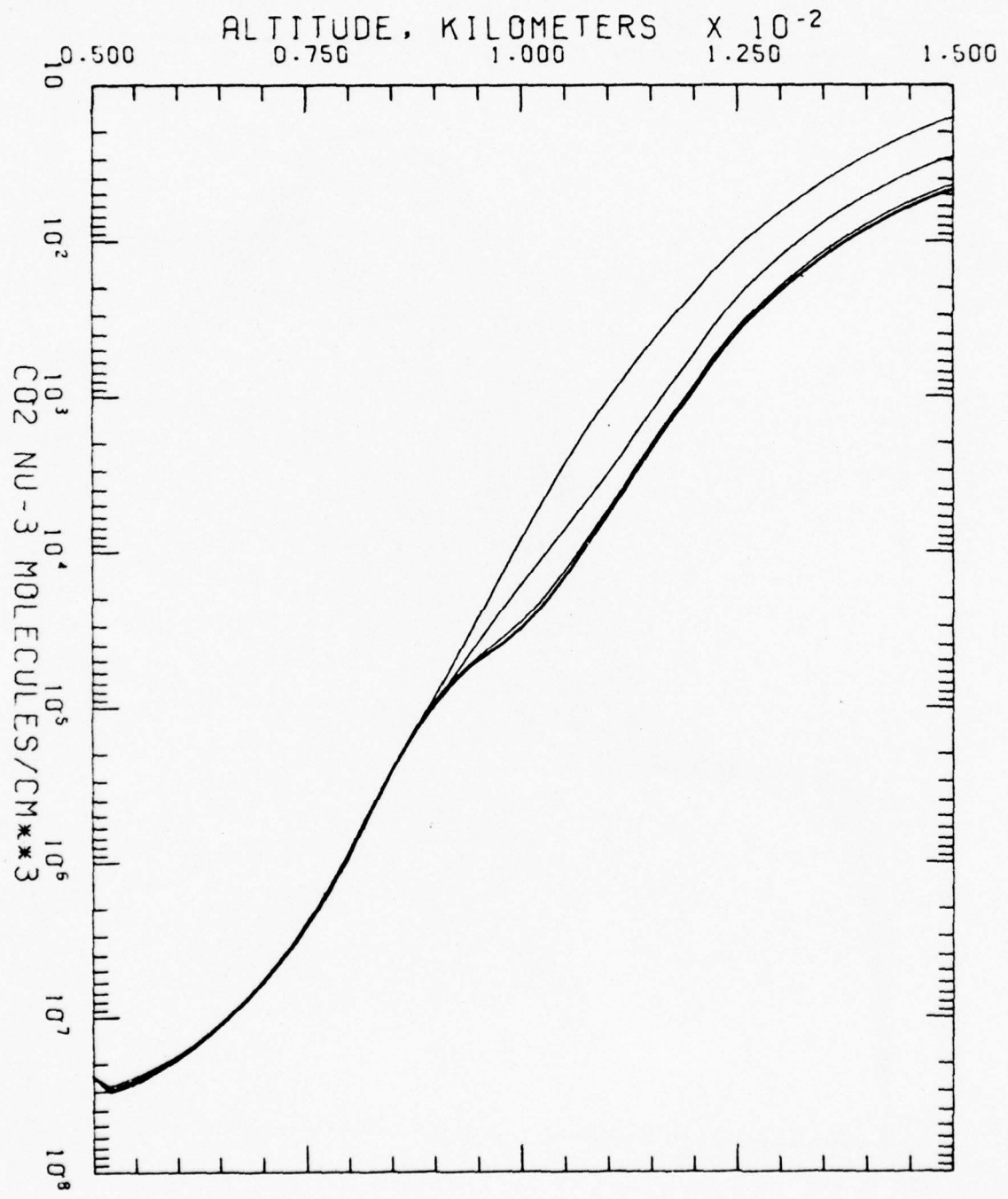


Figure 8

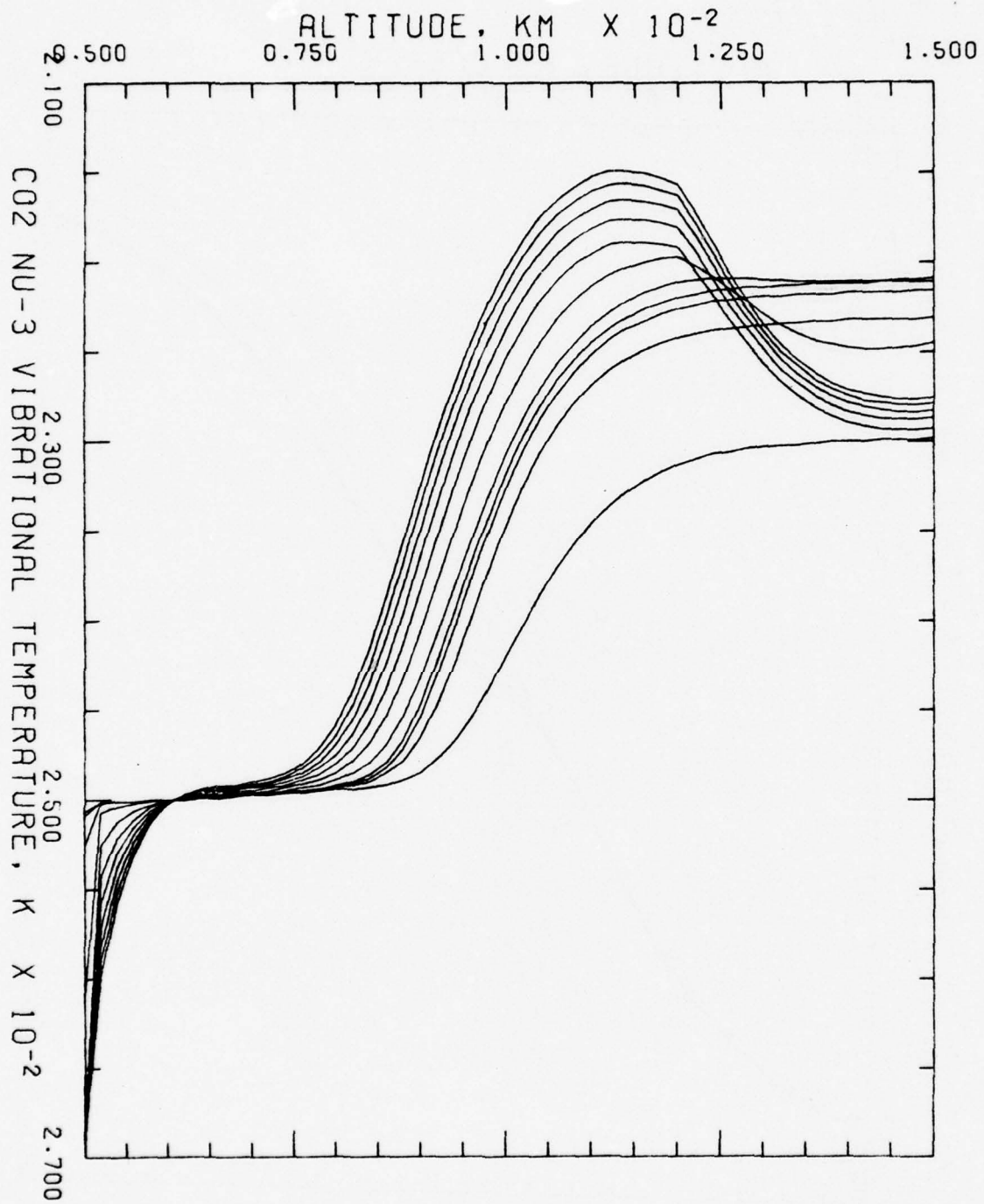


Figure 9

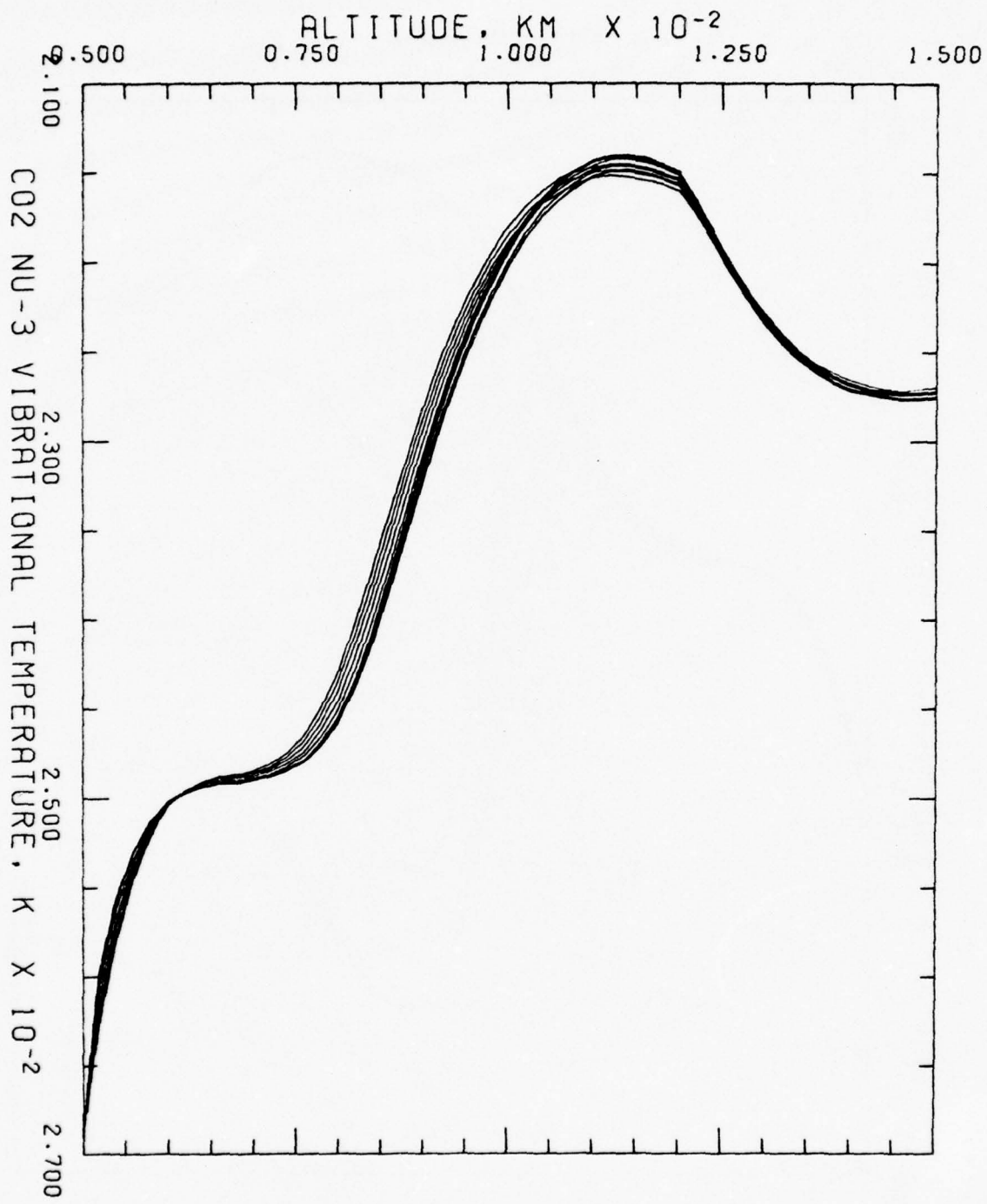


Figure 10

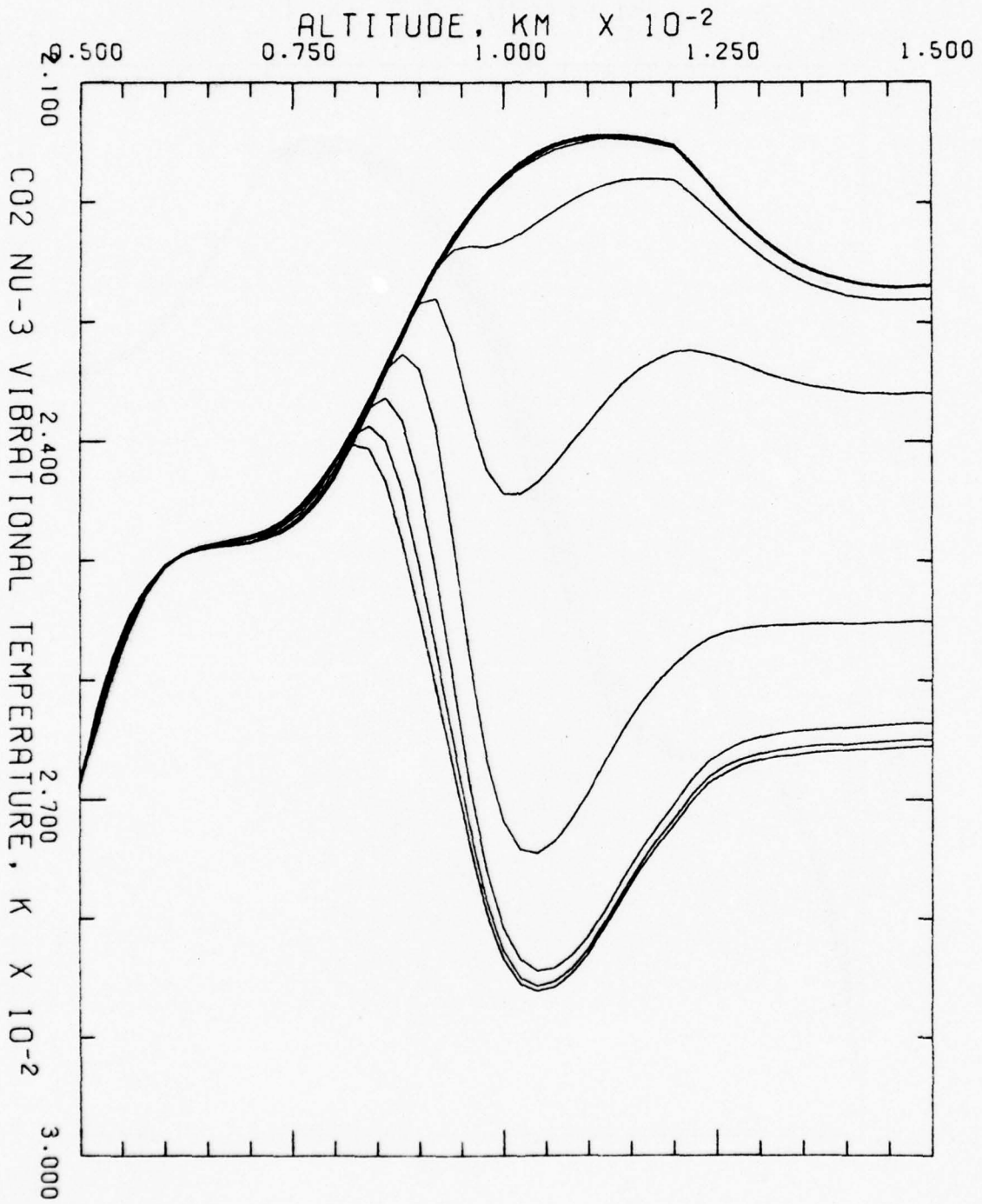


Figure 11

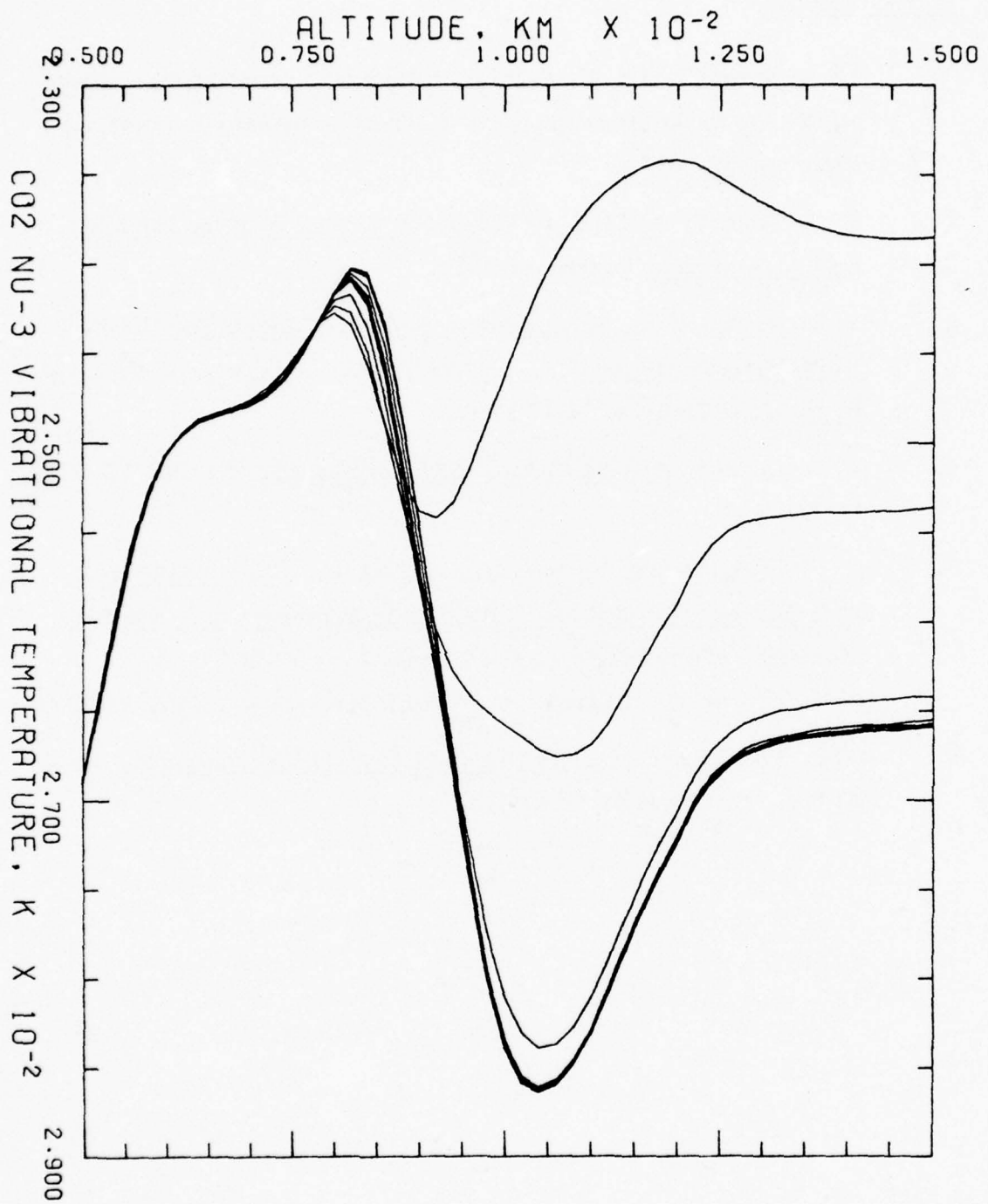


Figure 12

REFERENCES

1. M. J. Berger and S. M. Seltzer, "Energy Deposition by Auroral Electrons in the Atmosphere", *J. of Atmospheric Terrestrial Physics*, 32, 1970.
2. T. C. Degges, AFCRL-TR-74-0606, A High Altitude Infrared Radiance Model, December 1974.
3. V. L. Corbin et al, Atmospheric Radiance Models for Limb-Viewing Geometry in the Five- to Twenty-Five Micron Spectral Region, AFCRL-69-0552 (1969).
4. T. C. Degges, A High Altitude Radiance Model, AFCRL 72-0273 (1972).
5. Garvin, D., and Hampson, R. F., Editors, Chemical Kinetics Data Survey VII. Tables of Rate and Photochemical Data for Modelling of the Stratosphere (Revised). NBSIR 74-430, National Bureau of Standards, Washington, D. C., January 1974.
6. O. P. Manley et al, Modelling of Optical IR Backgrounds, AFCRL-TR-73-0565, (1973).

Appendix 1

Auroral Electron Energy Spectra

Rocket A18.219-1

Launched 25 February 1974

The data in the following figures was presented at the DNA ICECAP Data Meeting in January 1975. Rocket A 18.219-1 was launched 25 February 1975 and overflowed the same bright auroral arc twice. Peak energy deposition was in excess of $100 \text{ ergs cm}^{-2} \text{ sec}^{-1}$. The electron energy deposition was measured with two instruments, an aluminum covered scintillator coupled to a photomultiplier and an electrostatic analyzer (ESA). Figure 1 shows schematically the operation of the ESA. Spherical analyzer plates are used to select a narrow energy band. The electrons are then accelerated with a voltage applied to a thin aluminum deposition on the face of a calcium fluoride scintillator. This extends the low energy response of the instrument. By modulating the analyzer plate voltage and using a narrow band amplifier the sensitivity of the instrument is significantly improved. Figure 2 shows the scintillator measurement as a function of time. This detector measures the integrated electron flux above 4 or 5 keV. The two peaks correspond to the time when the rocket is on the magnetic field line connecting to the visible aurora. The auroral motion is presently being analyzed as part of the data analysis. The visible aurora initially is to the north, moves to the south under the rocket, and then moves to the north again passing under the rocket.

The following figures show the auroral energy spectrum measured with the ESA. The insert shows the scintillator measurement and the inverted triangle indicates when that electron energy spectrum was taken. The auroral peak energy extended beyond 30 keV and showed significant spectral differences north and south of the peak region. The spectral form north of the peak region was much softer than that south of the peak region. These spectral differences persisted throughout the flight. The most striking feature is that the electron spectral description of the auroral form varied very little while the form moved rapidly in the sky. The detailed analysis of this aurora will be presented in a later report.

The data in the following figures was presented at the DNA ICECAP Data Meeting in January 1975. Rocket A 18,219-1 was launched 25 February 1975 and overflowed the same bright auroral arc twice. Peak energy deposition was in excess of $100 \text{ ergs cm}^{-2} \text{ sec}^{-1}$. The electron energy deposition was measured with two instruments, an aluminum covered scintillator coupled to a photomultiplier and an electrostatic analyzer (ESA). Figure 1 shows schematically the operation of the ESA. Spherical analyzer plates are used to select a narrow energy band. The electrons are then accelerated with a voltage applied to a thin aluminum deposition on the face of a calcium fluoride scintillator. This extends the low energy response of the instrument. By modulating the analyzer plate voltage and using a narrow band amplifier the sensitivity of the instrument is significantly improved. Figure 2 shows the scintillator measurement as a function of time. This detector measures the integrated electron flux above 4 or 5 keV. The two peaks correspond to the time when the rocket is on the magnetic field line connecting to the visible aurora. The auroral motion is presently being analyzed as part of the data analysis. The visible aurora initially is to the north, moves to the south under the rocket, and then moves to the north again passing under the rocket.

The following figures show the auroral energy spectrum measured with the ESA. The insert shows the scintillator measurement and the inverted triangle indicates when that electron energy spectrum was taken. The auroral peak energy extended beyond 30 keV and showed significant spectral differences north and south of the peak region. The spectral form north of the peak region was much softer than that south of the peak region. These spectral differences persisted throughout the flight. The most striking feature is that the electron spectral description of the auroral form varied very little while the form moved rapidly in the sky. The detailed analysis of this aurora will be presented in a later report.

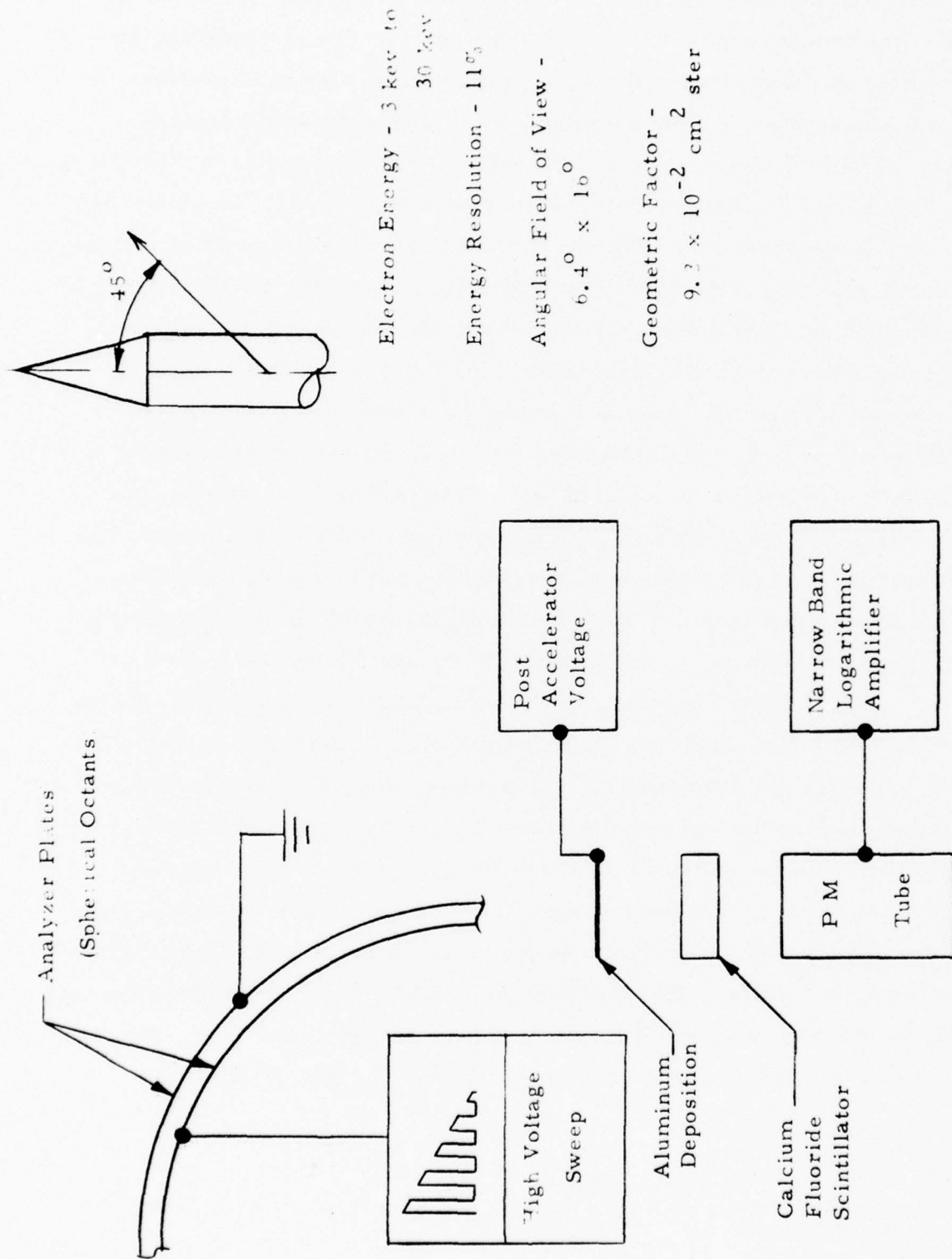


FIGURE 1:

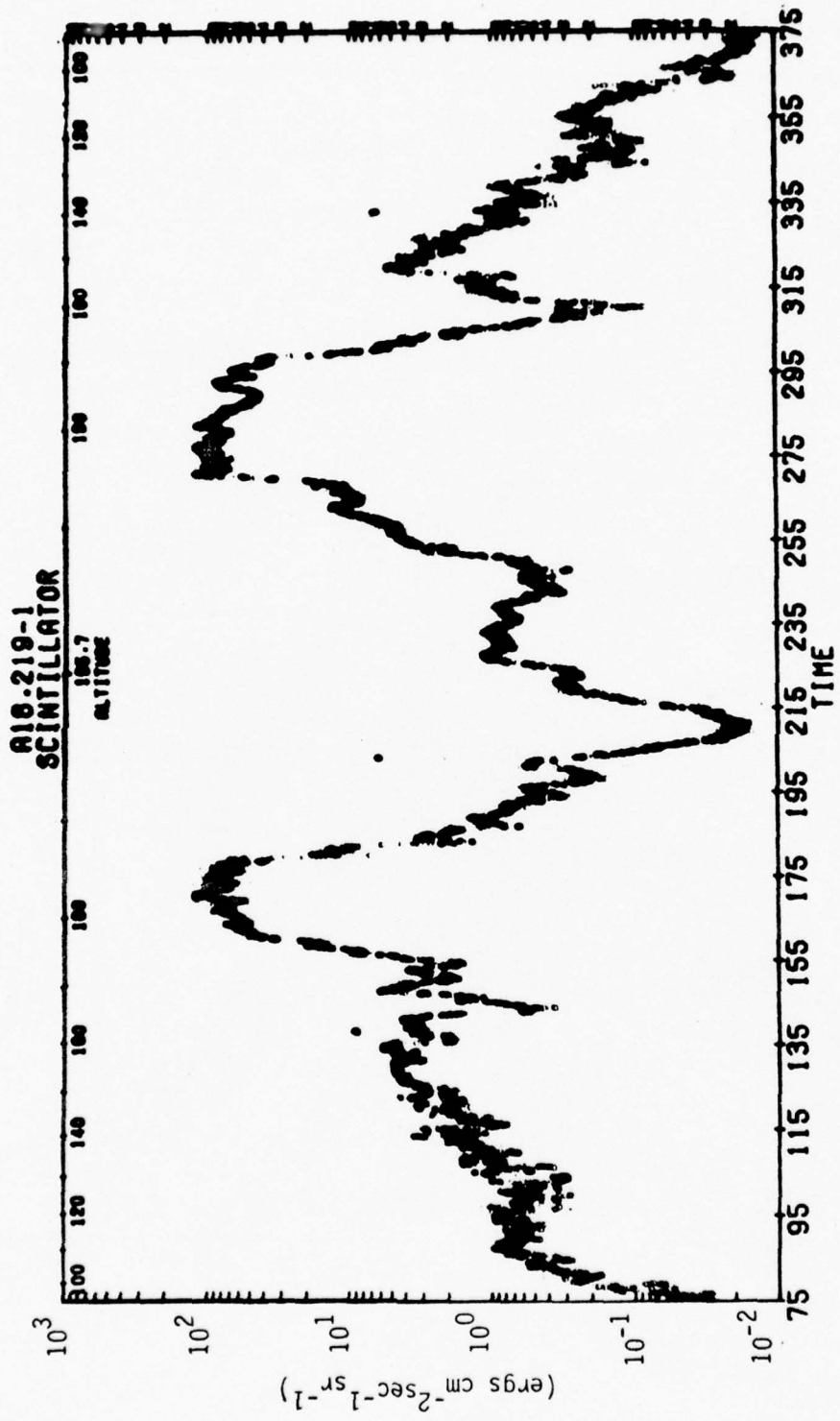


FIGURE 2:

DIFFERENTIAL FLUX VS. ENERGY. ROCKET A18.219-1

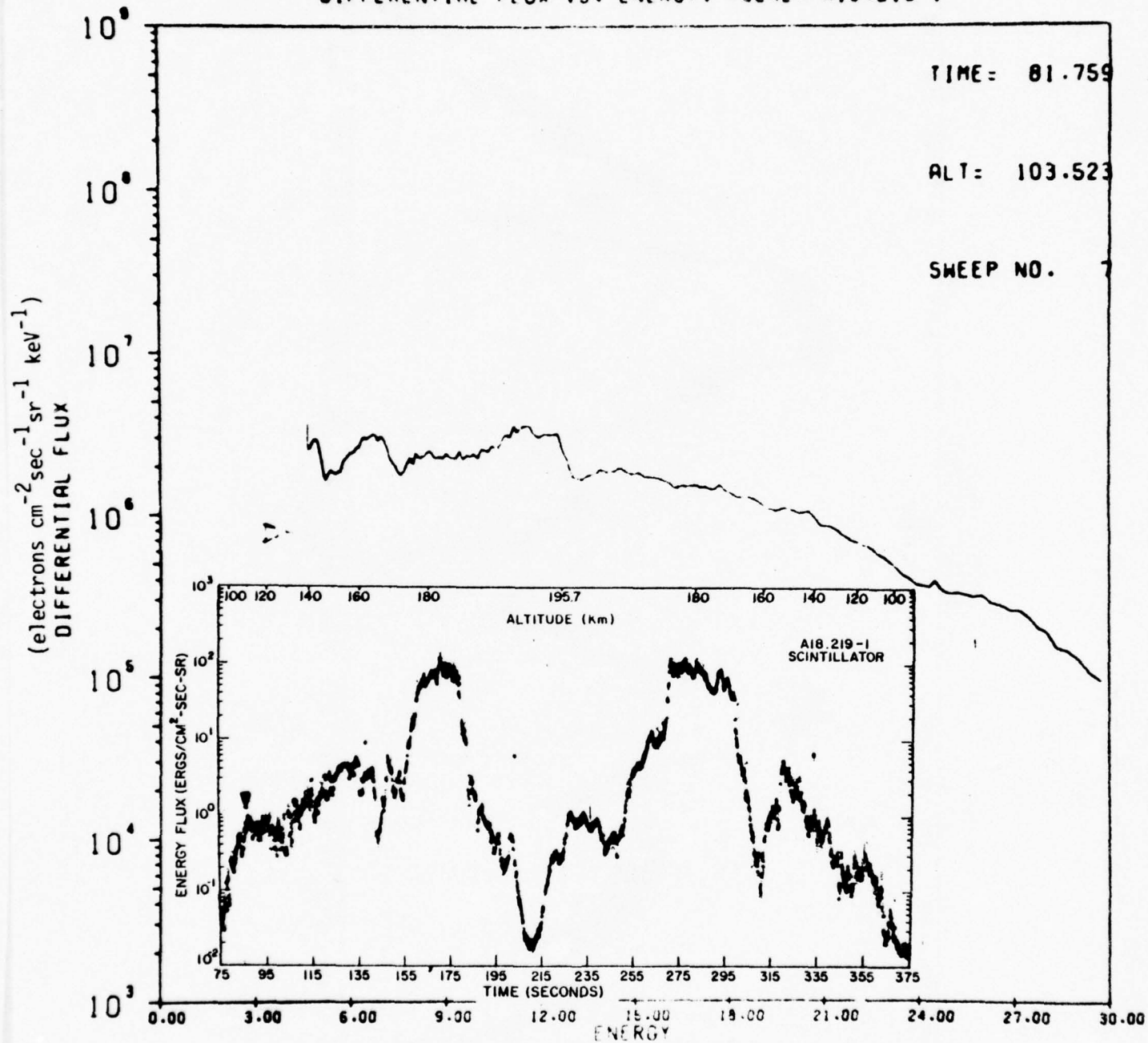


FIGURE 3:

DIFFERENTIAL FLUX VS. ENERGY. ROCKET A10.219-1

TIME = 104.015

ALT = 130.35

SWEEP NO. 50

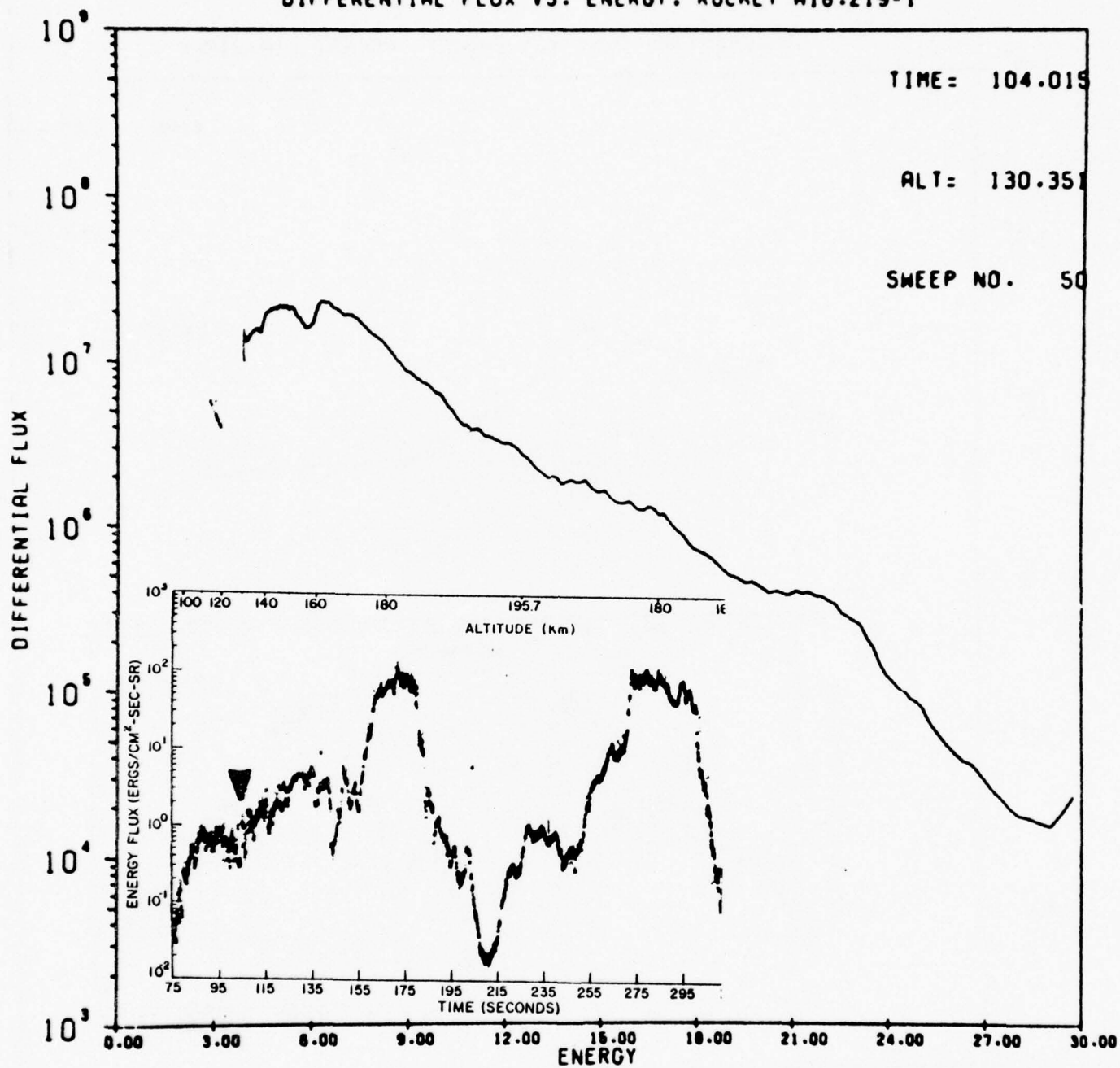


FIGURE 4:

DIFFERENTIAL FLUX VS. ENERGY. ROCKET A18.219-1

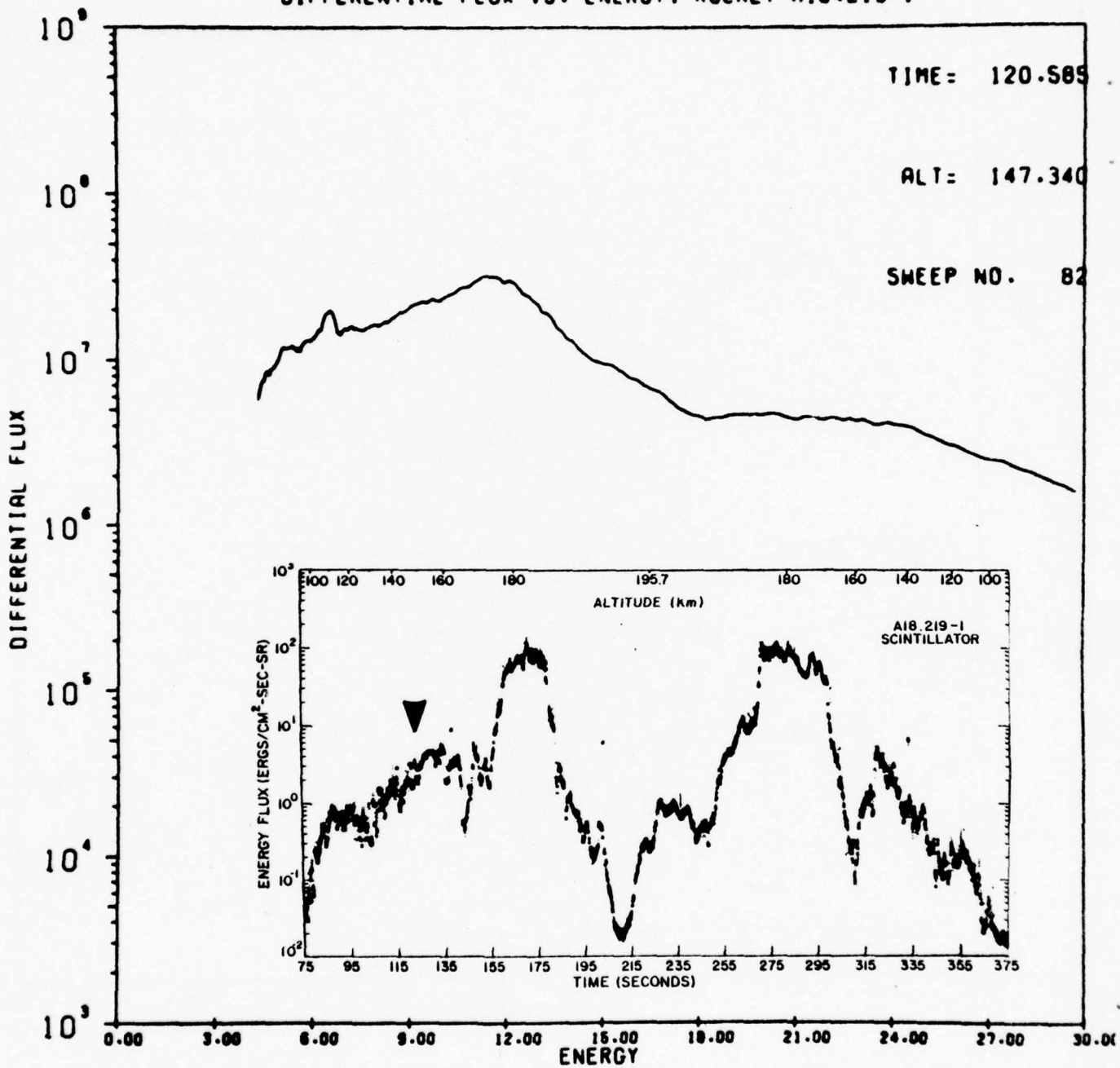


FIGURE 5:

DIFFERENTIAL FLUX VS. ENERGY. ROCKET A18.219-1

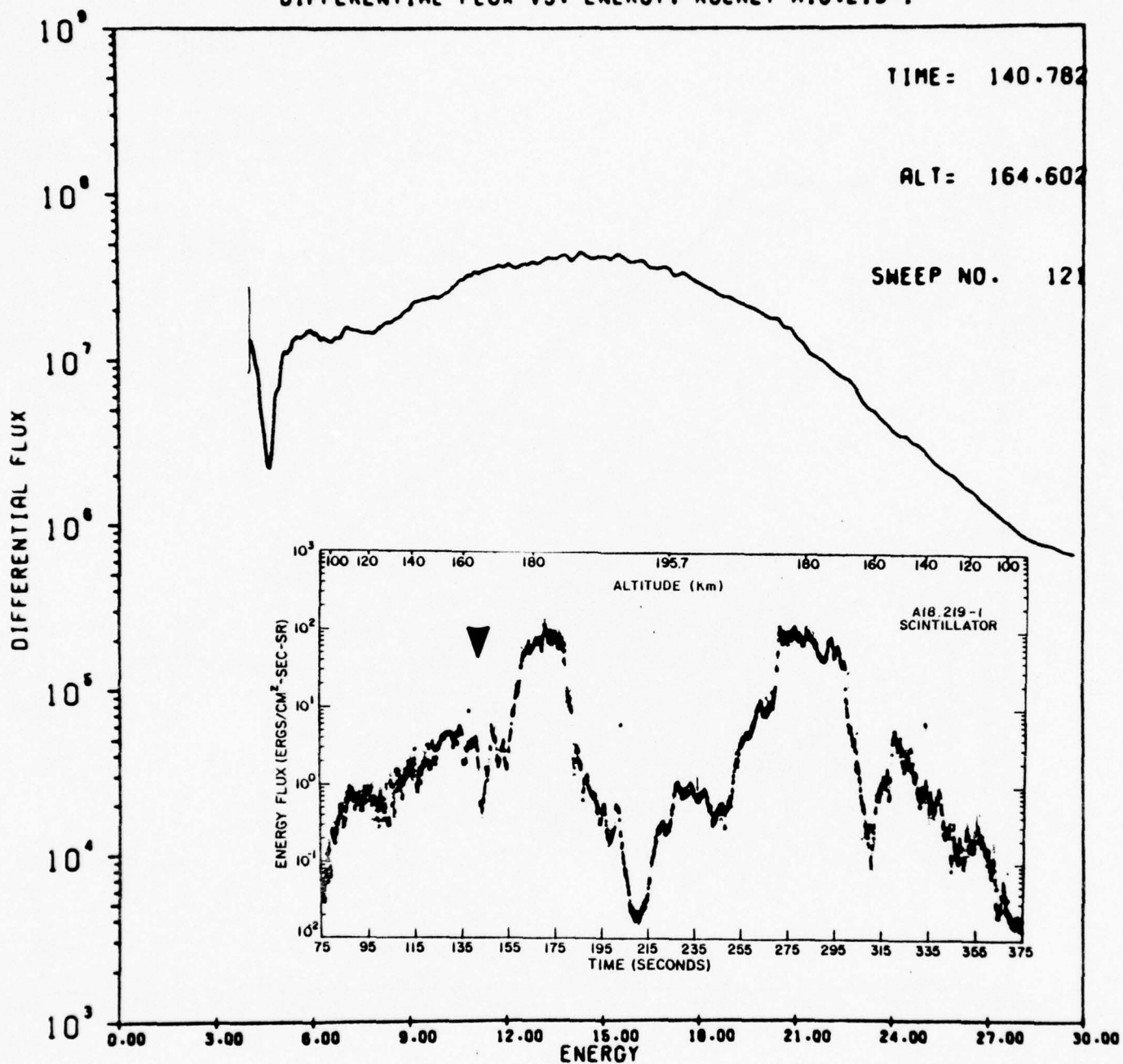


FIGURE 6:

DIFFERENTIAL FLUX VS. ENERGY. ROCKET A10.219-1

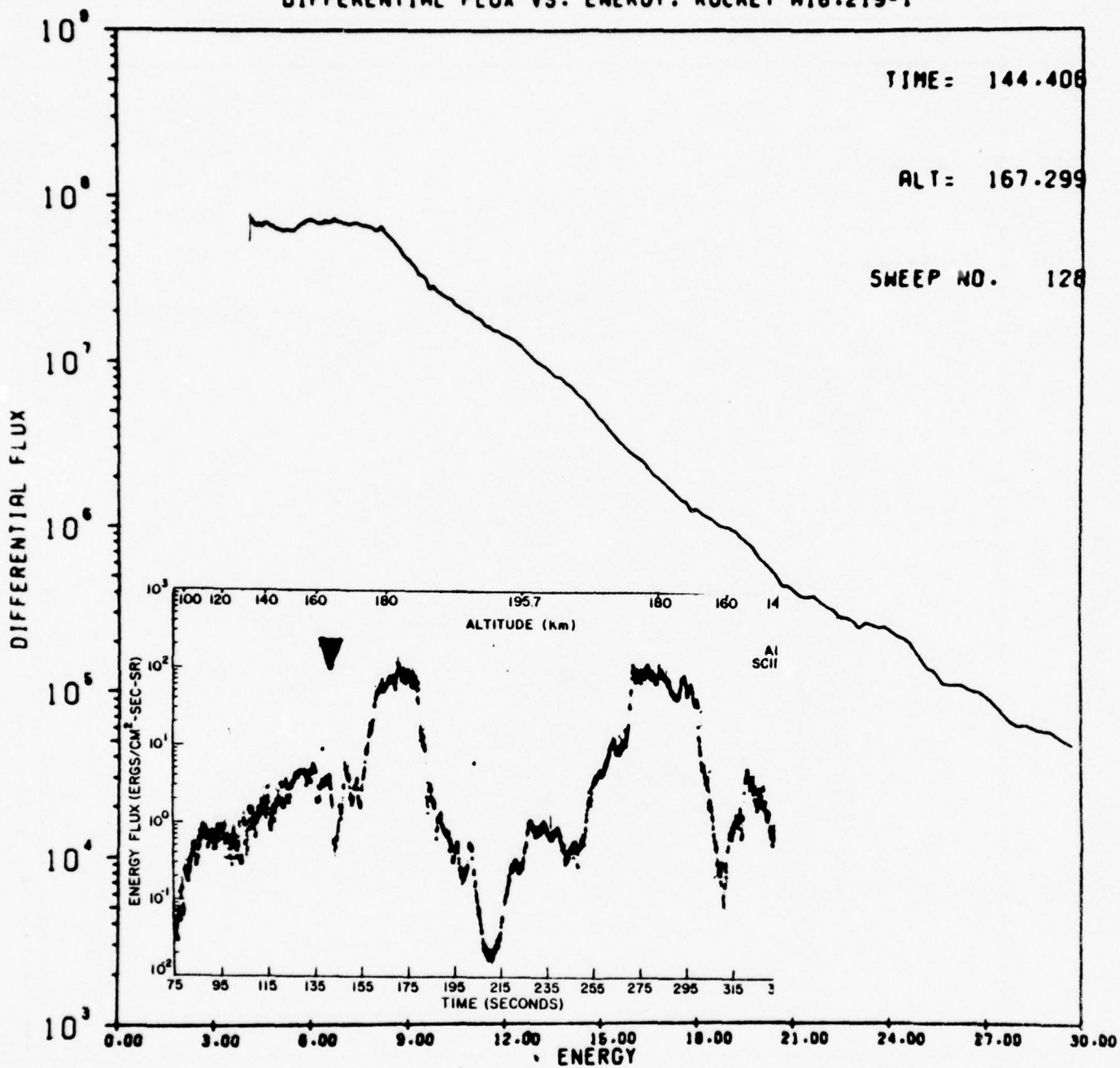


FIGURE 7:

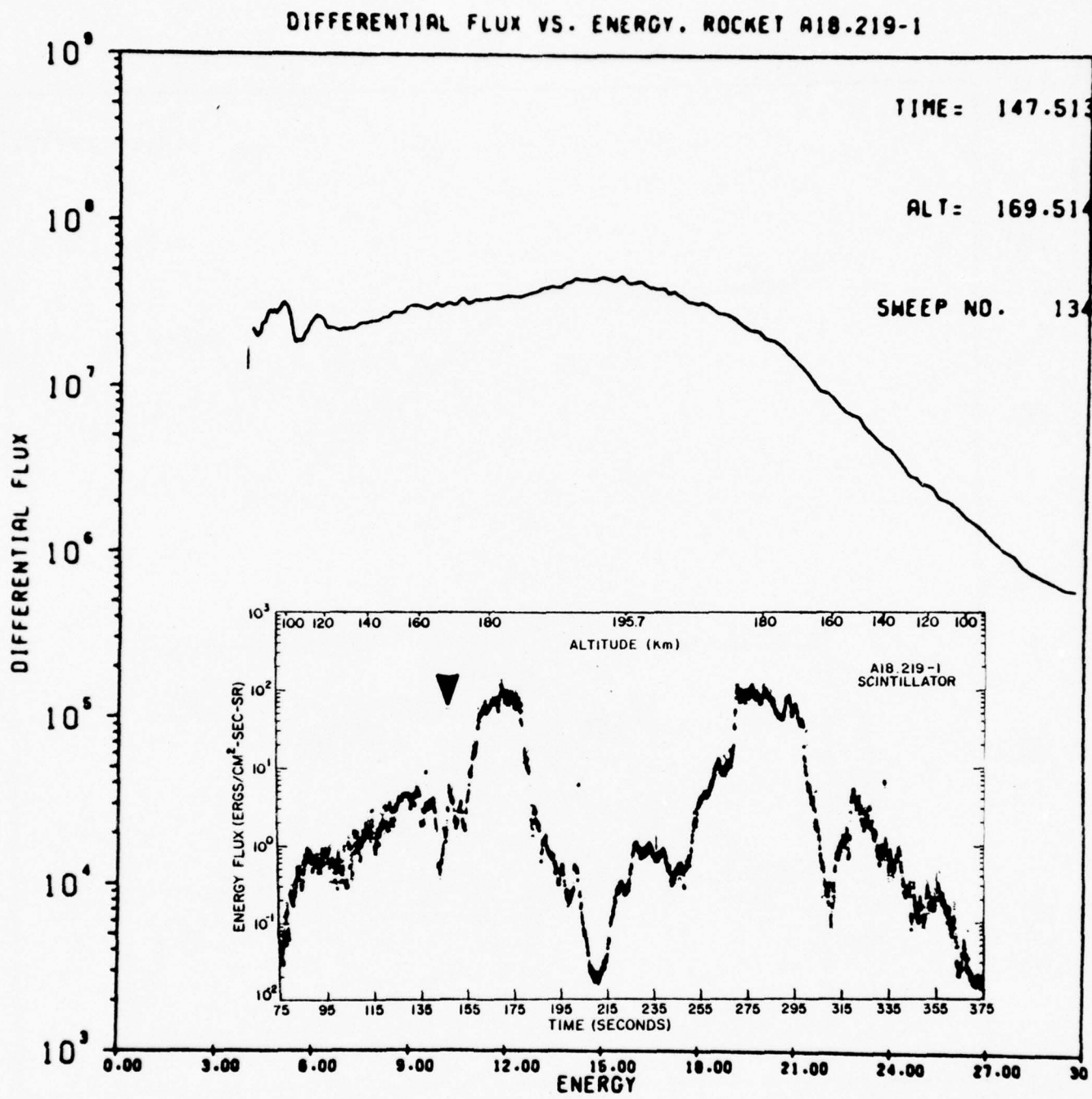


FIGURE 8:

DIFFERENTIAL FLUX VS. ENERGY. ROCKET A10.219-1

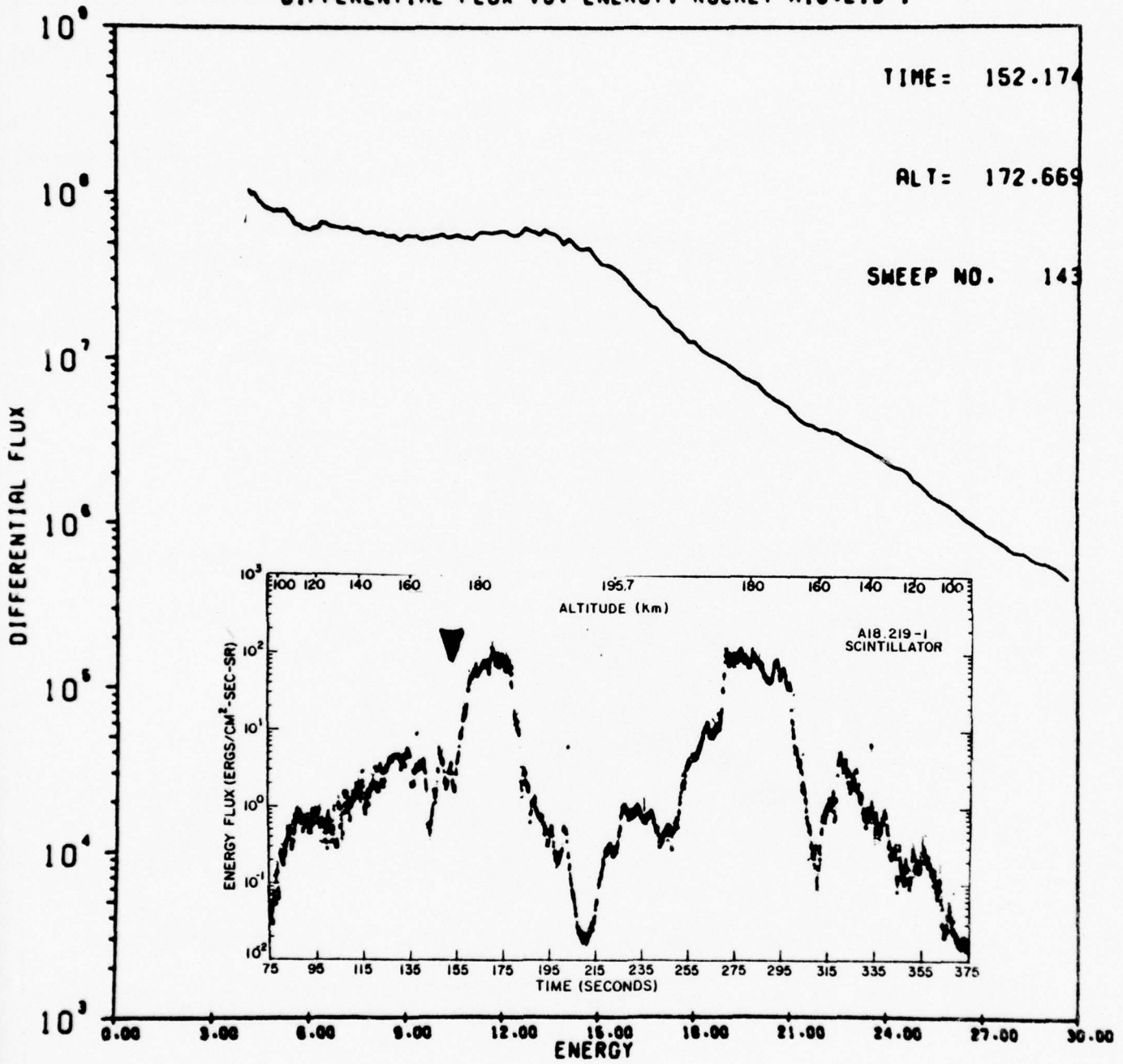


FIGURE 9:

DIFFERENTIAL FLUX VS. ENERGY. ROCKET A18.219-1

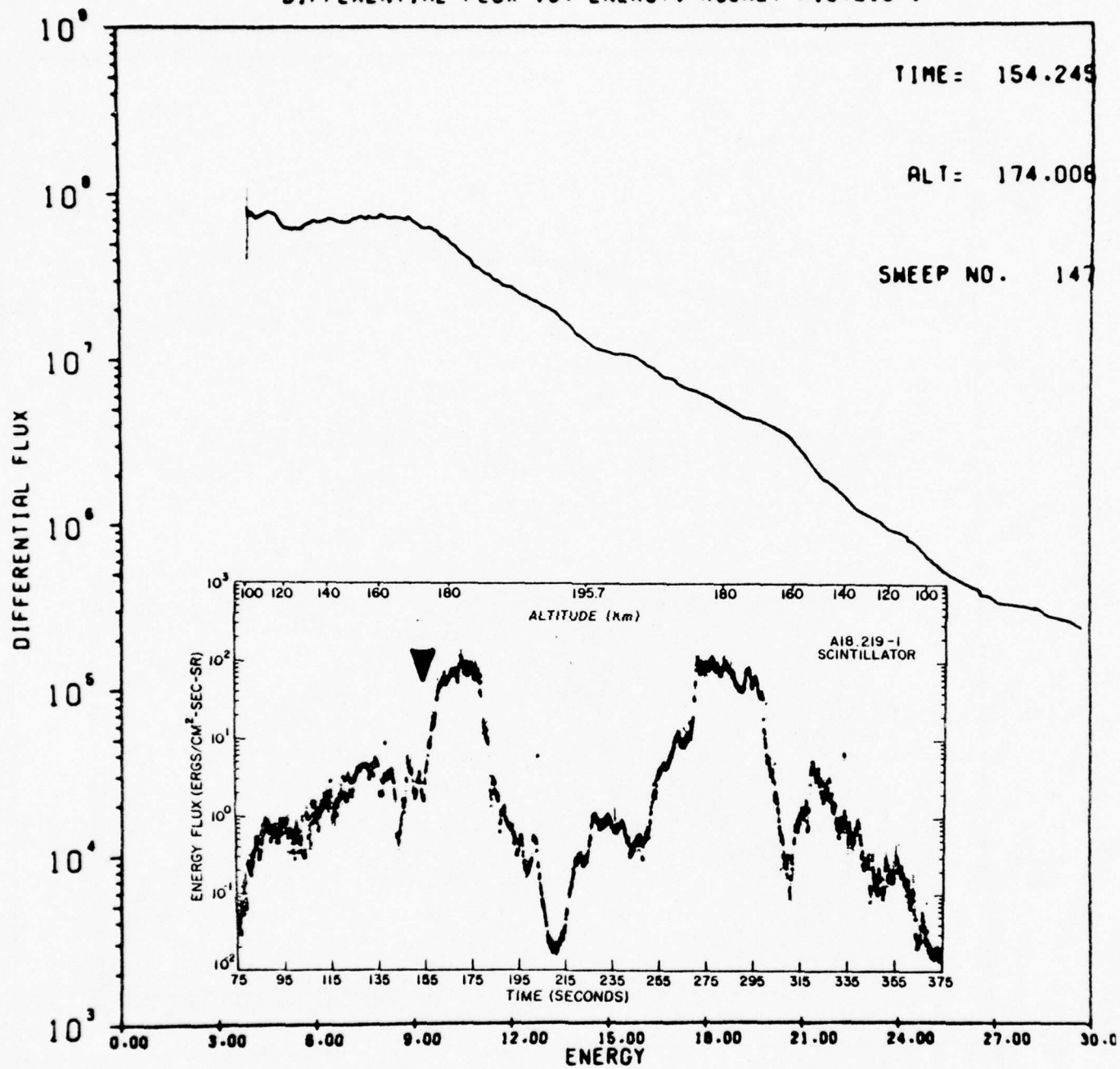


FIGURE 10:

DIFFERENTIAL FLUX VS. ENERGY. ROCKET A18.219-1

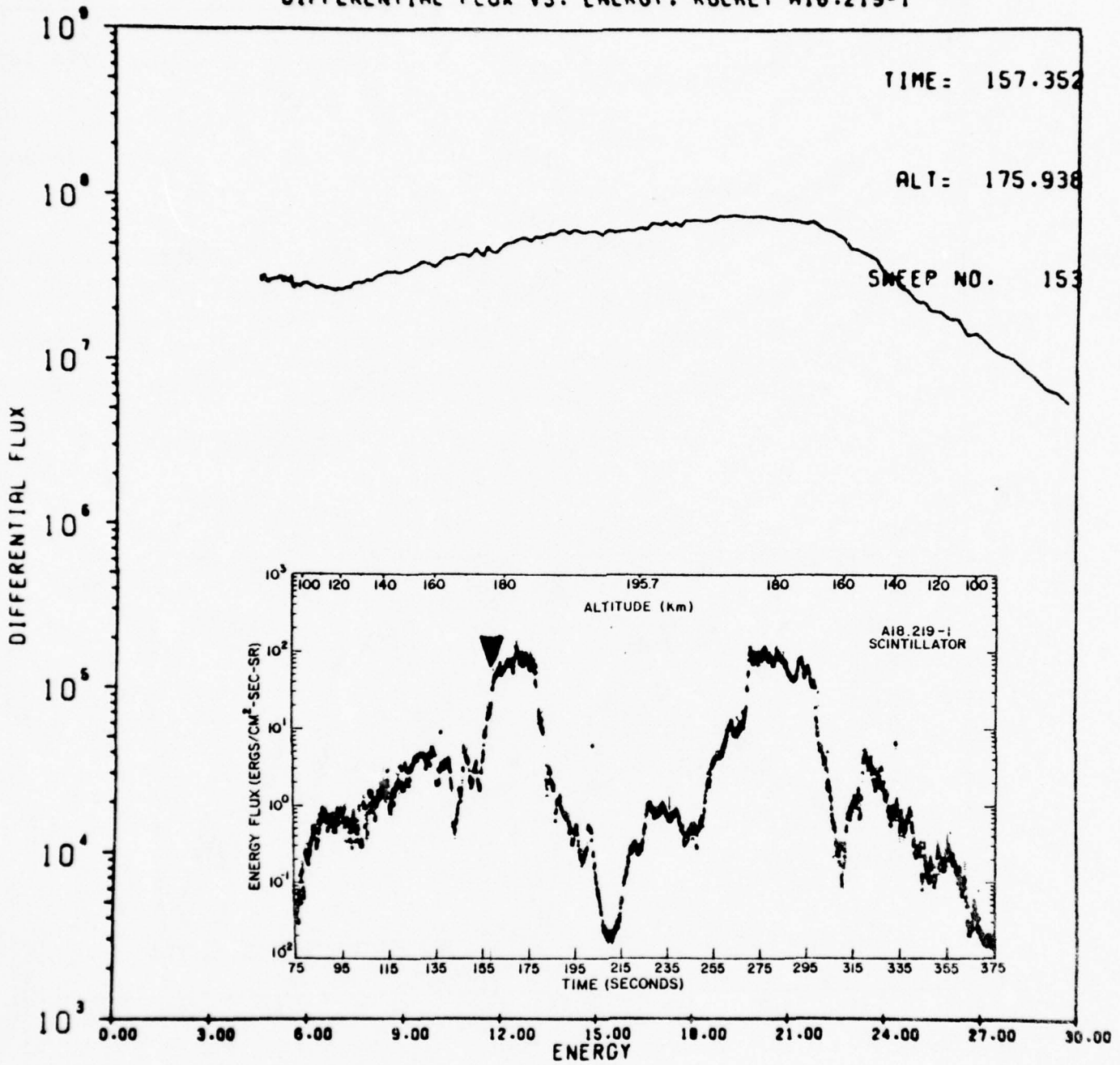


FIGURE 11:

DIFFERENTIAL FLUX VS. ENERGY. ROCKET A18.219-1

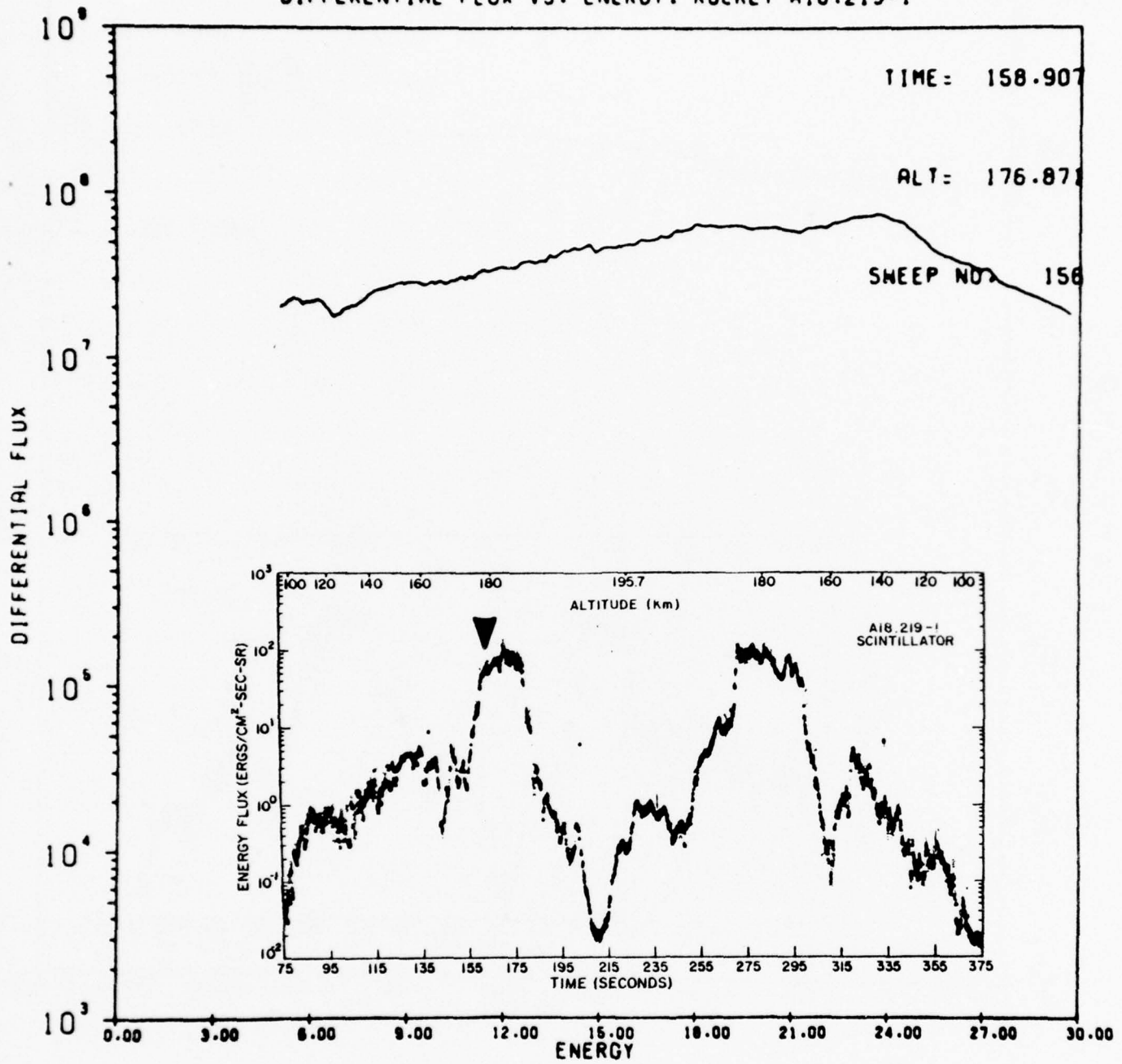


FIGURE 12:

DIFFERENTIAL FLUX VS. ENERGY. ROCKET A18-219-1

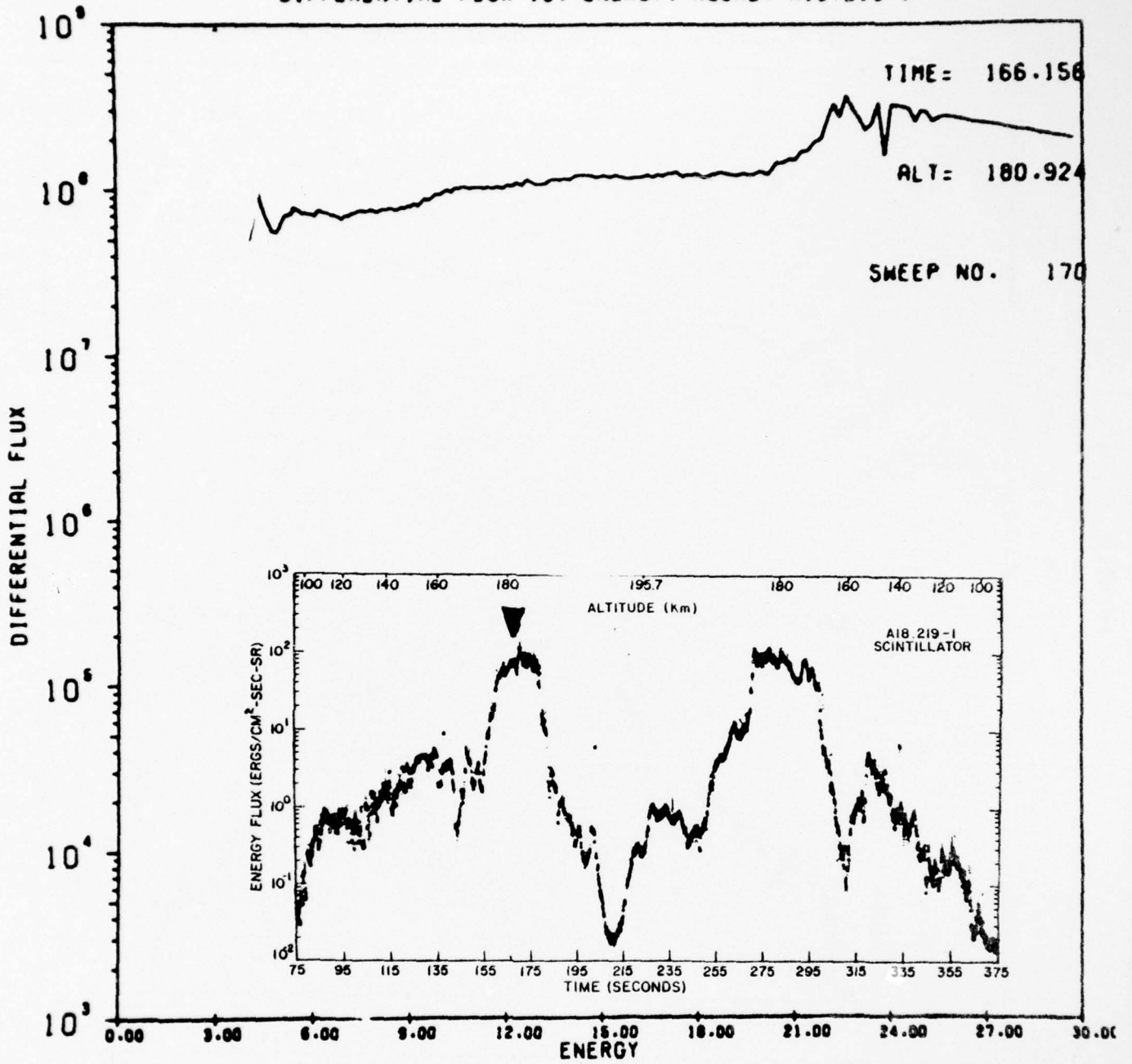


FIGURE 13

DIFFERENTIAL FLUX VS. ENERGY. ROCKET A18-219-1

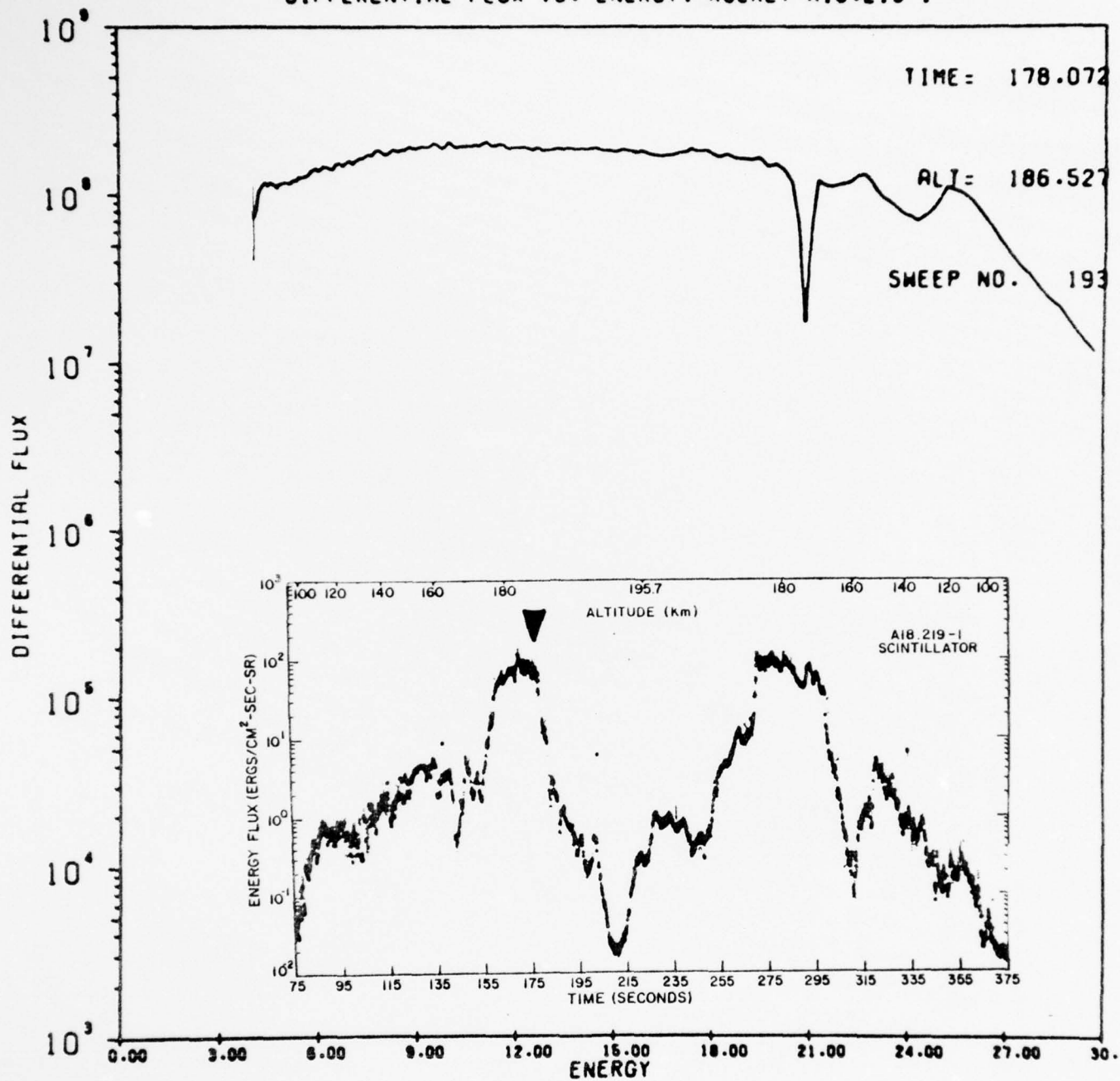


FIGURE 14

DIFFERENTIAL FLUX VS. ENERGY. ROCKET A18.219-1

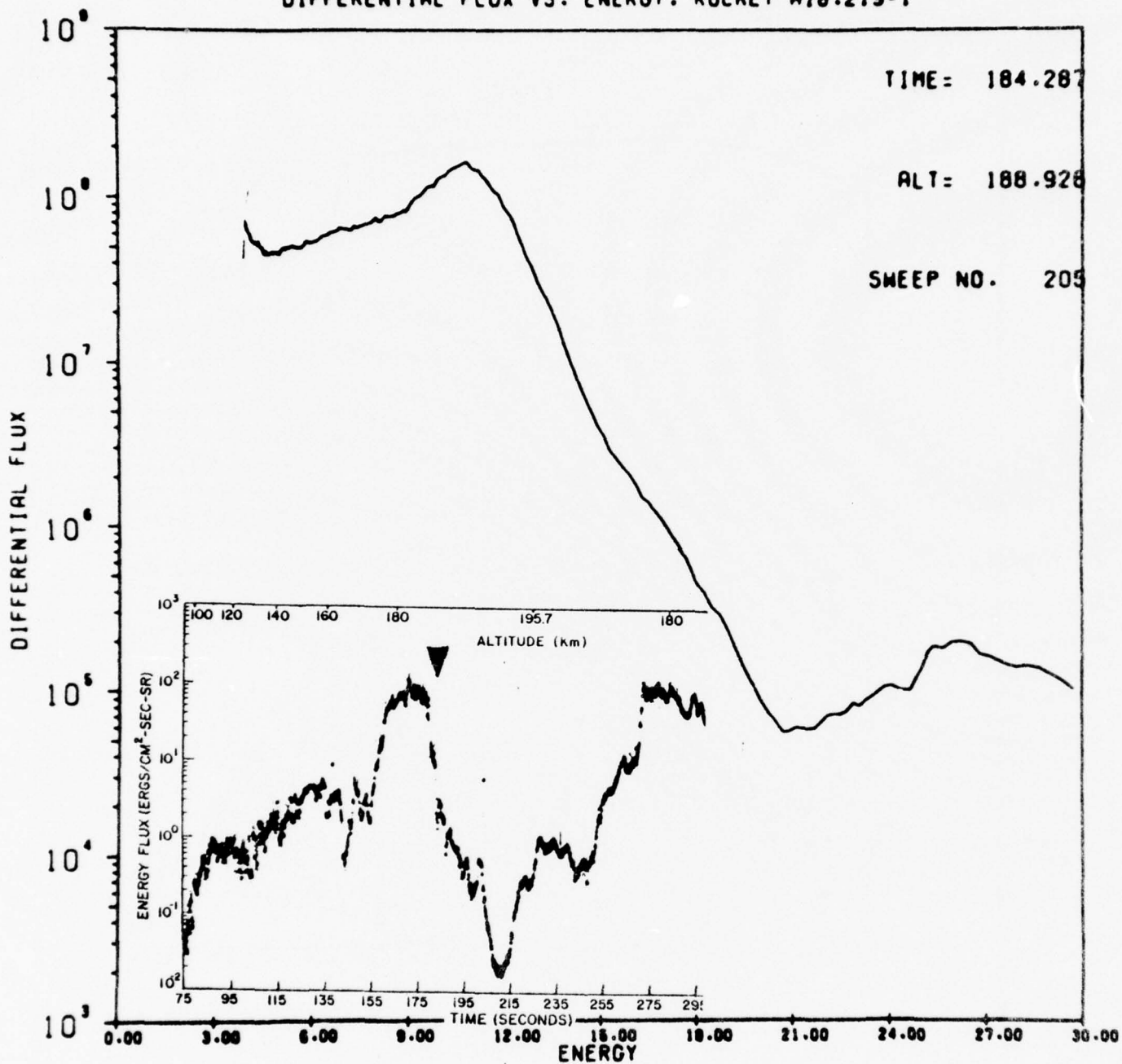


FIGURE 15

DIFFERENTIAL FLUX VS. ENERGY. ROCKET A18.219-1

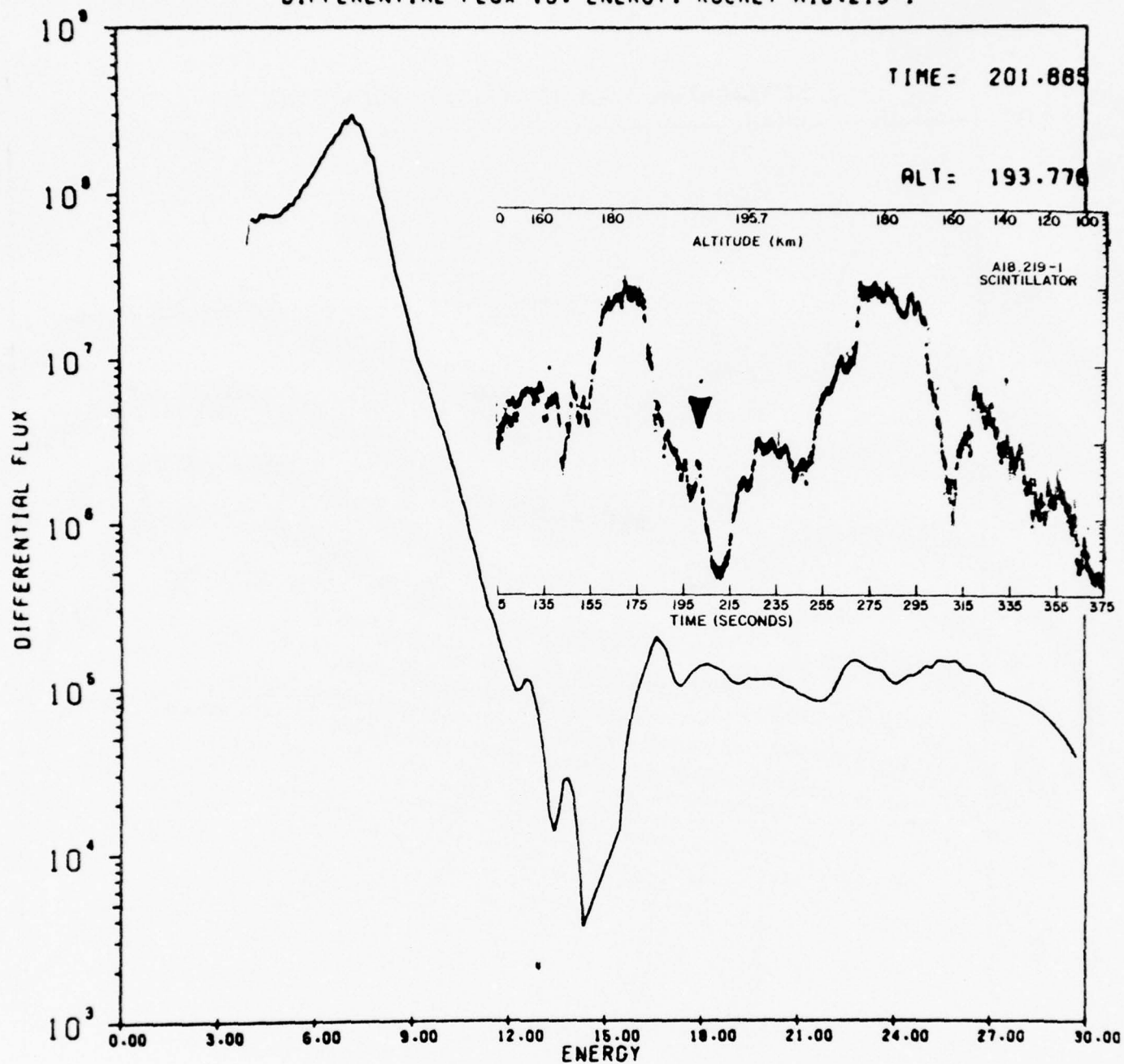


FIGURE 16

DIFFERENTIAL FLUX VS. ENERGY. ROCKET A18-219-1

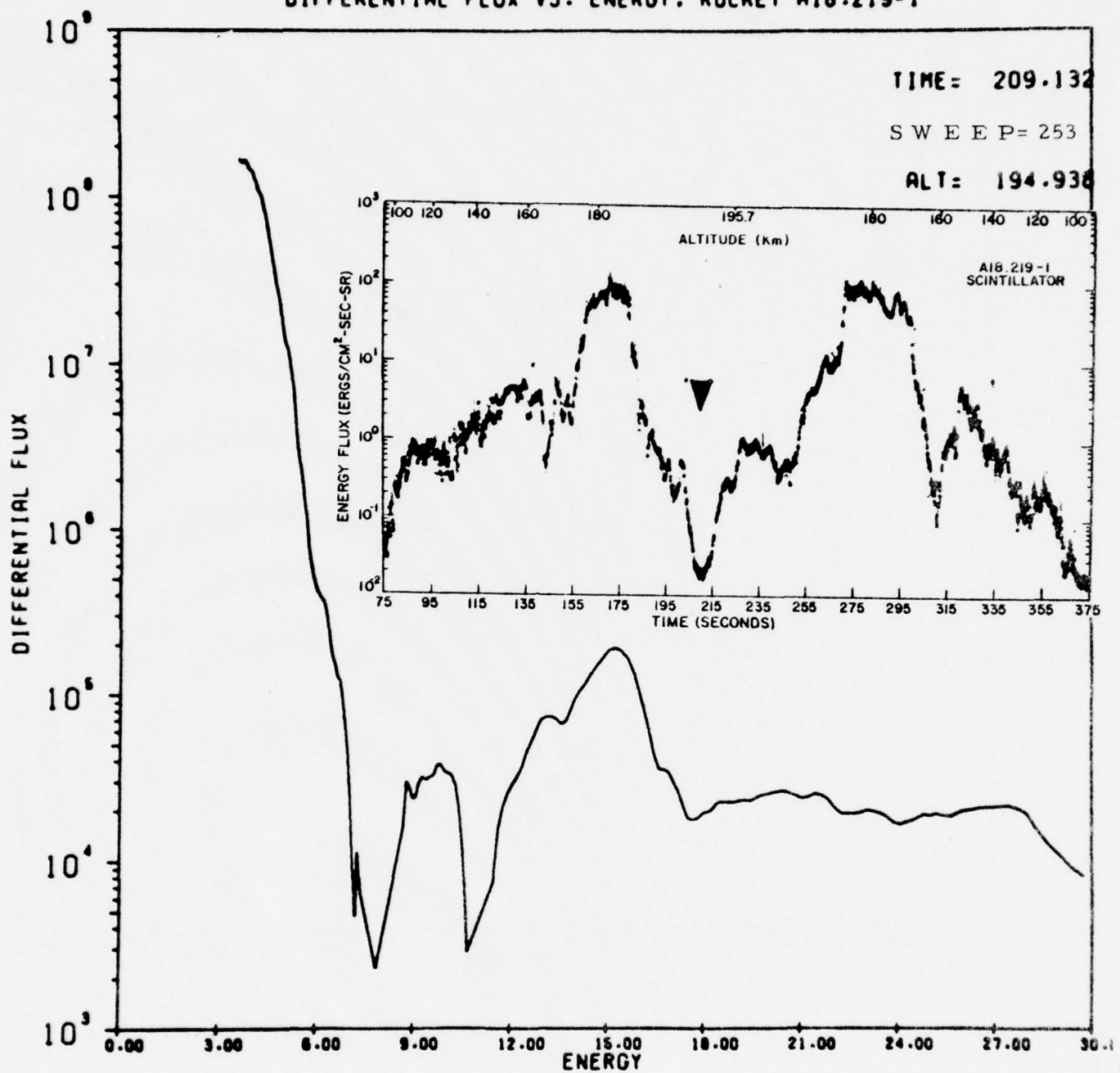


FIGURE 17

DIFFERENTIAL FLUX VS. ENERGY. ROCKET A18.219-1

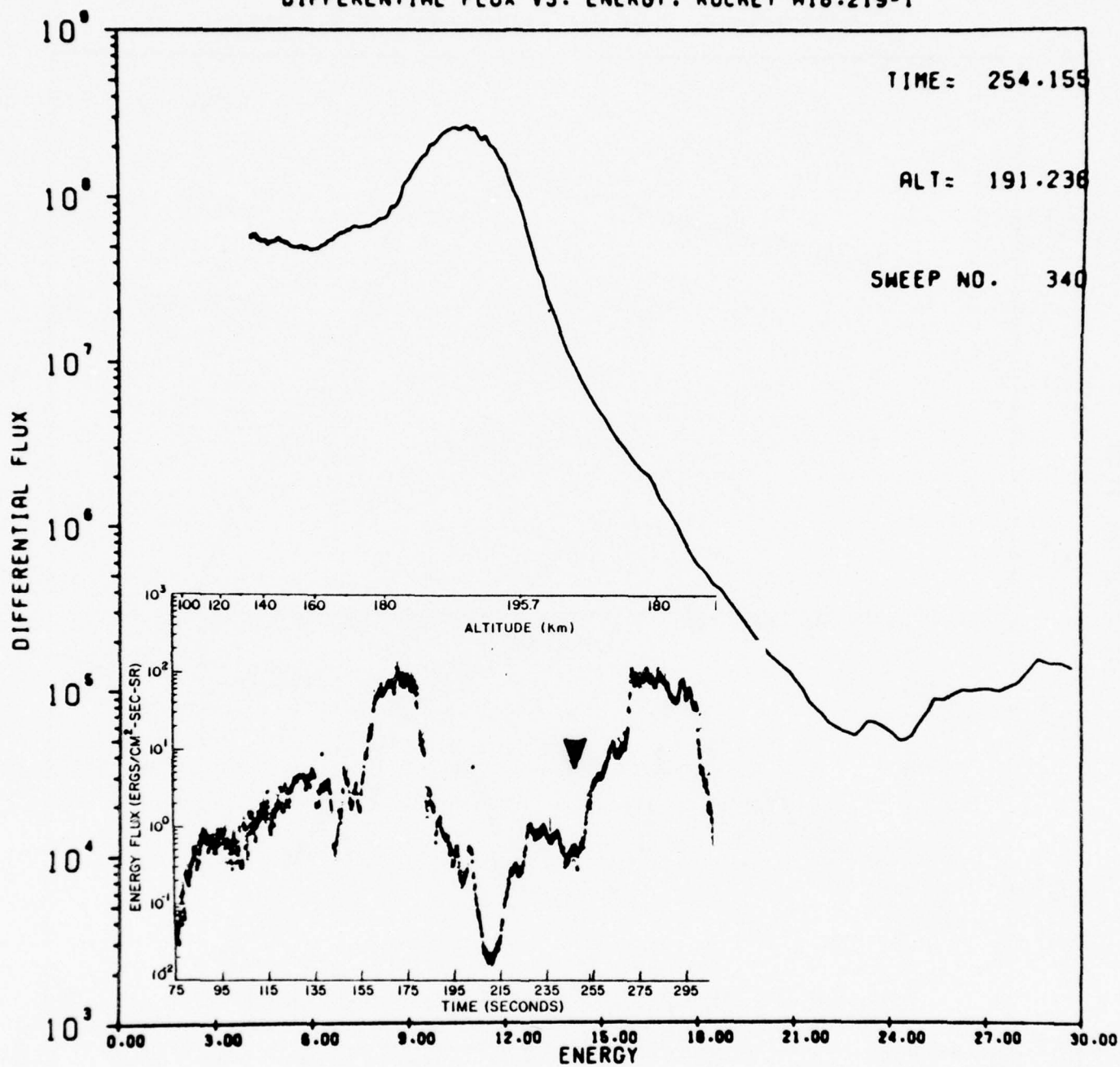


FIGURE 18

DIFFERENTIAL FLUX VS. ENERGY. ROCKET A18.219-1

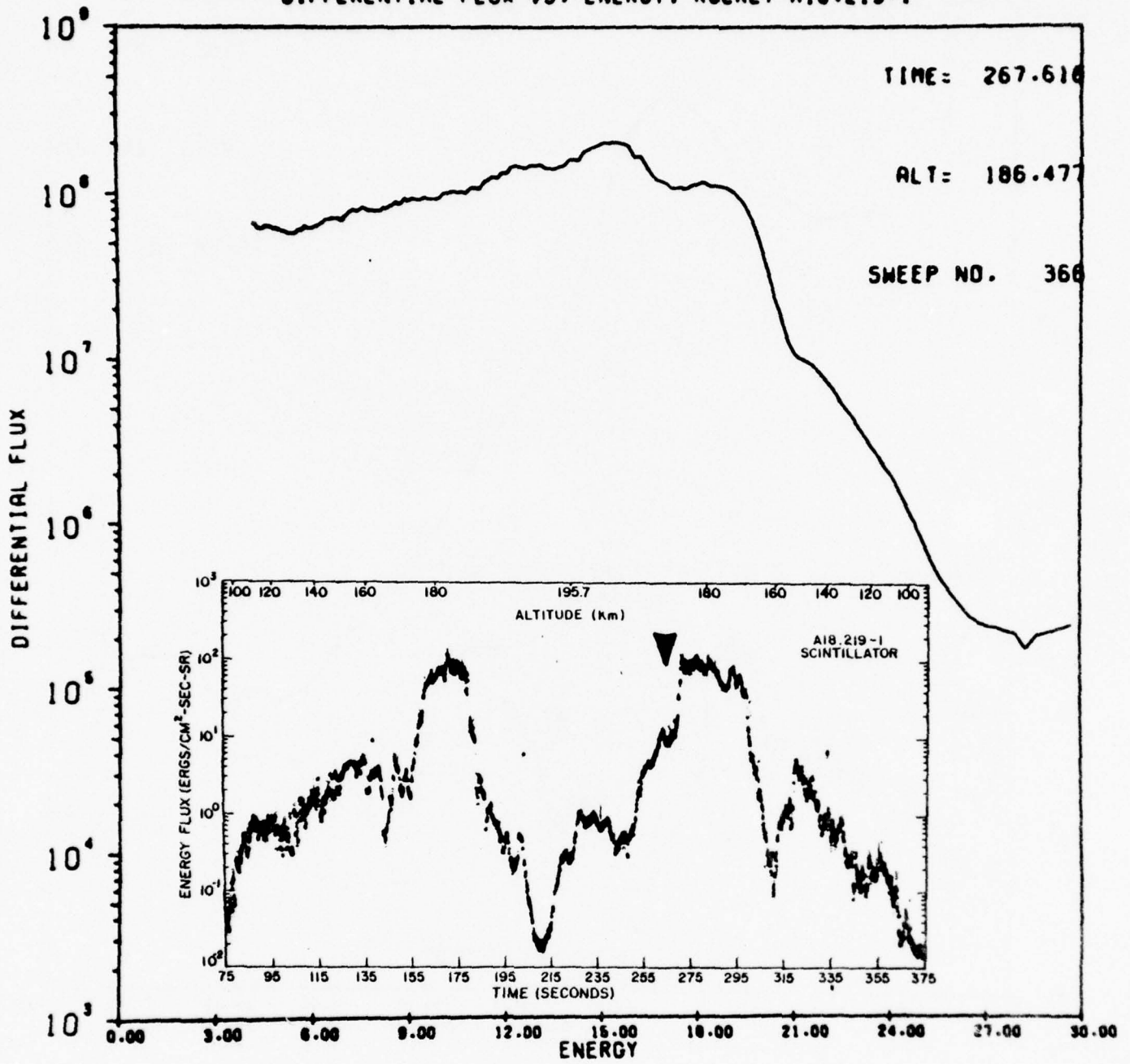


FIGURE 19

DIFFERENTIAL FLUX VS. ENERGY. ROCKET A18.219-1

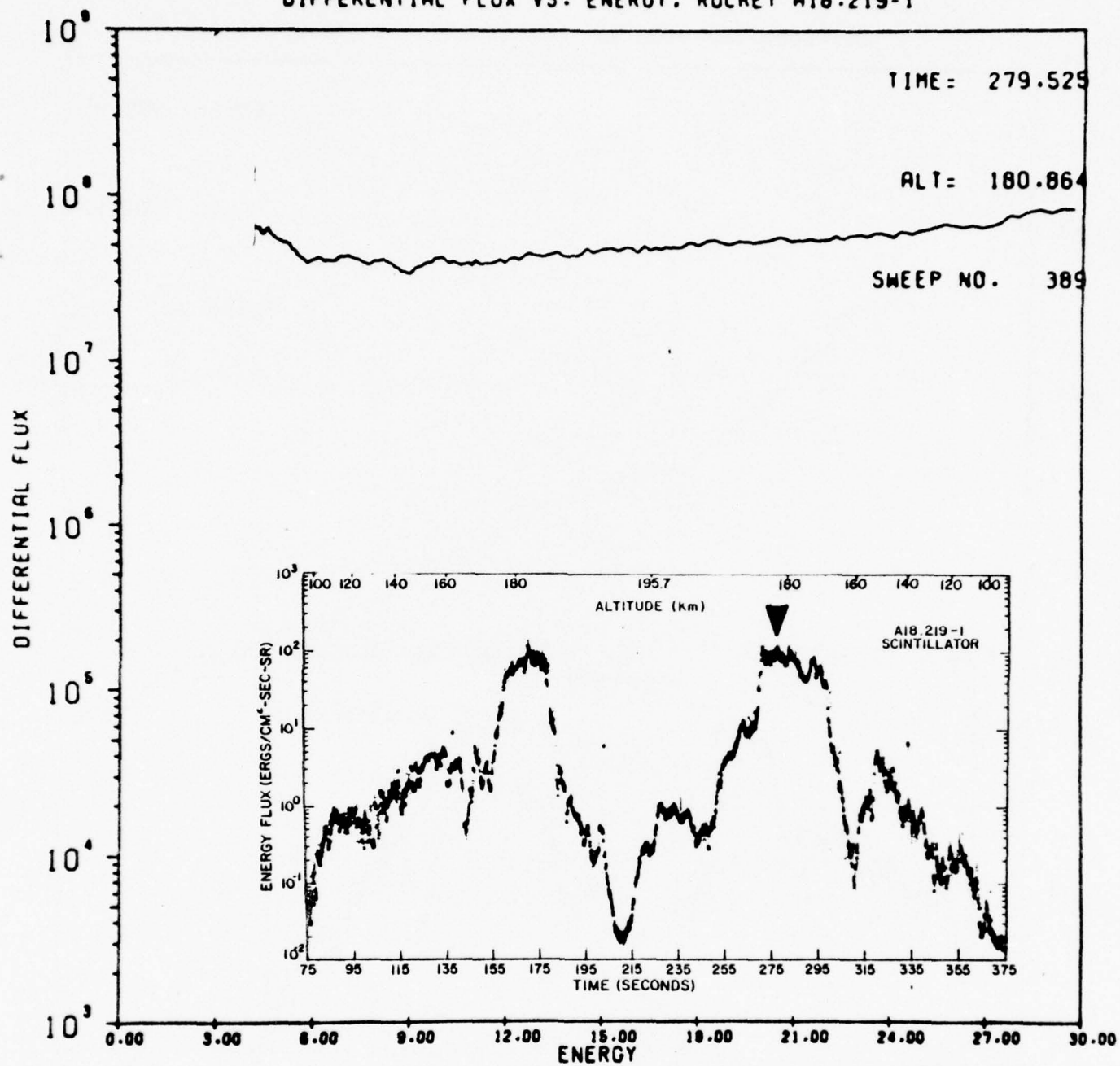


FIGURE 20

DIFFERENTIAL FLUX VS. ENERGY. ROCKET A18.219-1

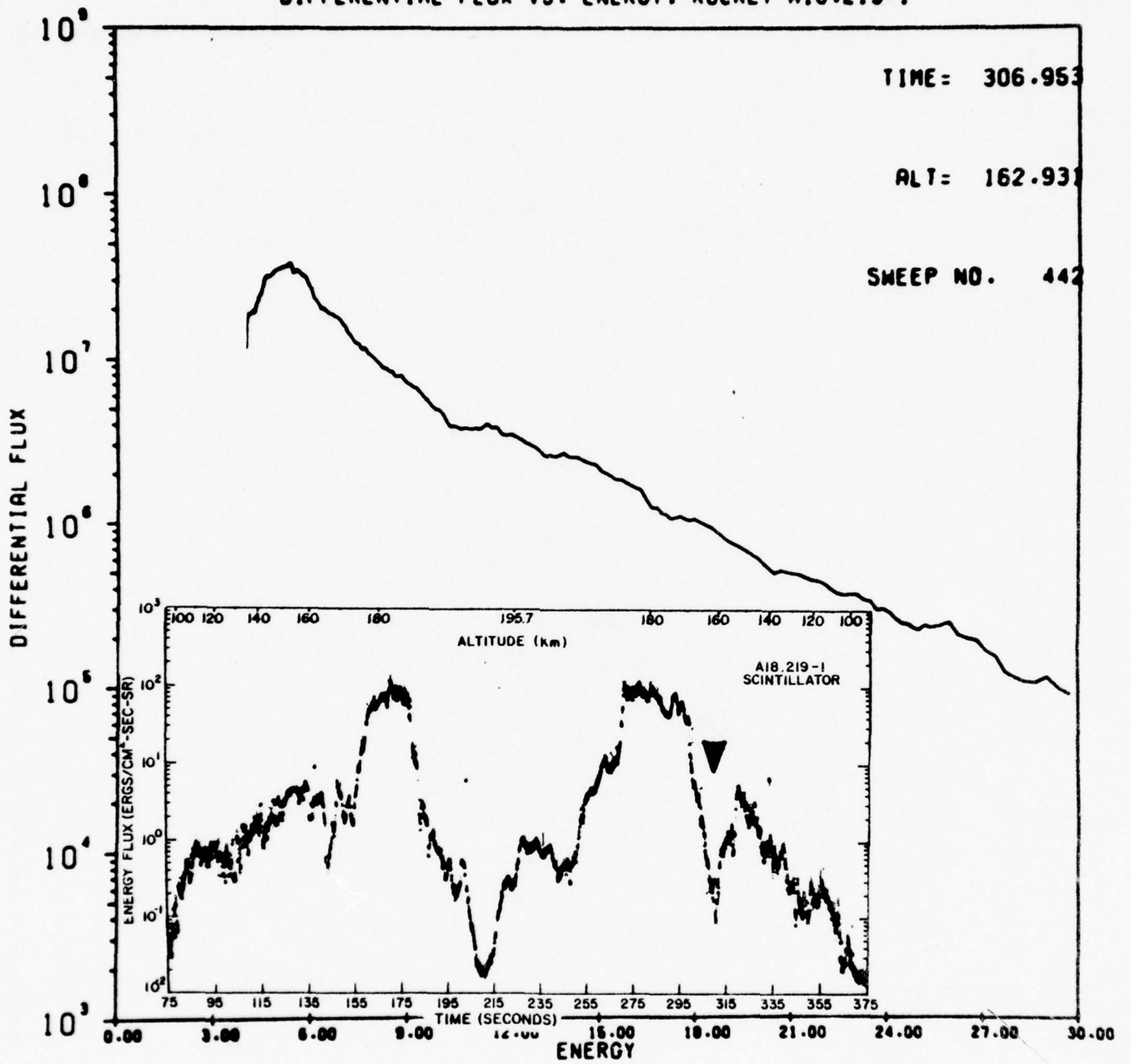


FIGURE 21

DIFFERENTIAL FLUX VS. ENERGY. ROCKET A18.219-1

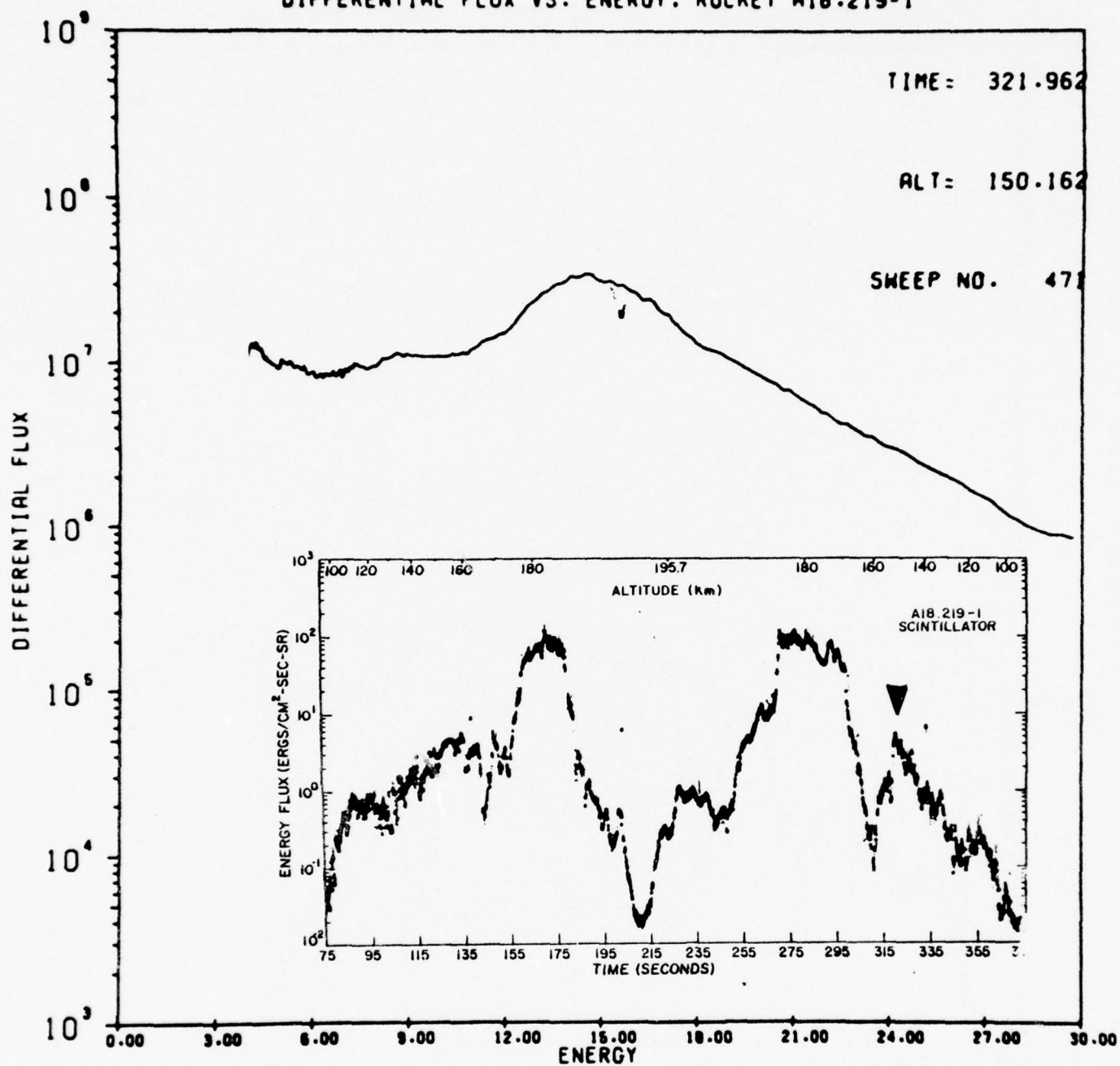


FIGURE 22

DIFFERENTIAL FLUX VS. ENERGY. ROCKET A18-219-1

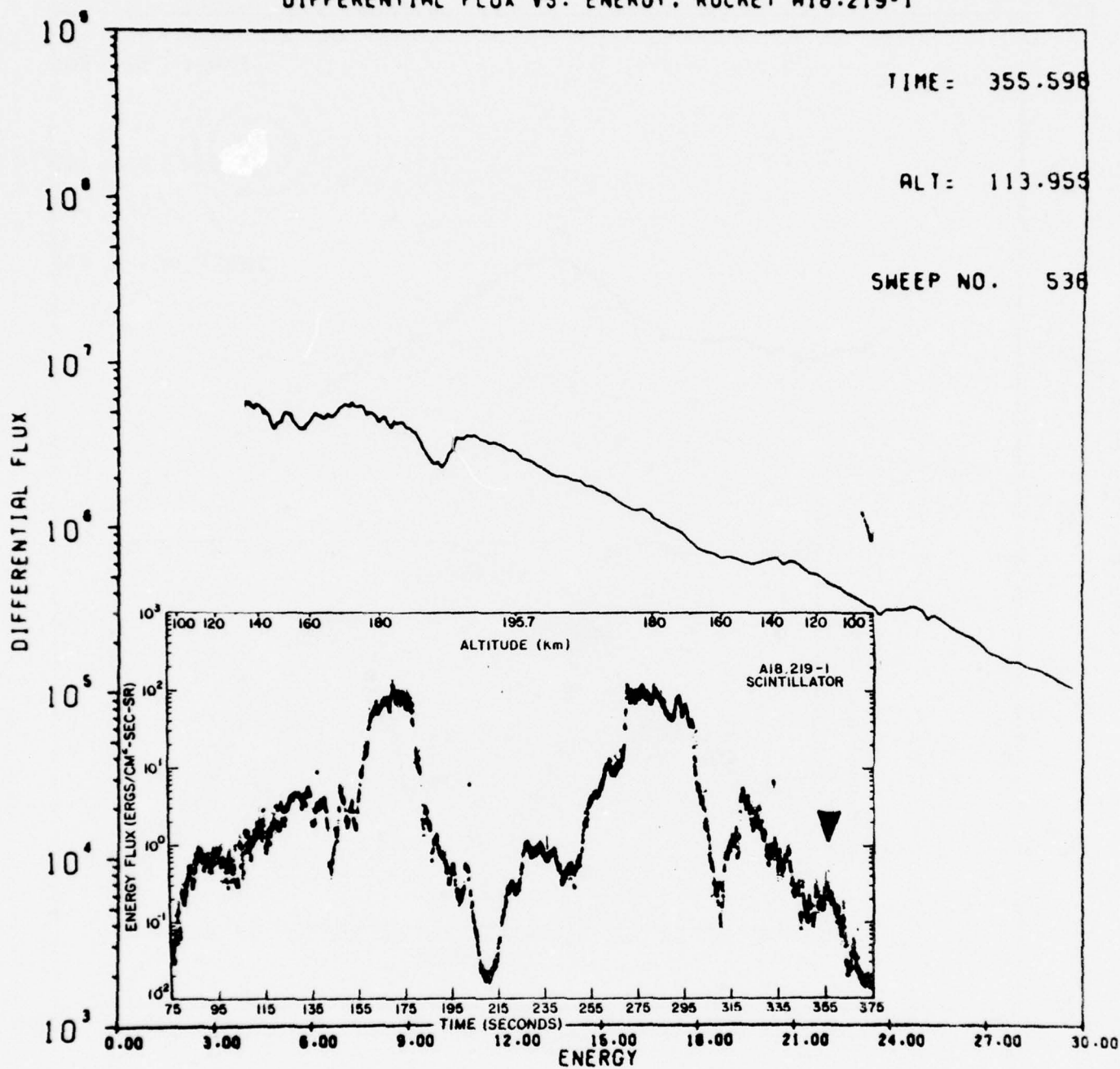


FIGURE 23

Appendix 2
Spectral Radiance Calculations at
4.3 μm , 9.6 μm , and 15 μm

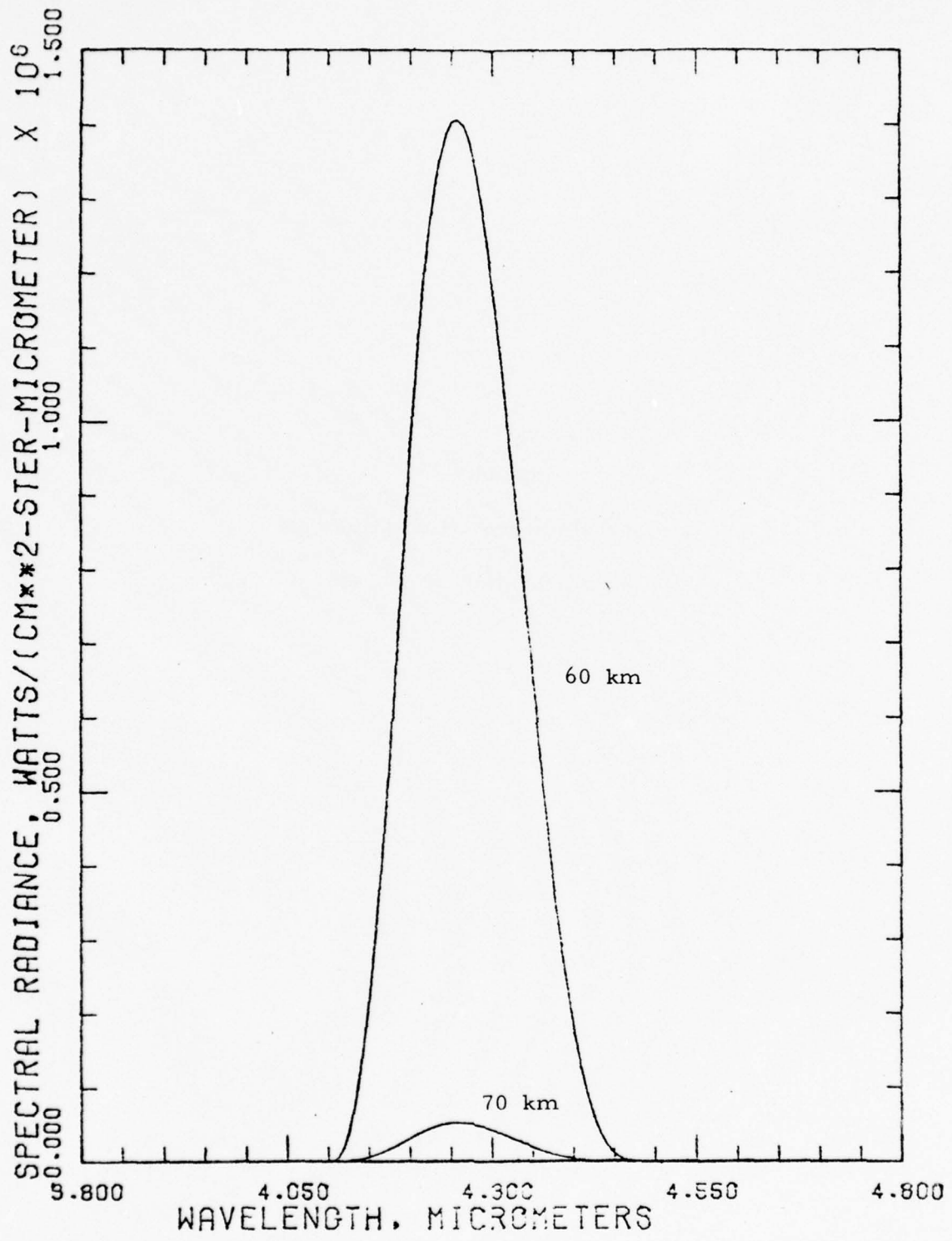


Figure A.2-1 Spectral Radiance in Upward Direction
 above indicated altitude, US Standard
 Atmosphere, 1962. CO₂ 4.3 μ m band.

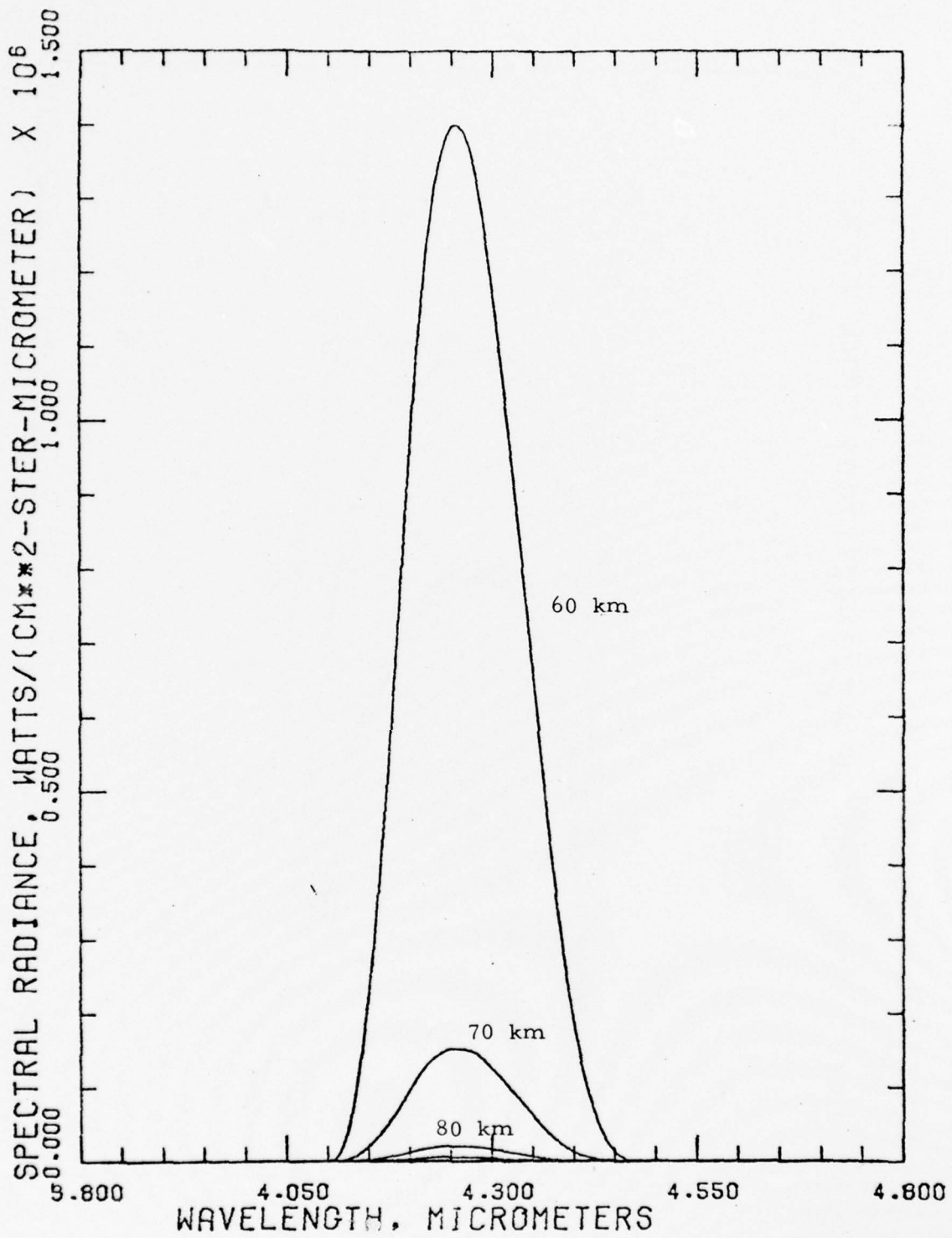


Figure A.2-2 Spectral Radiance in Upward Direction
 above indicated altitude. 230 K Mesopause,
 4.3 μ m CO₂ band.

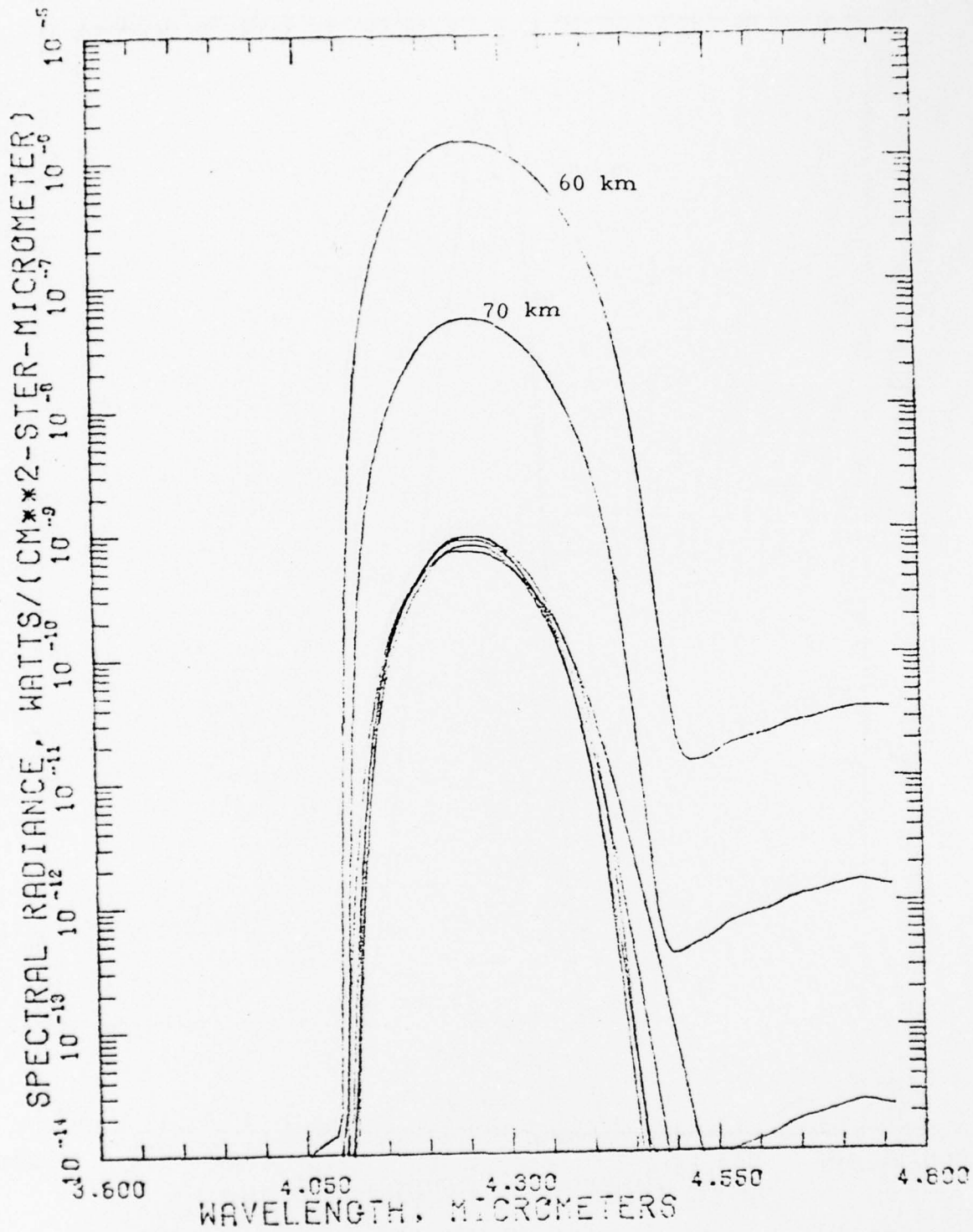


Figure A.2-3 Spectral Radiance in Upward Direction above indicated altitude, US Standard Atmosphere, 1962. CO_2 $4.3 \mu\text{m}$ band.

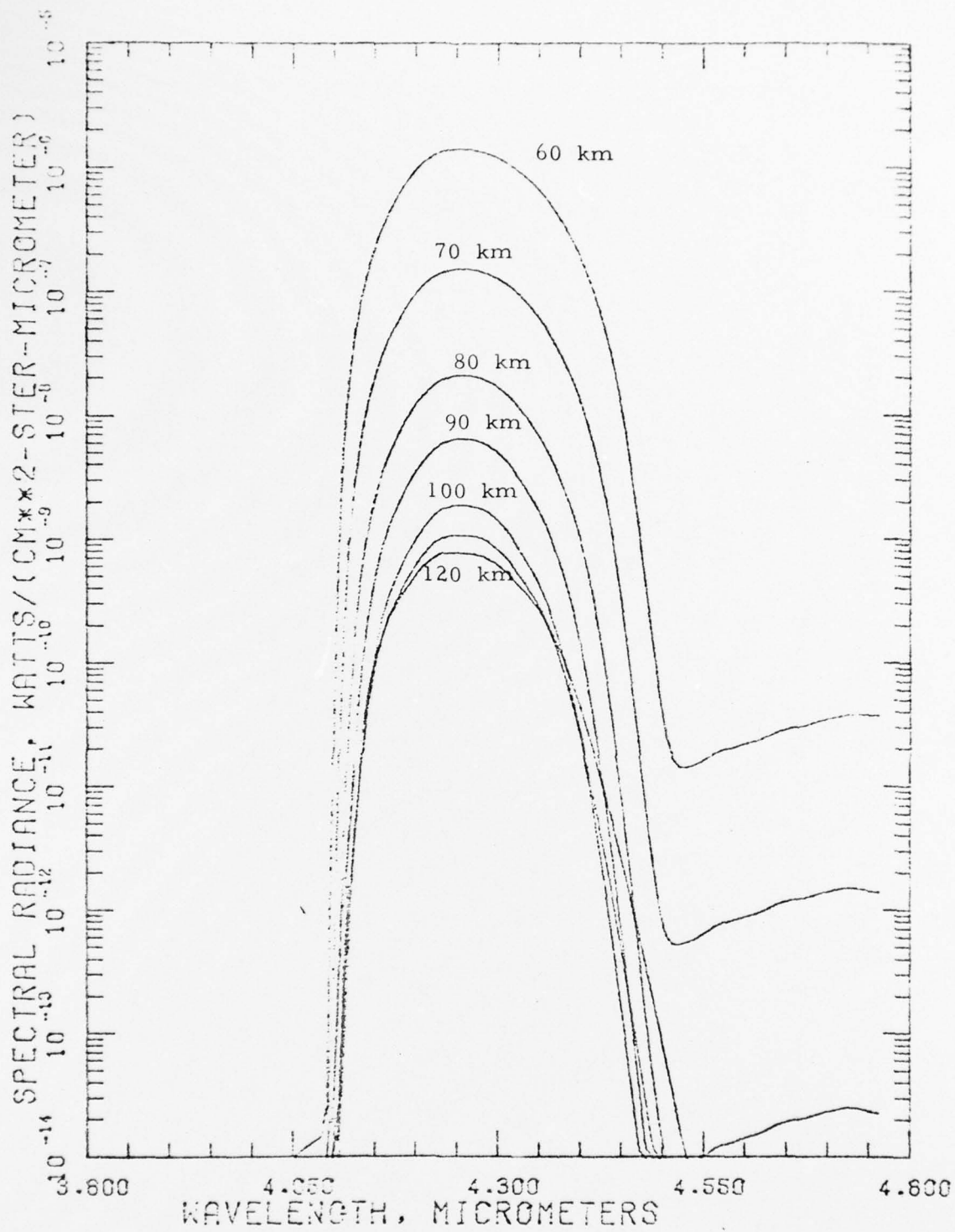


Figure A.2-4 Spectral Radiance in Upward Direction
 above indicated altitude, 230 K Mesopause,
 4.3 μ m CO₂ band.

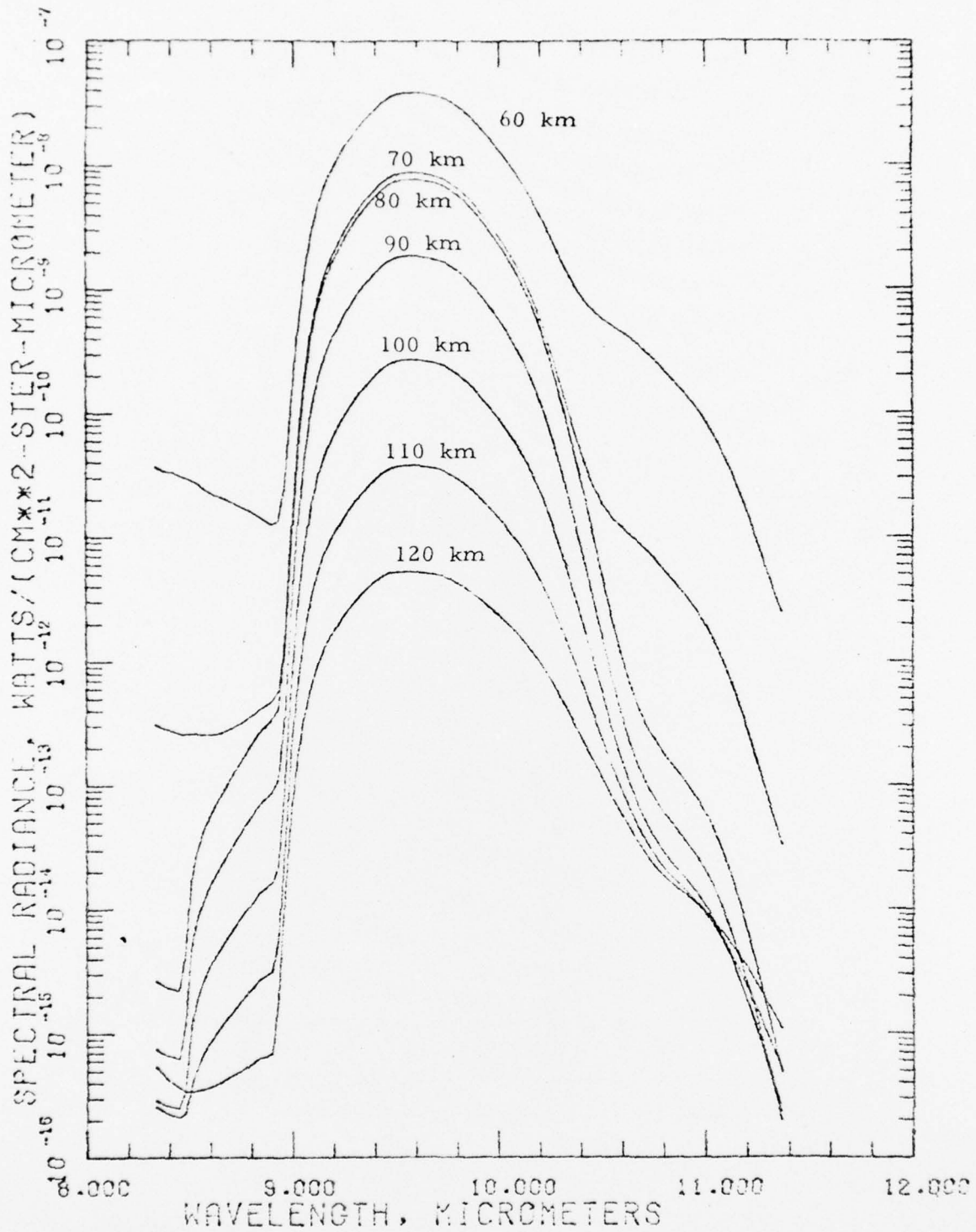


Figure A.2-5 Spectral Radiance in Upward Direction above indicated altitude, US Standard Atmosphere, 1962. Ozone 9.6 μ m band.

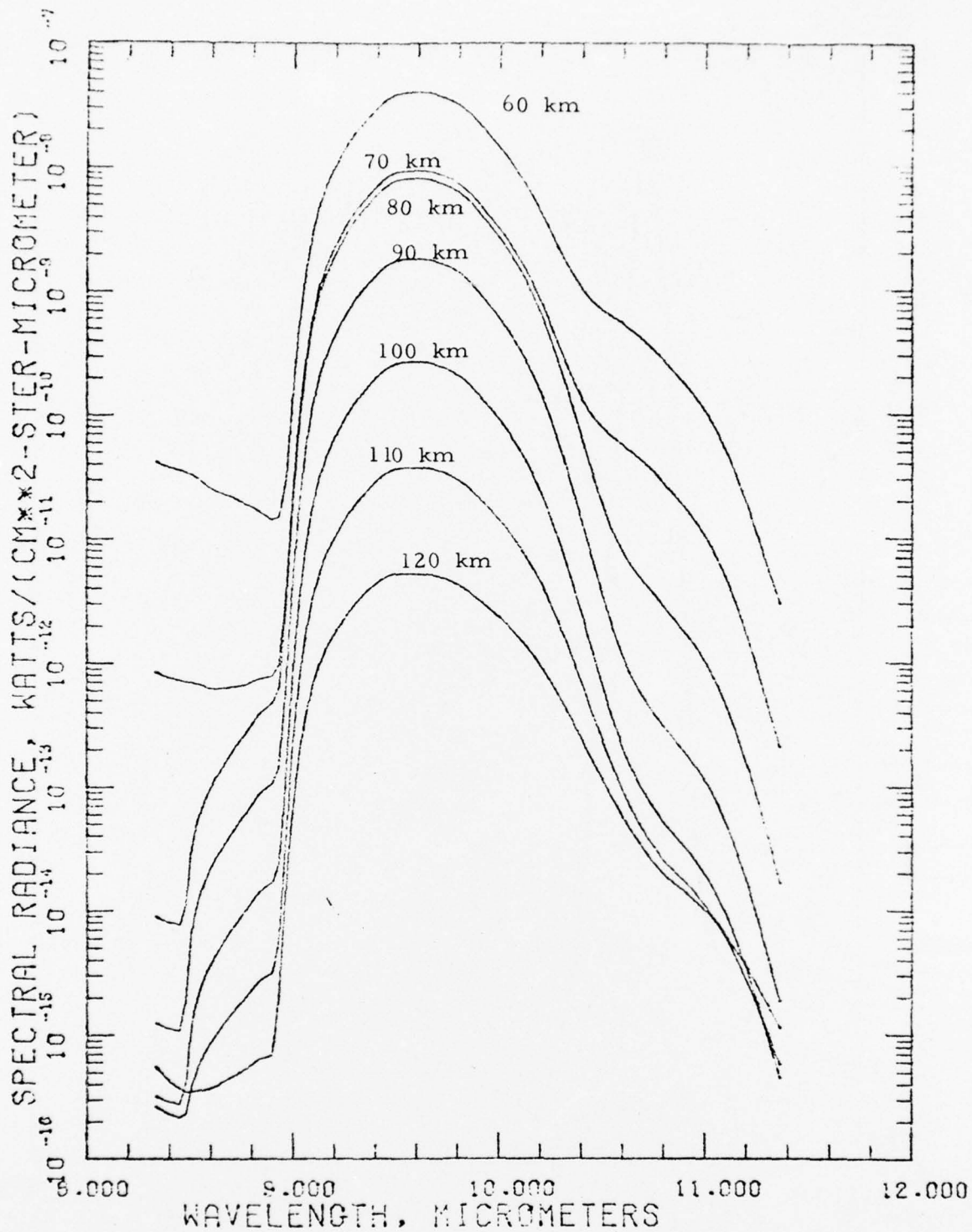


Figure A.2-6 Spectral Radiance in Upward Direction above indicated altitude. 230 K Mesopause, Ozone 9.6 μ m band.

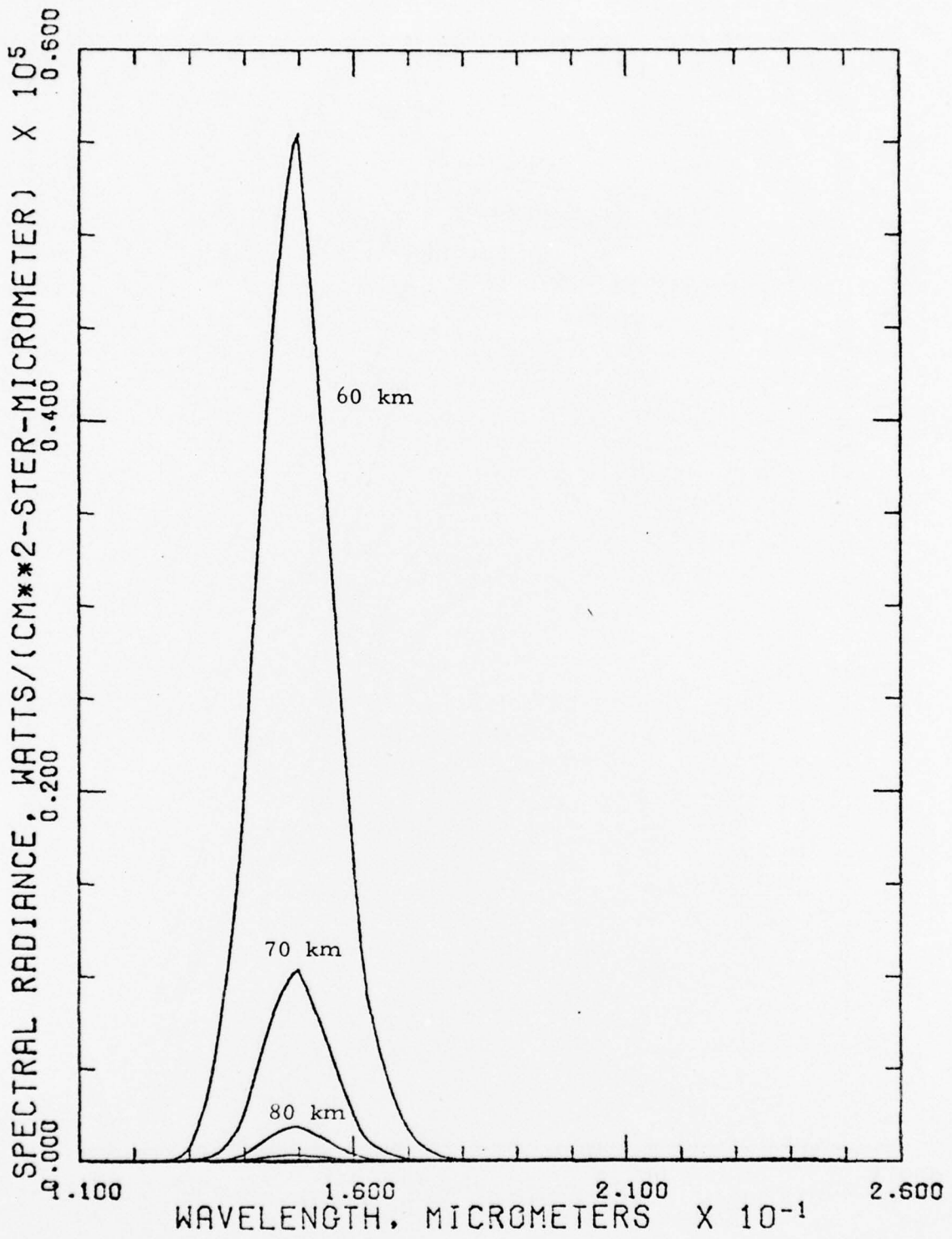


Figure A.2-7 Spectral Radiance in Upward Direction above indicated altitude, US Standard Atmosphere, 1962. CO₂ 15 μ m band.

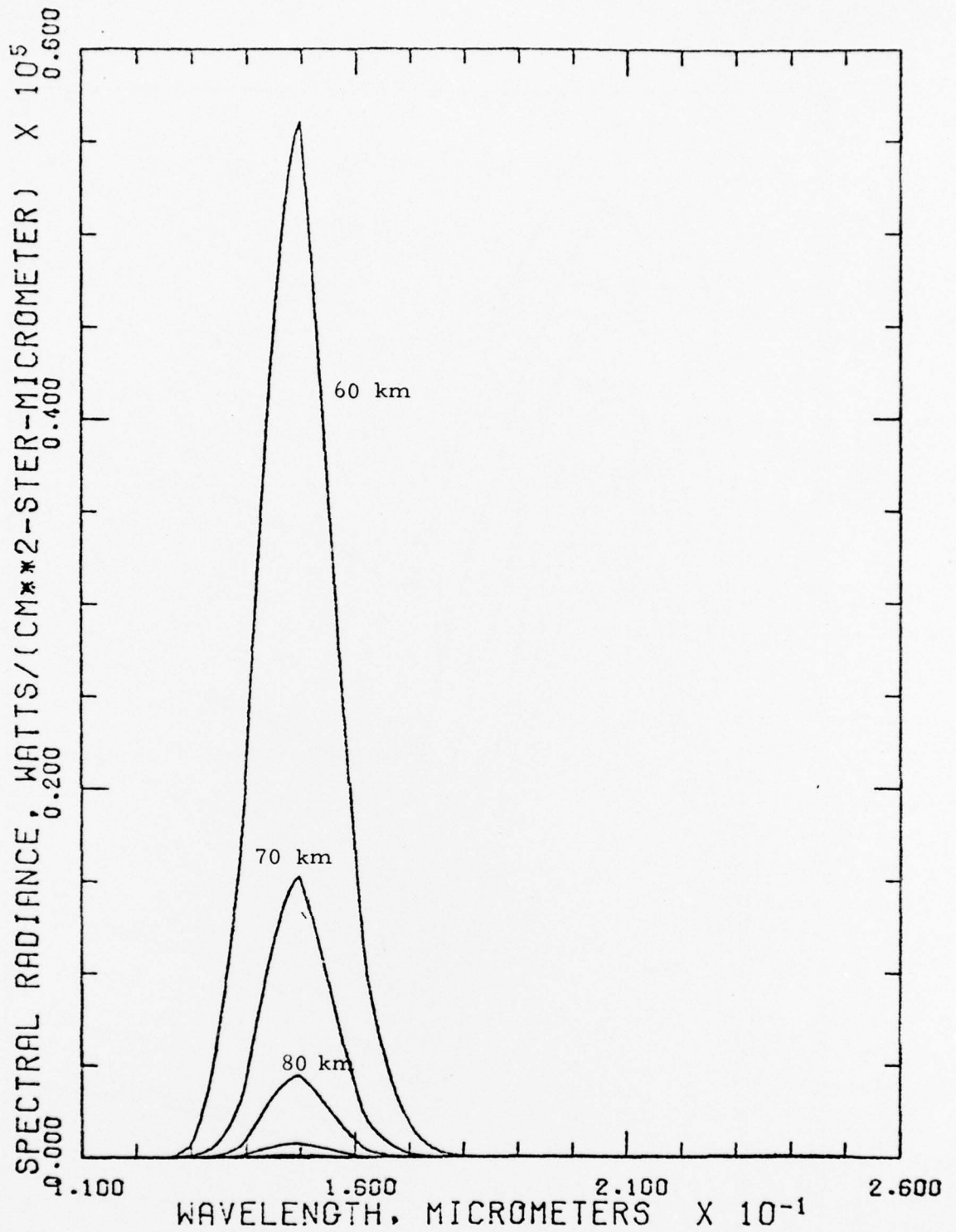


Figure A.2-8 Spectral Radiance in Upward Direction
 above indicated altitude. 230 K Mesopause,
 CO₂ 15 μ m band.

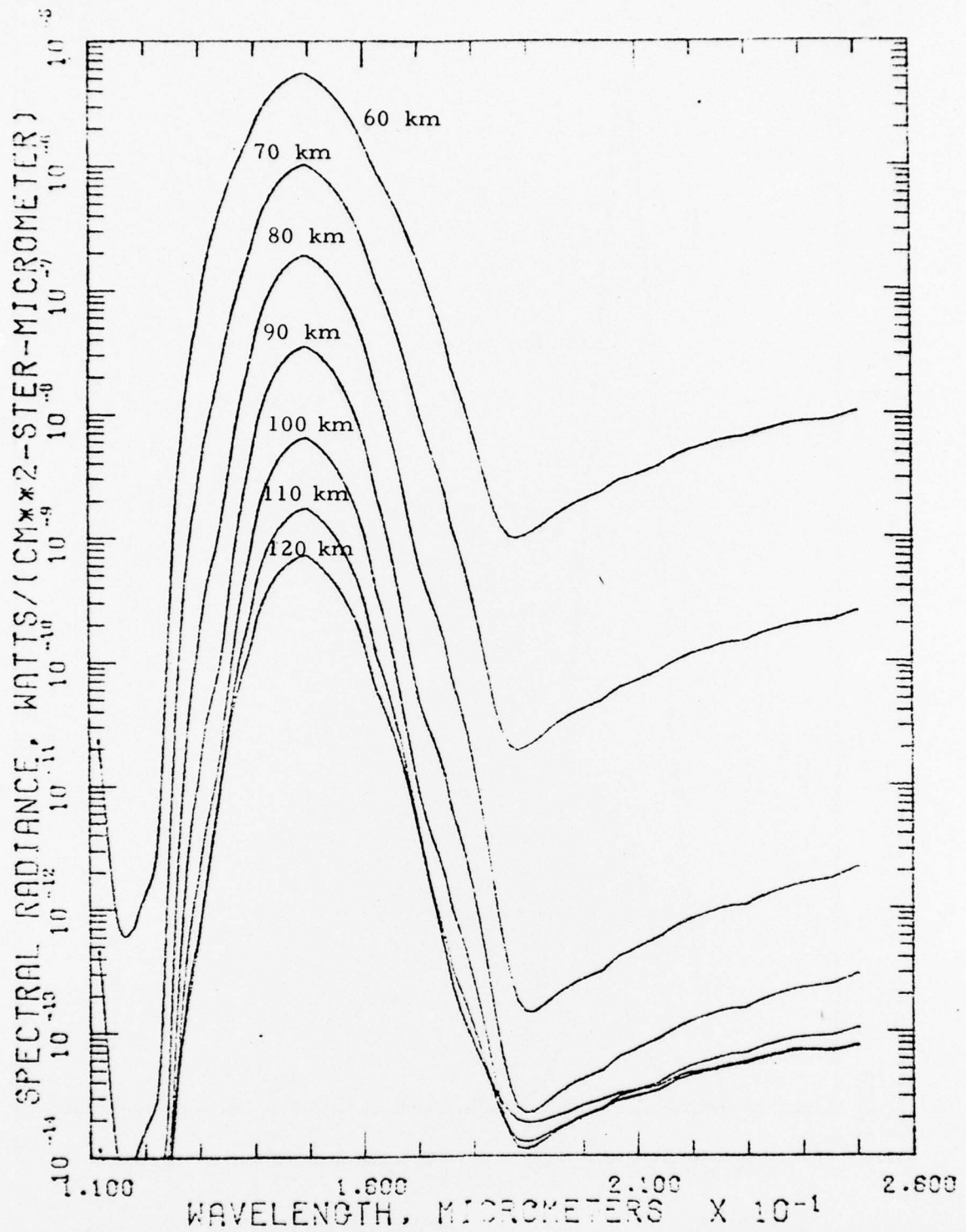


Figure A.2-9 Spectral Radiance in Upward Direction
 above indicated altitude, US Standard
 Atmosphere, 1962. CO₂ 15 μm band.

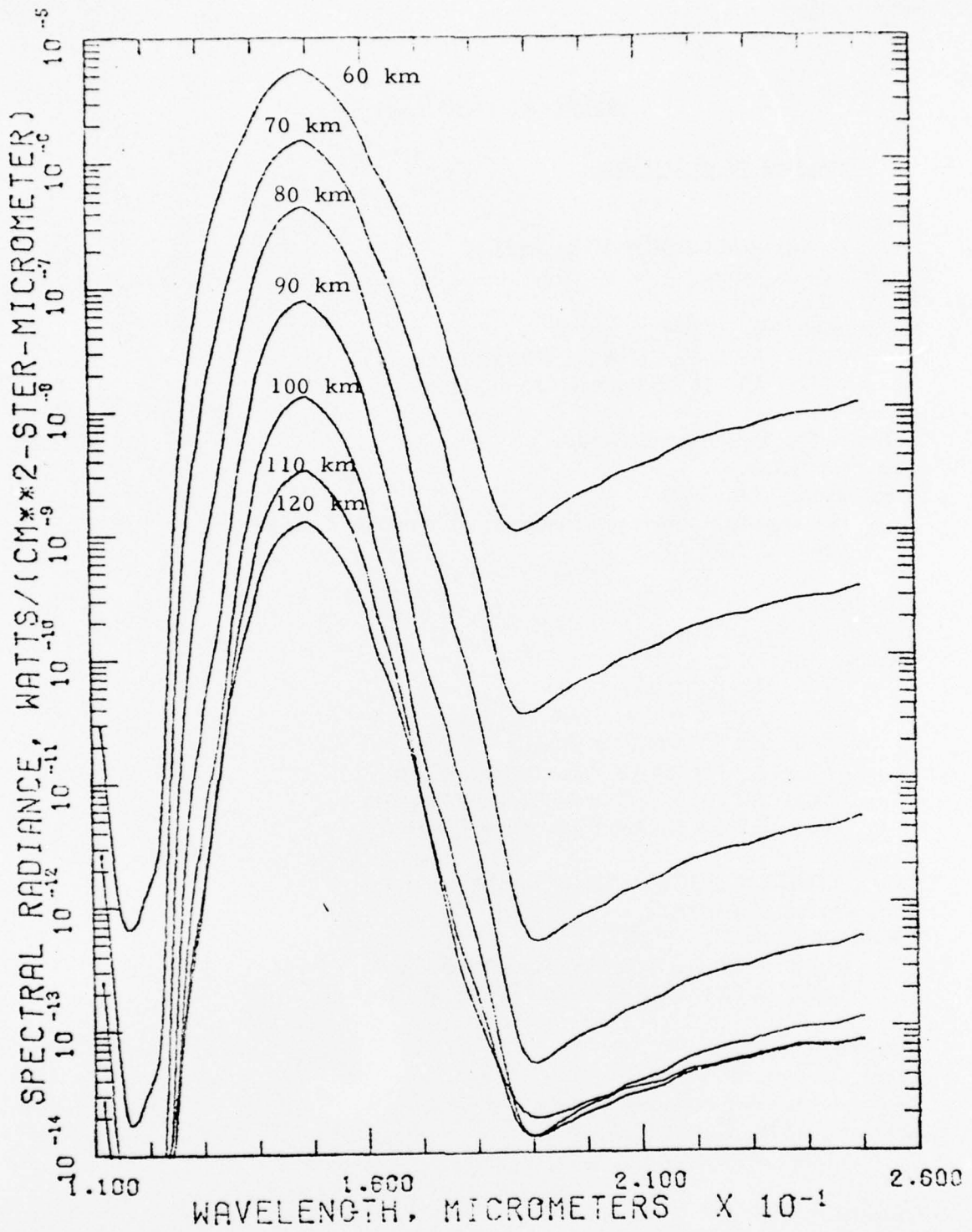


Figure A.2-10 Spectral Radiance in Upward Direction
 above indicated altitude. 230 K Mesopause,
 CO_2 15 μm band.

DISTRIBUTION LIST

Department of Defense

Director
Defense Advanced RSCH Proj Agency
Architect Building
1400 Wilson Blvd.
Arlington, VA 22209
01CY ATTN LTC W.A Whitaker
01CY ATTN STO Capt. J. Justice

Defense Documentation Center
Cameron Station
Alexandria, VA 22314
(12 copies if open publication, otherwise 2 copies)
12CY ATTN TC

Director
Defense Nuclear Agency
Washington, D. C. 20305
01CY ATTN DDST
02CY ATTN STTL Tech. Library
01CY ATTN STSI Archives
03CY ATTN RAAE Charles A. Blank
01CY ATTN RAAE Harold C. Fitz, Jr.
01CY ATTN RAAE Maj. John Clark

Dir. of Defense RSCH & Engineering
Department of Defense
Washington, D. C. 20301
01CY ATTN AD/S&AS Daniel Brockway
01CY ATTN DDS&SS Richard S. Ruffine

Commander
Field Command
Defense Nuclear Agency
Kirtland AFB, NM 87115
01CY ATTN FCPR

Chief
Livermore Division FLD Command DNA
Lawrence Livermore Laboratory
P.O. Box 808
Livermore, CA 94550
01CY ATTN FCPRL

Weapons Systems Evaluation Group
400 Army Navy Drive
Arlington, VA 22202
01CY ATTN Document Control

Department of Defense Contractors

Technology International Corporation
75 Wiggins Avenue
Bedford, MA 01730
01CY ATTN W.P. Boquist

Utah State University
Logan, UT 84321
01CY ATTN Doran Baker
01CY ATTN Kay Baker
01CY ATTN D. Burt
01CY ATTN C Wyatt

Visidyne, Inc.
19 Third Avenue
North West Industrial Park
Burlington, MA 01803
01CY
01CY ATTN J.W. Carpenter
01CY ATTN William Reidy
01CY ATTN T.C. Degges

R & D Associates
1815 N. FT. Myer Drive
11th Floor
Arlington, VA 22209
01CY ATTN Herbert J. Mitchell

Rand Corporation, The
1700 Main Street
Santa Monica, CA 90406
01CY ATTN James Oakley

Science Applications, Inc.
P.O. Box 2351
La Jolla, CA 92038
01CY ATTN Daniel A. Hamlin

Space Data Corporation
1331 South 26th Street
Phoenix, AZ 85034
01CY ATTN Edward F. Allen

Stanford Research Institute
333 Ravenswood Avenue
Menlo Park, CA 94025
01CY ATTN Walter G. Chestnut
01CY ATTN M. Baron
01CY ATTN Ray L. Leadabrand

Mission Research Corporation
735 State Street
Santa Barbara, CA 93101
01CY ATTN P. Fischer
01CY ATTN D. Archer

Photometrics, Inc.
442 Marrett Road
Lexington, MA 02173
01CY ATTN Irving L. Kofsky

Physical Dynamics Inc.
P.O. Box 1069
Berkeley, CA 94701
01CY ATTN Joseph B. Workman

Physical Sciences, Inc.
607 North Avenue, Door 18
Wakefield, MA 01880
01CY ATTN Kurt Wray

R & D Associates
P.O. Box 9695
Marina Del Rey, CA 90291
01CY ATTN Robert E. Lelevier
01CY ATTN Forest Gilmore

Geophysical Institute
University of Alaska
Fairbanks, AK 99701
(All Class ATTN: Security Officer)
03CY ATTN Neil Brown (UNCL Only)
01CY ATTN T. N. Davis (UNCL Only)

Honeywell Incorporated
Radiation Center
2 Forbes Road
Lexington, MA 02173
01CY ATTN W. Williamson

Institute for Defense Analyses
400 Army Navy Drive
Arlington, VA 22202

01CY ATTN Ernest Bauer
01CY ATTN Hans Wolfhard

Lockheed Missles and Space Company
3251 Hanover Street
Palo Alto, CA 94303

01CY ATTN John Kumer
01CY ATTN J. B. Reagan D/52-12
01CY ATTN Billy M. McCormac Dept. 52-12
01CY ATTN Martin Walt Dept. 52-10
01CY ATTN Richard G. Johnson Dept. 52-12
01CY ATTN Robert D. Sears Dept. 52-14

Aerodyne Research, Inc.
Tech/Ops Building
20 South Avenue
Burlington, MA 01803

01CY ATTN F. Bien
01CY ATTN M. Camac

Aerospace Corporation
P. O. Box 92957
Los Angeles, CA 90009

01CY ATTN R. D. Rawcliffe
01CY ATTN Harris Mayer
01CY ATTN T. Taylor
01CY ATTN R. Grove

General Electric Company
Tempo-Center for Advanced Studies
816 State Street (P. O. Drawer QQ)
Santa Barbara, CA 93102

01CY ATTN Warren S. Knapp
05CY ATTN Dasiac Art Feryok

General Research Corporation
P. O. Box 3587
Santa Barbara, CA 93105

01CY ATTN John Ise, Jr.

Other Government

Department of Commerce
Office of Telecommunications
Institute for Telecom Science
Boulder, CO 80302
01CY ATTN Glenn Falcon
01CY ATTN William F. Utlaut

NASA
600 Independence Avenue S W
Washington, D. C. 20546
01CY ATTN M. Dubin
01CY ATTN J. Holz

U.S. Energy Rsch. and Dev. Admin.

Los Alamos Scientific Laboratory
P.O. Box 1663
Los Alamos, NM 87545
01CY ATTN Doc. Con. for Milton Peek

Department of the Air Force

Commander
Aeronautical Systems Division, AFSC
Wright-Patterson AFB, OH 45433
01CY ATTN ASD-YH-EX Ltc. Robert Leverette

AF Cambridge Rsch. Labs, AFSC
L. G. Hanscom Field
Bedford, MA 01730
05CY ATTN OPR James C. Ulwick
01CY ATTN LKB Kenneth S. W. Champion
01CY ATTN OP John S. Garing
01CY ATTN OPR Alva T. Stair

AF Weapons Laboratory, AFSC
Kirkland AFB, NM 87117
01CY ATTN DYT
01CY ATTN SUL
01CY ATTN DYT Maj. Don Mitchell

Department of the Navy

Chief of Naval Research
Navy Department
Arlington, VA 22217
01CY ATTN Code 427 CDR Ronald J. Oberle

Commander
Naval Electronics Laboratory Center
San Diego, CA 92152
01CY ATTN Code 2200 1 Verne E. Hildebrand
01CY ATTN Code 2200 TLAN Rothmuller

Director
Naval Research Laboratory
Washington, D. C. 20375
01CY ATTN Code 7750 Paul Juluene
01CY ATTN Code 7750 Darrell F. Strobel
01CY ATTN Code 2027 Tech. Lib.
01CY ATTN Code 7127 Charles. Y. Johnson
01CY ATTN Code 7701 Jack D. Brown
01CY ATTN Code Douglas Strickland
01CY ATTN Code 7750 Timothy P. Coffey
01CY ATTN Code 7750 Ellis Hyman

Commander
Naval Surface Weapons Center
White Oak, Silver Spring, MD 20910
01CY ATTN Code 213 William L. Derksen
01CY ATTN Code 1224 Navy Nuc. Prgms. Off.

Department of the Army

Commander
Harry Diamond Laboratories
2800 Powder Mill Road
Adelphi, MD 20783
(CNWDI-Inner Envelope: ATTN: AMXDO-RBH)
02CY ATTN AMXDO-NP.

Director
U. S. Army Ballistic Research Labs
Aberdeen Proving Ground, MD 21005
01CY ATTN AMXBR-CA Franklin E. Niles

Headquarters
U. S. Army Elct. Warfare Lab. (ECOM)
Missile Electronic Warfare Tech. Area
White Sands Missile Range, NM 88002
01CY ATTN E. Butterfield